

Study of Microstructural and Magnetic Properties of Melt Textured NdBCO Superconductor

A Thesis submitted
for the award of the Degree of
Doctor of Philosophy

By

N. Hari Babu



**School of Physics
University of Hyderabad
Hyderabad 500 046, India**

November 1997

**DEDICATED
TO MY
PARENTS**

DECLARATION

I hereby declare that the work reported in this thesis has been carried out by me under the supervision of Dr. T. Rajasekharan at Defence Metallurgical Research Laboratory (DMRL), Hyderabad. I also declare that this has not been submitted to any University or Institute for the award of any degree/diploma.

Date: 27-11-97

Place : Hyderabad

N. Hari Babu
N. HARI BABU

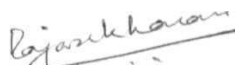
(CANDIDATE)

CERTIFICATE

This is to certify that the research work compiled in this thesis entitled "**STUDY OF MICROSTRUCTURAL AND MAGNETIC PROPERTIES OF MELT TEXTURED NdBCO SUPERCONDUCTOR**" has been carried out by Mr. **N. Hari Babu** under my supervision and the same has not been submitted for the award of any degree of any University.

Date : 27-11-97

Place : Hyderabad



Dr. T. RAJASEKHARAN
(SUPERVISOR)



DEAN
DEAN,
SCHOOL OF PHYSICS
UNIVERSITY OF HYDERABAD

ACKNOWLEDGEMENT

I express my deep sense of gratitude to my research supervisor Dr. T. Rajasekharan for his guidance, critical and useful discussions throughout my Ph.D work.

I thank the Director, Defence Metallurgical Research Laboratory, who allowed me to use the DRDO facilities for carrying the present research work.

I thank Prof. K. N. Srivastava, Dean, and former Deans of the School of Physics, University of Hyderabad for their kind cooperation. I also express my sincere thanks to all teachers, who taught in my post graduation.

I am extremely thankful to Dr. V. Seshu **Bai**, School of Physics, University of Hyderabad, for readily allowing me to use the research facilities in the lab, useful discussions and constant encouragement throughout my Ph. D work.

I thank Prof. S. K. Malik, TIFR, for allowing the use of SQUID magnetometer.

I am thankful to A. Manik Rao, S. Suri, A. **Kamalakar** Rao Technicians and T. Rajender Singh, Technical officer for their cooperation and help.

I thank my colleagues Sudhakar Reddy and Viswanath for their encouragement, helpful discussions, cooperation and company at DMRL. I also thank my colleagues Ravi, Harish, Patanjali, Isaac and Radhika for their helpful discussions and cooperation at UH.

I thank Veera Mohan, P.D. Babu, M. B. Srinivas, **Sambasiva** Rao, Subbu, Ravi Kanth, Satheesh, Lok, Srinath, Anita, Rama Sita and Senthil for their help and moral support.

I am grateful to my friends *viz* Raghava Prasad, Raja Sekhar, Venkat (ACS), Murthy, Sambasiva Rao, Saradhi, Arun, Bharadwaz, Kranthi, Murali, Mahadev and many other friends from departments of Life Sciences and Chemistry, for their constant company, humour and moral support which made my stay on the campus, a memorable one.

I acknowledge financial assistance in the form of NSF (DST), and SRF (**CSIR**).

I wish to acknowledge deepest sense of gratitude to my parents and other family members for their constant encouragement and moral support, which has made this endeavour possible.

Hari Babu

Table of Contents

1	Introduction	1
1.1	Brief historical development in superconductivity.	1
1.2	Discovery of high T_c superconductors.	4
1.3	YBa ₂ Cu ₃ O _y structure.	5
1.4	Preparation of bulk superconductors.	7
1.4.1	Sintering	7
1.4.2	Various melt growth processes.	8
1.5	Magnetic response of HTSC.	12
1.5.1	Critical state models.	12
1.5.2	Flux pinning	14
1.5.3	ac susceptibility.	16
1.5.4	Magnetic flux penetration	17
1.6	Motivation and aim of the work	17
2	Experimental Techniques	24
2.1	Optical microscope.	24
2.2	Scanning Electron Microscope.	25
2.3	Quantitative analysis of microstructures.	26
2.4	X-ray diffractometer.	27
2.5	dc electrical resistivity.	29
2.6	ac susceptibility.	30

2.7	Magnetic flux profile measurements.	32
2.8	SQUID magnetometer.	34
3	Melt processing and microstructure of NdBCO superconductor	36
3.1	Introduction.	36
3.2	Synthesis of Nd-123 and Nd-422 powder in large scale.	38
3.2.1	NdBa ₂ Cu ₃ O ₇ phase.	38
3.2.2	Nd ₄ Ba ₂ Cu ₂ O ₁₀ phase.	39
3.3	Sintered NdBCO.	40
3.4	Melt Processing.	41
3.4.1	Furnace configuration.	41
3.4.2	The melt processing experiments.	42
3.5	Microstructural investigations.	44
3.6	Effect of cooling rate on microstructural features.	49
3.7	Infiltration and Growth process.	52
3.8	Effect of rates of cooling on IG processed samples.	59
4	ac susceptibility measurements	62
4.1	Introduction.	62
4.2	Temperature variation of ac susceptibility.	64
4.2.1	Polycrystalline NdBCO sample.	64
4.2.2	Melt textured NdBCO samples.	66
4.3	Reversible fluxoid motion.	71
4.4	Bulk-pinning hysteresis loss.	73
4.5	Universal behavior of ac susceptibility.	74
4.5.1	Field dependence of ac susceptibility in BSCCO superconductor.	77

4.5.2	Temperature dependence of ac susceptibility in BSCCO superconductor.78
4.5.3	Field variation of ac susceptibility in melt textured Nd-BCO superconductor.	80
4.5.4	Temperature variation of ac susceptibility in melt textured NdBCO superconductor.	80
5	Magnetic flux profiles	84
5.1	Introduction.	84
5.2	Experimental.	86
5.3	Magnetic flux profiles in polycrystalline superconductors : BSCCO and NdBCO.	88
5.3.1	Profiles with $H_{dc} = 0$	88
5.3.2	Profiles with $(H_{dc} \neq 0)$	90
5.4	Magnetic flux profiles in melt textured NdBCO samples.	91
5.4.1	Slow cooled samples.	91
5.4.2	Fast cooled textured samples.	96
5.5	Information on domain coupling strength from flux profiles	98
5.6	Theoretical model calculations.	100
6	dc magnetization measurements	105
6.1	Introduction.	105
6.2	Experimental.	106
6.3	Results on melt processed NdBCO samples.	106
6.4	Results on IG processed NdBCO sample.	114
7	Conclusions	117

Chapter 1

Introduction

1.1 Brief historical development in superconductivity

Kamerlingh Onnes [1], discovered that the dc resistivity of mercury suddenly drops to zero whenever the sample is cooled below 4.2 K, the boiling point of liquid helium. He named the new phenomenon - superconductivity. He has also discovered that a sufficiently strong magnetic field restores the resistivity in the sample. Later on it was discovered that many other metallic elements exhibit superconductivity at very low temperatures. The highest critical temperature (T_c) of all pure metals was discovered in Nb, $T_c = 9.2$ K.

Meissner and Ochsenfeld [2] discovered another distinct property of the superconducting state : **perfect diamagnetism**. They noticed that the magnetic flux is expelled from the interior of the sample that is cooled below the critical temperature in weak external magnetic fields.

John Bardeen, Leon Cooper and Robert Schrieffer [3] proposed a complete microscopic theory of superconductivity that is usually referred to as the BCS theory. The basis of the theory is the interaction of a gas of conduction electrons with elastic waves of the crystal lattice. Ordinarily the electrons repel each other by Coulomb force, but in the special case of a superconductor at sufficiently low temperatures there is a net attraction

between two electrons that form the so-called Cooper pairs. Naively one can think of an electron that polarizes its environment, i.e, attracts positively charged ionic background of the lattice, which in turn attracts another electron of the opposite momentum. Below the critical temperature the attraction permits the formation of Cooper pair that are pairs of electrons of opposite momenta and spins.

As a result of such attractive interaction, the condensed state of highly correlated pairs of conduction electrons is formed below T_c . All Cooper pairs move in a single coherent motion, so a local perturbation, like an impurity, cannot scatter an individual pair. Once this collective, highly coordinated state of coherent super-electrons is set in motion, its flow is without any dissipation.

London theory

Following the discovery of the Meissner effect, F. and H. London [4] explained the Meissner effect by modifying the Maxwell's electrodynamic equations. London derived a phenomenological equation

$$\mathbf{V} \times \mathbf{J} + (\mu_o n_s e^2 / m) \mathbf{r} = \mathbf{0}. \quad (1.1.1)$$

An expression of the London's equation in one dimensional form is $d^2 H / dx^2 = H / \lambda_L^2$, where λ_L is equal to $\sqrt{m / \mu_o n_s e^2}$.

For a uniform, infinite superconductor in the region $x > 0$, and with the magnetic field H_o applied parallel to the surface, the field inside the superconductor is given by the following solution of the above equation

$$H = H_o \exp(-x / \lambda_L) \quad (1.1.2)$$

The field decreases exponentially and vanishes in the interior of the superconductor. λ_L is the London penetration depth that measures the extension of the penetration of the

magnetic field inside the superconductor. It shows that, in order to have zero field within the bulk of the material, one must have a sheet of superconducting current which flows within λ_L from the surface and which creates an opposite field inside the superconductor that cancels the externally applied magnetic field.

Type-I and Type-II superconductors

Superconducting materials that completely expel magnetic flux until they become completely normal are called **type-I** superconductors. The strength of the applied magnetic field required to completely destroy the state of perfect diamagnetism in the interior of the superconducting specimen is called the **thermodynamic** critical field H_c . The variation of the critical field H_c with temperature for type-I superconductor is approximately parabolic:

$$H_c = H_0(1 - (T/T_c)^2), \quad (1.1.3)$$

where H_0 is the extrapolated value of H_c at $T = 0$. The magnetization curve of a type-I superconductor is given in Fig. 1.1 (a). The Meissner effect, $B = 0$, corresponds to $\mathbf{M} = -H$. Above the critical field H_c , the material becomes normal, so $\mathbf{M} = 0$. The negative sign shows that the sample becomes a perfect diamagnet that excludes the flux completely from its interior by means of surface currents. For type-II superconductors there are two critical fields : the lower H_{c1} and the upper H_{c2} . The flux is completely expelled only up to the field H_{c1} . In applied fields smaller than H_{c1} , a type-II superconductor behaves just like a type-I superconductor below H_c . Above H_{c1} the flux partially penetrates into the material until the upper critical field, H_{c2} , is reached. Above H_{c2} , the material returns to the normal state. The typical magnetization curve for type-II superconductor is shown in Fig. 1.1(b). Between H_{c1} and H_{c2} the superconductor is said to be in the mixed state. The Meissner effect is only partial. For all partial fields $H_{c1} < H < H_{c2}$, the magnetic flux partially penetrates the superconducting specimen in the form of tiny microscopic filaments called vortices. It consists of a normal core, in which the magnetic field is large,

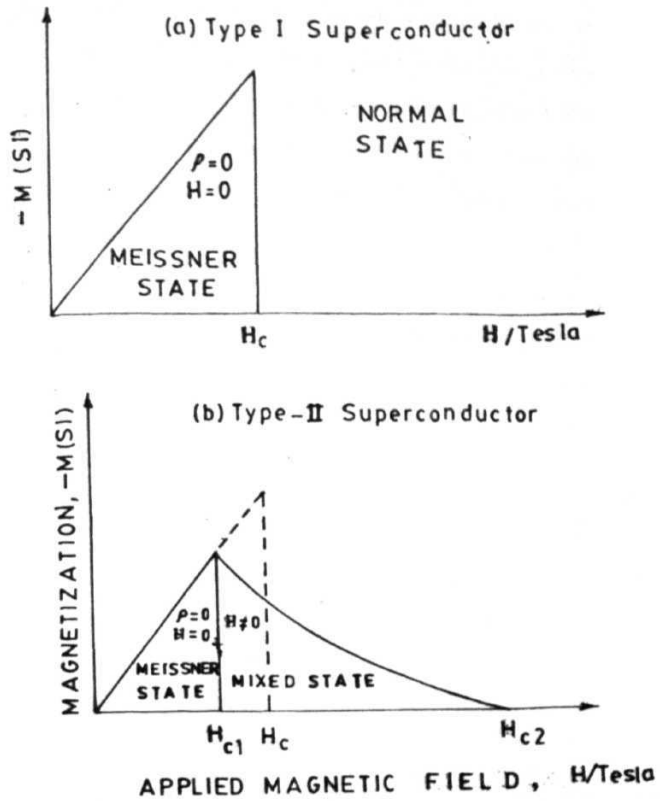


Fig. 1.] Variation of magnetization as a function of the magnetic field for (a) type-I superconductor and (b) type-II superconductor.

surrounded by a superconducting region in which flows a persistent supercurrent which maintains the field within the core. Each vortex carries a magnetic flux $\phi_0 = h/2e = 2.067 \times 10^{-15}$ Weber, where h is the Planck constant and e is the charge of the electron. Penetration of flux in type-II superconductors through a lattice of flux lines had been predicted by Abrikosov [5]. The vortex tubes repel each other, and the most stable one is a triangular lattice. In that case, the distance between two vortices is given by

$$a = 1.072 \sqrt{\phi_0 / B} \quad (1.1.4)$$

The triangular flux line lattice is directly visualized by magnetic decoration techniques [6].

The coherence length

The coherence length ξ is the distance between two electrons of the Cooper pair within the highly correlated coherent superconducting state. Another definition of the coherence length is that it is a measure of the distance over which the gap parameter can vary, for instance, near a superconductor-normal metal boundary [7].

1.2 Discovery of high T_c superconductors

Many technologically important metallic superconductors of relatively low T_c were discovered till 1986 and they could be used only at liquid helium temperatures. Bednorz and Müller [8] discovered superconductivity in La-Ba-Cu-O ceramics at 30 K. This triggered a wide spread search among oxide compounds.

In 1987, research groups coordinated by Wu and Chu [9] discovered that the ceramic $\text{YBa}_2\text{Cu}_3\text{O}_7$ (YBCO) is superconducting with $T_c = 92$ K. This was an important discovery, because its T_c is above the boiling point of liquid nitrogen which is a much cheaper

coolant than liquid helium. This discovery simulated new research programs looking for technological applications.

Maeda *et al.* [10] discovered new ceramic superconducting phases in the Bi-Sr-Ca-Cu-O system. The highest T_c in that system is 110 K. Sheng and Hermann [11] discovered the Tl-Ba-Ca-Cu-O system, with a maximum T_c of 120 K. The problem with this system is the toxicity of thallium which necessitates careful handling and processing.

Putlin *et al.* [12] discovered a new layered superconductor, $\text{HgBa}_2\text{CuO}_{4+\delta}$ with T_c of 94 K. This temperature is not a new record, but it raised new hopes because it was quite a high value for a compound with a single CuO layer per elementary cell. Following this trend, Schilling *et al.* [13] published their finding of a critical temperature of 133.5 K in the three CuO layer structure of the $\text{HgBa}_2\text{Ca}_2\text{Cu}_3\text{O}_{1+x}$. The search for better high T_c materials continues today with more expectations. Improving the T_c is not the only important matter. For most applications, large critical current densities (J_c) of the order of 10^4 to 10^6 A/cm² are required, in the presence of large magnetic fields. J_c is not an intrinsic property of a superconductor, it is strongly dependent on its microstructure. Hence microstructural control is very important for practical applications. For realization of practical applications, it is also necessary that the processing routes that yield a high J_c through microstructural control should also enable the shaping of the material into the necessary geometries.

1.3 $\text{YBa}_2\text{Cu}_3\text{O}_y$ structure [14,15]

Except for some materials (like $\text{Ba}_{1-x}\text{K}_x\text{BiO}_3$ and YNiBC), most high- T_c superconductors are cuprate compounds. One of their characteristics is the presence of CuO_2 layers which dominate most properties. The schematic structure of $\text{YBa}_2\text{Cu}_3\text{O}_6$ is presented in

Fig. 1.2. The unit cell is developed from that of a tetragonal perovskite tripled along the c-axis and it consists of a sequence of copper-oxygen layers. It is an insulator [15]. It has to be doped to gradually become a metallic conductor and a superconductor below some critical temperature. The doping is achieved by adding additional oxygen which forms CuO 'chains'. These oxygen ions attract electrons from the CuO_2 planes which therefore become metallic. Therefore $\text{YBa}_2\text{Cu}_3\text{O}_{6+x}$, where x corresponds to partial oxygen content, for $0 < x < 0.4$, is an insulator, and for $\sim 0.4 < x < 1$, is a superconductor. Numerous diffraction studies indicate that most oxygen vacancies occur within planes made of CuO chains (ab-plane) rather than within the pyramids. In $\text{YBa}_2\text{Cu}_3\text{O}_6$, the chains along the b-axis are oxygen depleted and Cu(1) coordination is only 2 (only two neighboring oxygen ions). This compound is an insulator. By increasing the oxygen concentration one gradually dopes the ab-plane with charge carriers (holes) and it eventually reaches the $\text{YBa}_2\text{Cu}_3\text{O}_7$ composition in which there are no oxygen vacancies. Very detailed studies indicate that the maximum in T_c is reached for $x \sim 0.93$ ($T_c = 94$ K) and that for $x = 1$ the critical temperature is lower, $T_c = 92$ K. The orthorhombic cell dimensions $\text{YBa}_2\text{Cu}_3\text{O}_7$ are : $a = 3.88 \text{ \AA}$, $b = 3.84 \text{ \AA}$, $c = 11.63 \text{ \AA}$, with a cell volume $\sim 173 \text{ \AA}^3$ [14]. Other rare earth compounds having the general formula, $\text{REBa}_2\text{Cu}_3\text{O}_7$, where RE represents one of the rare earth elements, that can replace yttrium in the original 123 structure of Fig. 1.2, are also found to exhibit superconductivity. However, an exception is $\text{PrBa}_2\text{Cu}_3\text{O}_7$ which does not exhibit superconducting properties to low temperatures.

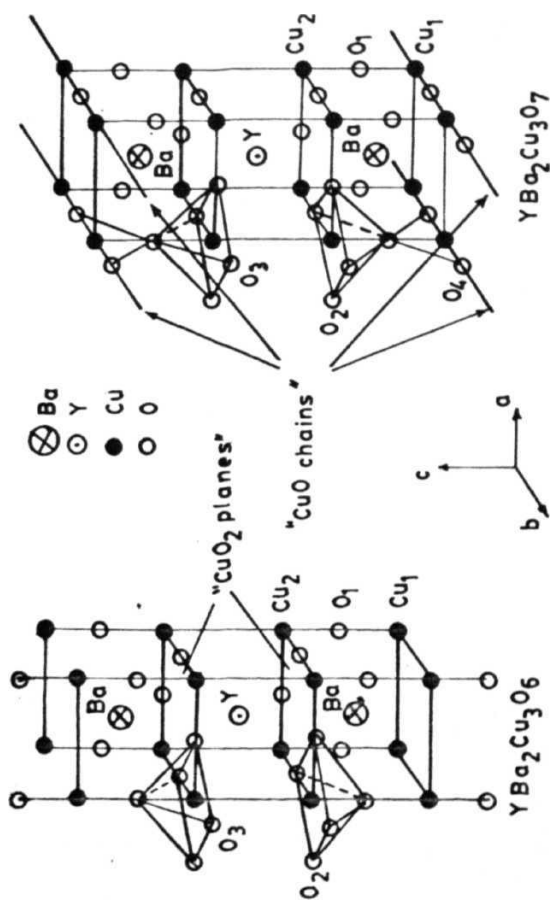


Fig. 1.2 Schematic diagrams of (a) $\text{YBa}_2\text{Cu}_3\text{O}_6$ an insulator and (b) $\text{YBa}_2\text{Cu}_3\text{O}_7$ superconducting oxide.

1.4 Preparation of bulk superconductors

1.4.1 Sintering

Sintering is commonly used in ceramic processing. In general sintered samples are prepared from starting powders by shaping them and then subjecting them to solid state reaction at high temperatures. Although sintering is very common and has many advantages in ceramic processing, it has failed to produce oxide superconductors with high J_c values, primarily due to the presence of weak-links at the grain boundaries. The weak link nature of grain boundaries is ascribed to impurity segregation, chemical or structural variation, the presence of nonsuperconducting phases, and cracking. It has also been pointed out that high angle grain boundaries are intrinsically weaklinks, due to a combination of small coherence length and a large anisotropy [16,17]. Because the J_c supported by the material is at least an order of magnitude more in the a-b plane than in the c-direction, many researchers have tried to align the grains in the preferred orientation, that is, along the ab plane. Sintering in magnetic fields or under uniaxial pressure was effective in aligning grains. However, the coupling between the grains was not drastically improved. Since sintering is a solid state reaction, the diffusion rate of atoms is not high enough to construct an ideal structure in large dimensions and it is likely that defects are created at grain boundaries. This problem of weak link nature of grains has been overcome by the process called melt textured growth [18].

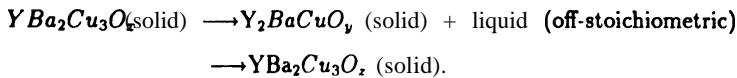
Sintering also causes substantial amount of shrinkage. In large green bodies of complex shapes, the retention of shape without distortions and cracks, and of the **main-**tainance of dimensional tolerances after sintering is a difficult task.

Ceramic components have also been produced by processes which involve the infiltration of molten metals into **shaped** preforms. Examples are the production of Reaction Bonded Silicon Carbide (**RBSI**) components and the Lanxide process for the production of ceramic matrix composites [19]. The advantage of such processes are the absence of shrinkage during processing enabling large shaped components to be made with a minimum of machining after the heat treatment.

1.4.2 Various melt growth processes

Melt Textured Growth process [18]

In order to obtain highly oriented samples, Jin *et al.*, [18] used a 'melt process' (Melt Textured Growth, MTG Process). The process can be understood with reference to Fig. 1.3 where a pseudo-binary Y-Ba-Cu-O phase diagram is shown. A sintered **YBa₂Cu₃O₇** sample is heated to 1100 °C to 1200 °C for decomposition and melting. The sequence of events during melting and subsequent solidification by slow cooling is



The melt textured samples prepared by this technique are essentially 100% dense, consisting of long platelet-shaped grains. The platelet axis appears to coincide with either the a or b direction in the orthorhombic phase. Such crystallographic alignment should be beneficial for the flow of supercurrent.

Modified MTG process [20]

For grain growth of the 123 phase, both the **Y₂BaCuO₅** (211) and the liquid must be

supplied. Therefore, when the distribution of the **211** is not uniform, the reaction will not proceed continuously where the **211** density is low. When the samples are cooled in the **211** + **L** region, the **211** grows to a large size and is distributed inhomogeneously, which will result in weak connectivity of the **superconducting** phase. In order to avoid coarsening of the **211** phase, several groups have modified the MTG process. For **example**, coarsening of **211** can be reduced by decreasing the heating temperature to the point just above the peritectic temperature. The connectivity of the superconducting phase could be greatly improved by such a modification and it is also found that the size of the **211** inclusions trapped in the **123** phase can be reduced down to the order of 1-5 microns.

Quenched and Melt Growth (QMG) process and Melt Powder Melt Growth (MPMG) Processes [21,22]

In this process sintered **123** sample or a mixture of calcined powders, are heated to the Y_2O_3 + **L** region (see Fig. 1.3) and quenched using copper plates. Here the sample consists of Y_2O_3 particles and the solidified liquid phase (a mixture of barium cuprates and amorphous phases).

The quenched material is then reheated to the **211** plus liquid region, where Y_2O_3 reacts with the liquid and produces the **211** phase. Since the **211** nucleates from Y_2O_3 , it is possible to control the distribution of the **211** phase if the distribution of Y_2O_3 is controlled. In the QMG process, the Y_2O_3 particles are segregated to some extent due to sedimentation, which causes a non-uniform distribution of the **211** phase. In the MPMG process, the melt quenched material is crushed into a fine powder and mixed well. By this process, coarse Y_2O_3 can be refined and its distribution can be made uniform. The pellets are rapidly heated to the **211** + **L** region. Here, the sample should not be kept for a long time since the **211** will grow into coarse grains. However, when the holding time is too short, the density of the sample will be poor and a number of pores will remain

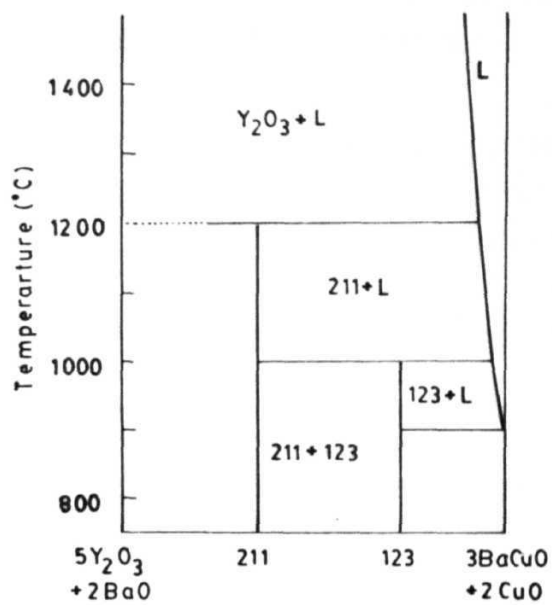


Fig. 1.3 A pseudobinary phase diagram for the Y-Ba-Cu-O system [46].

in the final microstructure. After an appropriate holding time in this region (20 min to 1 h), the sample is rapidly cooled down to a point just above the peritectic temperature and then very slowly cooled down to 850 to 900 °C. Through this process a uniform distribution of fine 211 in the textured 123 matrix is obtained.

Powder Melting Process

Instead of using the melt quenched powders in the first phase of MPMG process, it is possible to use a mixture of $\text{Y}_2\text{O}_3/\text{BaCuO}_2/\text{CuO}$ or a mixture of $\text{Y}_2\text{BaCuO}_5/\text{BaCuO}_2/\text{CuO}$ as starting materials [23,24]. They are heated to the 211 + L region and slowly cooled through the peritectic temperature as in the MPMG process. The microstructure of the PMP processed samples is essentially identical to that of MTG processed samples.

Platinum doped melt growth (PDMG) process

Ogawa *et al* [25] have found that a small amount Pt addition is effective in reducing the size of the 211 inclusions in the 123 matrix. The size reduction of 211 is explained based on the assumption that Pt acts as a nucleation site for the 211. However, recent works have shown that even when 211 phase particles are fine, they can grow to a large size in relatively short time when heated to the 211 + L region, but the grain growth can be reduced by Pt addition. Therefore Pt works so as to retard the Ostwald ripening of the 211 inclusions.

It has also been found that the addition of BaSnO_3 [26,27] and CeO_2 [28-31] are also effective in reducing the size of the 211 inclusions, thereby increasing J_c values.

OCMG process

Light rare earth $\text{REBa}_2\text{Cu}_3\text{O}_{7-\delta}$ (RE = Nd, Sm, and Gd) superconductors when processed in ambient atmosphere form solid solutions of type $\text{RE}_{1+x}\text{Ba}_{2-x}\text{Cu}_3\text{O}_{7-\delta}$, which have low T_c [32-35]. To suppress the low T_c phase formation, Yoo *et al.* [36] melt processed

in reduced oxygen partial pressures. In inert **atmosphere**, due to the absence of **oxygen**, $\text{RE}_{1+x}\text{Ba}_{2-x}\text{Cu}_3\text{O}_{7-\delta}$ phase formation is not promoted. Using this process, T_c of 95 K has been obtained in the $\text{NdBa}_2\text{Cu}_3\text{O}_{7-\delta}$ (**Nd-123**) system.

Seeding [37,38]

For most applications, bulk materials in usable shapes of large dimensions are needed. It has been demonstrated that single crystals of $\text{SmBa}_2\text{Cu}_3\text{O}_x$ and $\text{NdBa}_2\text{Cu}_3\text{O}_x$, which have a higher melting point than **Y-123**, can work as seeds for crystal growth and thus make it possible to control the crystal orientation. Long crystals with controlled orientation can be fabricated by this technique.

Directional solidification [39,40]

The former sections deal with solidification without sample transport. The motion of a sample relative to a temperature gradient can be employed to obtain long samples which are highly textured along the growth direction. The basic mechanism of grain growth is essentially the same as solidification without sample transport. The techniques used involve either moving a heating source or moving a sample through a hot zone. The latter technique is preferred from a commercial point of view, because it permits long samples to be processed in a continuous fashion. Lian *et al* [23] employed zone melting where $\text{Y}_2\text{BaCuO}_5/\text{BaCuO}_2/\text{CuO}$ powders are pressed in the form of bars and continuously melted and solidified by moving the samples through a tubular furnace which has a narrow high temperature zone for melting and a steep temperature gradient for unidirectional solidification. The temperature gradient (G) at 1000 °C was about 180 °C/cm, the microstructures obtained by this technique were identical to those by solidification without sample transport.

1.5 Magnetic response of HTSC

1.5.1 Critical state models

All the high T_c superconductors are type-II superconductors. To explain the hysteresis in the magnetization of type-II irreversible superconductors, critical state models [41-44] have been proposed. The models assume that penetrated supercurrents flow with a density equal to the critical current density, and that the flux vortex array is stable and there is no flux creep, and that the lower critical field is zero. Bean [41] derived the full hysteresis loop by assuming that the J_c is constant. But in high T_c superconductors, J_c is found to decrease with the applied field. Many workers assumed different functional behaviors of J_c . Examples are ;

Kim' model [42] : $J_c(H) = K/(H_o + H)$, where A' and H_o are constants;

Exponential Model [43,44] : $J_c(H) = \text{Exp} (-H/H_o)$;

Power-law model [45] : $J_c(H) = A' / H^n$, where n is a constant.

In the present study Bean, Kim, exponential and power law models are used to analyze the experimental data and to obtain physical parameters.

Bean's critical state model

The basic premise of this theory is that there exists a limiting macroscopic superconducting current density, $J_c(H)$, that a hard superconductor can carry, and further that any electromotive force, however small, will induce this full current to flow locally. This model assumes that the critical current density, J_c , is a constant, which means that it is independent of the local internal field, that the flux vortex array is stable and there is no flux creep, and that the lower critical field is zero. If this magnitude of current flows everywhere in the specimen, it is in the critical state. If we assume that this current density is independent of field, the process of magnetization of a slab of thickness D ($= 2a$) in a field parallel to its surface is shown in Fig. 1.4. The field within the specimen

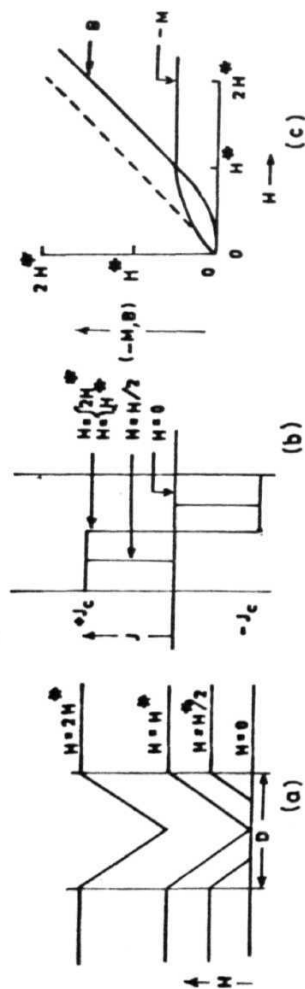


Fig. 1.4 A plot of local fields and current density, as well as magnetization curves, for fields 0 , $H^*/2$, H^* and $2H^*$ applied parallel to the surface of a slab of thickness D . The critical current density is assumed independent of field.

decreases linearly with distance as a consequence of Ampere's law, $\text{curl } \mathbf{H} = 4\pi \mathbf{J}/10$. In the initial stages of magnetization, the current flows in superficial layers whose thickness A is just enough to reduce the internal local field to zero, i.e, $A = 10H/4\pi J_c$. At fields of $H > \pi J_c D/5 = H^*$, currents flow through the entire volume of the specimen.

The volume average of the local field, by definition is

$$B = \int H dv / \int dv$$

$$M = B/\mu_o - H$$

In other words, B is merely the volume average of the local field while M is the average field created by the currents. For infinite slab, the initial magnetization curve, $M(H)$ becomes,

$$M = -H + H^2/2J_c a \quad 0 < H < H^*$$

$$M = -J_c a/2 \quad H > H^*$$

These results are sketched in Fig. 1.4(c). The reverse curve for the high $-H_m$ case is given by

$$M(H) = -J_c a/2 + H_m - H - (HH)^2/4J_c a \quad H_m - 2H^* < H < H_m$$

$$M(H) = J_c a/2 \quad -H_m < H < H_m - 2H^*$$

where H is the applied magnetic field, H_m is the maximum applied field, and a is half the thickness of a slab.

The critical current density of superconductors can be determined from magnetic measurements based on Bean's model, where J_c is constant. When H_m is larger than $2H^*$, J_c is related to the magnetization, M , for slab of thickness $2a$ as follows,

$$M(H)^+ - M(H)^- = J_c a.$$

Therefore, J_c can be calculated by measuring the width of a hysteresis loop at a given field, after the hysteresis loop is obtained.

For the **orthorhombic** sample,

$$M(H)^+ - M(H)^- = J_c a (1 - a/36)$$

where a and 6 are dimensions of the cross section of a sample, $b > a$.

1.5.2 Flux pinning [46]

Critical currents of type-II superconductors can be low due to the motion of vortices due to Lorentz force. It has to be prevented to have high critical current density. This can be achieved by the vortex pinning (or flux pinning), by creating normal sites out of which the vortex cannot leave without large energy increase [47]. The vortex will be pinned to such inclusions as it does not have to spend energy to destroy superconductivity in that inclusion. An inclusion is most **efficient** when its diameter is equal to the coherence length ξ , i.e, when the diameter of the tube which is in normal state within the vortex is equal to ξ .

A magnetic field enters a type-II superconductor to compensate for the energy needed to repel a magnetic field when the external field exceeds H_{c1} . The system can lower its total free energy by allowing the magnetic field to enter the superconductor, although the region where the fluxoid has penetrated locally loses the condensation energy. The loss of energy due to the penetration of fluxoid is thus called the penalty energy and is $H_c^2/2\mu_o$ per unit volume.

When the fluxoid interacts with the nonsuperconducting region, the penalty energy can be saved per interacted volume, since such a region is normal conducting. The saved energy is $U_p = (H_c^2/2)\pi\xi^2 d$, where d is the size of a nonsuperconducting particle. The

penalty energy must be paid to move the fluxoid from the normal superconducting region, whereby the fluxoids are pinned at normal regions.

The pinning force f_p is given by $f_p = dU_p/dx$ and in a simple case

$$= U_p/\xi = (H_c^2/2)\pi\xi d$$

This f_p is called an elementary pinning force. In the case of very small pinning centers, the interaction volume becomes $(4/3)\pi\xi^3$ and thus

$$f_p = (2H_c^2/3)\pi\xi^2$$

Since oxide superconductors are highly anisotropic, the pinning forces are also anisotropic and it depends on the direction of the field and the Lorentz force.

Bulk pinning force

The bulk pinning force, F_p , per unit volume, is the sum over all the contributions from various pinning centers, and if the number of interactions per unit volume is N , F_p becomes equal to Nf_p . Critical current density is then simply obtained from the relation

$$F_p = Nf_p = J_c B.$$

Flux pinning sites in melt textured YBCO

Melt processed YBaCuO contains many defects which may act as pinning centers. Those defects are twin planes [48-52], stacking faults [53-54], cracks, oxygen defects [55] and dislocations [56,57]. Presence of nonsuperconducting particles such as that of Y_2BaCuO_5 (Y-211) phase cause secondary defects in Y-123 matrix. Such defects occur only when the radius of curvature of the 123/211 interface is smaller than approximately $0.25\mu m$ [58,59]. In light RE-123, solid solution regions of the type $RE_{1+x}Ba_{2-x}Cu_3O_{7-\delta}$

whose T_c is lower than that of the stoichiometric 123 phase have been proposed to act as pinning centers [60-64].

Depairing critical current

There is an intrinsic critical current that a superconductor can support which is called depairing critical current. It is the current which destroys pairs and thus superconductivity. The maximum current is

$$J_c = (4/3\sqrt{6})H_c/\lambda_L$$

At 77 K, YBCO has a H_c of 0.3 T and a λ_L of 0.1 μm , which gives the ideal J_c value to be $2.4 \times 10^8 \text{ A/cm}^2$. This is three orders of magnitude larger than the required values, indicating that YBCO superconductors have intrinsically a potential for high J_c .

1.5.3 ac susceptibility

One of the most useful methods to study the magnetic properties of superconductors is to measure magnetization induced by ac magnetic fields. ac magnetization is usually evaluated as ac susceptibility. Measurements of the ac susceptibility, which is expressed as complex susceptibility, $\chi = \chi' - i\chi''$, have been used to determine the critical temperatures in conventional metallic superconductors [65] and recently, to determine the onset temperature for high T_c oxide superconductors [66]. It has provided important information on flux dynamics [67-72]. The real part of the susceptibility, χ' , represents diamagnetic shielding and the imaginary part, χ'' , represents bulk hysteresis loss. The ac field dependence of the loss peak in the susceptibility is analyzed to gain information on the movement of magnetic flux and the pinning strength.

1.5.4 Magnetic flux penetration

When magnetic fields are applied to a **type-II** superconducting sample, flux begins to penetrate into the sample preferentially from the regions with weaker pinning forces. Several kinds of the techniques for measurements of flux distribution have been reported. Higashida *et al.* [73] have found by the Bitter [6] decoration technique, that flux lines are trapped at 211 inclusions in melt-processed YBCO. Another method for the observation of dynamic flux behavior in superconductors was recently developed using magneto-optic Faraday effect in ferromagnetic iron garnet thin films [74-77]. The results clearly show that the critical state is established even in oxide superconductors and the 211 inclusions act as flux pinning centers. Many researchers measured the trapped field using a Hall probe in bulk melt textured samples [78,79] in order to characterize them for practical applications. There is another method for measuring the flux distribution in superconductors suggested by Campbell [80]. This is an inductive method, the penetration of the **flux** is detected by a lock-in amplifier operated in the wide-band mode. This was extensively used to study low T_c superconductors. In this thesis, we present the methodology of measuring the flux profiles using this technique and apply it to various samples.

1.6 Motivation and aim of the work

A polycrystalline high T_c superconductor is formed by small grains, typically a few microns in size, electrically coupled by weak links. This interconnected network [66] is supported by a nonsuperconducting matrix containing different impurities, voids and sometimes lower T_c superconducting phases. The most important limitation in the performance of these materials comes from the weak intergrain **connections**, which limit the current carrying capability and make the sample very sensitive to magnetic fields. **The**

weaklink nature of the grain boundaries can be avoided by grain alignment by melt textured growth. Through this process large values of bulk J_c could be obtained in YBCO, containing optimal amount of 211 inclusions and silver, even in the presence of external dc fields. Recently Yoo *et al.* [36] melt processed $\text{NdBa}_2\text{Cu}_3\text{O}_{7-\delta}$ (Nd-123) system in reduced oxygen atmosphere. This resulted in the samples with high J_c even in the high fields. A peak effect is seen in the $M - H$ loops [36,60]. This has been attributed to the presence of $\text{Nd}_{1+x}\text{Ba}_{2-x}\text{Cu}_3\text{O}_{7-\delta}$ phase inclusions which turn normal in the presence of high external fields [60-64].

The Y-211 inclusions modify practically all microstructural features of the melt processed Y-123 material : eg. platelet width, inter-platelet crack width, 211 size and morphology etc. The J_c of melt processed Y-123 is only a few hundreds of Amperes/cm² in the absence of Y-211 inclusions, but it increases by orders of magnitude when an optimal amount of Y-211 inclusions are incorporated into the Y-123 matrix. The low field J_c of stoichiometric Nd-123 is relatively small and there is a possibility of enhancing that by the addition of Nd-422 inclusions.

In order to study the effect of Nd-422 inclusions on the microstructural features and magnetic response, we have melt processed Nd-123 with various amounts of Nd-422 inclusions. The microstructural aspects are studied by polarized light optical and scanning electron microscopy. There exists some initial study on the effect of Nd-422 on the critical current density of melt processed Nd-123. The aim of the present work was to study quantitatively the variations of different microstructural parameters such as the platelet width, the width of the inter-platelet gaps, and the size and morphology of the Nd-422 inclusions as a function of Nd-422 concentration. Similarities and differences in the behavior between the two systems were expected to throw light on the mechanism

of microstructural evolution on melt processing in these samples. Experiments were also done by cooling the samples at different cooling rates through the peritectic temperature. The main purpose of these experiments was to isolate the microstructural features which are modified by solidification instabilities. It is also useful to know if the samples can be melt processed at faster rates which can be of practical use. Nd-123 has also been melt processed in this work, using a process called the Infiltration and Growth (IG) process. This process involves the infiltration of liquid phase into Nd-422 preforms at high temperatures and subsequent formation of textured Nd-123 by slow cooling through the peritectic temperature. This process, which is akin to the methods used for the fabrication of RBSC and lanxide composites, avoids shrinkage and distortions in the textured material. Macroscopic hollow regions which occur in the interior of conventionally melt processed samples are also avoided by the IG process. The IG process offers a means of making high J_c bulk products of large complex shapes with good dimensional tolerance and surface finish. The work described herein involves a study of an extension of the IG process to the Nd-123 system.

To avoid the possibility of forming low T_c solid solution phases of the formula $\text{Nd}_{1+x}\text{Ba}_{2-x}\text{Cu}_3\text{O}_{7-\delta}$, the samples were processed in flowing high purity Argon gas. In order to detect any low T_c phase left back, ac susceptibility was measured in bulk samples. Temperature variation of susceptibility at various ac field strengths was used to examine the nature of domain boundaries in the melt textured sample in comparison with the polycrystalline samples. The experimental data has been analyzed in terms of the critical state models.

Bulk melt textured samples, when processed without any imposed temperature gradient can contain more than one domain. Measuring the magnetization and J_c using a VSM or a SQUID magnetometer characterizes only small sized samples which are very

often single domain. The behavior of large sample would be governed to a large extent by the nature of the domain boundaries. Measurements on larger samples having several domains can be of practical value. Such measurements are demonstrated to be possible in this work, using a home-made facility, where flux profiles are measured. Measuring the flux distribution in the melt textured sample gives information about the weaklink regions. Flux distribution in sintered and various melt textured samples was measured using the home-made facility. The observations on the melt textured samples are correlated to the microstructural features of the samples. Critical current density could be obtained on a large sized samples. The features observed in the flux profiles of sintered samples could be simulated well using the critical state models. The effect of Nd-422 inclusion on melt textured samples has been studied using this technique. Magnetization measurements were also carried out on the samples using a SQUID magnetometer as a function of temperature and magnetic field. The melt processed Nd-123 samples with various amounts of Nd-422, and also the IG processed samples were studied. The behavior of J_c has been discussed as a function of the microstructural variations introduced through Nd-422 and compared with the data available on other RE-123 system.

References

- [1] H. Kammerlingh Onnes, Leiden Commun., **120b**, 1226 (1911).
- [2] W. Meissner and R. Ochsenfeld, *Naturwissenschaften* **21**, 787 (1933).
- [3] J. Bardeen, L. N. Cooper and J. R. Schrieffer, *Phys. Rev.* **108**, 1175 (1957).
- [4] F. London and H. London, *Physica* **2**, 341 (1935).; F. London and H. London, *Z. Phys.* **96**, 359 (1935).
- [5] A. A. Abrikosov, *Soviet Phys. JETP* **5**, 1774 (1957).
- [6] F. Bitter, *Phys. Rev.* **38**, 1903 (1931).
- [7] A. B. Pippard, *Physica* **19**, 765 (1953).; A. B. Pippard, *Proc. R. Soc. London, A* **216**, 547 (1953)
- [8] J. G. Bednorz and K. A. Muller, *Z. Phys. B* **64**, 189 (1986).
- [9] M. K. Wu, J. R. Ashburn, C. J. Torang, P. H. Hor, R. L. Meng, L. Gao, Z. J. Huang, Y. Q. Wang and C. W. Chu, *Phys. Rev. Lett.*, **58**, 908 (1987).
- [10] H. Maeda, Y. Tanaka, M. Fukutomi and T. Asano, *Jap. J. Appl. Phys.*, **27**, L209 (1988).
- [11] Z. Z. Sheng and A. M. Hermann, *Appl. Phys. Lett.* **52**, 1738 (1988).
- [12] S. N. Putilin, E. V. Antipov, O. Chmaissem and M. Marezio, *Nature* **362**, 226 (1993).
- [13] A. Schilling, M. Cantoni, J. D. Guo and H. R. Ott, *Nature* **363**, 56 (1993).
- [14] *Introduction to Superconductivity and high T_c Materials*, M. Cyrot and D. Pavuna *World Scientific Publishing Co. P 169*. (1992).
J. M. Bell, *Phys. Rev. B* **37**, 541 (1988).
R. J. Cava, *Scientific American*, Aug. **42** (1990).
- [15] M. Onoda, S. I. Shamoto, M. Sato and S. Hosoya, *Jpn. J. Appl. Phys.* **26**, L876 (1987).
- [16] D. Dimos, P. Chaudhari and J. Mannhart, *Phys. Rev. B*, **41**, 4038 (1990).
- [17] S. E. Babcock, X. Y. Cai, D. L. Kaiser and D. C. Larbalestier, *Nature* **347**, 167 (1990).
- [18] S. Jin, T. H. Tiefel, R. C. Sherwood, M. E. Davis, R. B. van Dover, G. W. Kammlott, R. A. Fastnacht and K. D. Keith, *Appl. Phys. Lett.* **52**, 2074 (1988).
- [19] A. W. Urquhart, *Mater. Sci. Engg.* **A144**, 75 (1991).
- [20] K. Salama, V. Selvamanickam, L. Gao and K. Sun, *Appl. Phys. Lett.* **54**, 2352 (1989).
- [21] M. Murakami, M. Morita, K. Doi, and K. Miyamoto, *Jpn. J. Appl. Phys.* **28**, 1189 (1989).
- [22] H. Fujimoto, M. Murakami, S. Gotoh, N. Koshizuka and S. Tanaka, *Advances in Superconductivity* **2**, 285 (1990).
- [23] Z. Lian, Z. Pingxian, J. Ping, W. Keguang, W. Jingrong and W. Xiaozu, *Supercond. Sci. Tech.* **3**, 490 (1990).
- [24] Z. Lian, Z. Pingxian, J. Ping, W. Keguang, W. Jingrong and W. Xiaozu, *IEEE Trans. Mag.* **27**, 912 (1991).
- [25] N. Ogawa, I. Hirabayashi and S. Tanaka *Physica C* **177**, 101 (1991).
- [26] P. J. McGinn, W. Chen, N. Zhu, C. Varanasi and S. Sengupta, *Appl. Phys. Lett.* **59**, 120 (1991)
- [27] C.J. Kim, K. B. Kim, and G. W. Hong, *Physica C* **232**, 163 (1994).
- [28] N. Vilalta, F. Sandiumenge, S. Pinol And X. Obradors, *J. Mater. Res.* **12**, 38 (1997).

- [29] **S. Pinol**, **F. Sandiumenge**, **B. Martinez**, **V. Gomis**, **J. Fontcuberta**, **X. Obradors**, **E. Snoeck** and **Ch. Roucau**, *Appl. Phys. Lett.* **65**, 1448 (1994).
- [30] **C.J. Kim**, **K.B. Kim**, **G.W. Wong**, **D.Y. Won**, **B.H. Kim**, **C.T. Kim**, **H.C. Moon**, and **D. S. Suh**, *J. Mater. Res.* **7**, 2349 (1992).
- [31] **C.J. Kim**, **K.B. Kim**, **D.Y. Won**, **H.C. Moon**, **D. S. Suh**, **S. H. Lai** and **P.J. McGuinn**, *J. Mater. Res.* **9**, 1952 (1994).
- [32] **K. Takita**, **H. Katoh**, **H. Akinaga**, **M. Nishino**, **T. Ishigaki** and **H. Asano**, *Jpn. J. Appl. Phys.* **27**, L57(1988).
- [33] **S. I. Yoo**, **R. W. Mc Callum**, *Physica C* **210**, 147 (1993).
- [34] **M. J. Kramer**, **A. Karion**, **K. W. Dennis**, **M. park** and **R. W. McCallum**, *J. Electron. Mater.* **23**, (1994).
- [35] **T. B. Lindemer**, **E. D. Specht**, **P. M. Martin** and **M. L. Flitcroft**, *Physica C* **255**, 65 (1995).
- [36] **S. I. Yoo**, **N. Sakai**, **H. Takaichi** and **M. Murakami**, *Appl. Phys. Lett.* **65**, 633 (1994).
- [37] **M. Muarakami**, **T. Oyama**, **H. Fujimoto**, **T. Taguchi**, **S. Gotoh**, **Y. Shiohara**, **N. Koshizuka**, and **S. Tanaka**, *Jpn. J. Appl. Phys.* **29**, L1991 (1990).
- [38] **U. Balachndran**, **W. Zhong**, **C. A. Youngdahl**, and **R. B. Peoppel**, *J. Electron. Mater.*, **22**, 1285 (1993).
- [39] **T. Izumi**, **Y. Nakamura** and **Y. Shiohara**, *J. Mater. Res.* **7**, 1621 (1992).
- [40] **P. McGinn**, **W. Chen**, **N. Zhu**, **M. Langan** and **U. Balachandran**, *Appl. Phys. Lett.* **57**, 1455 (1990).
R. Meng, **C. Kinalidis**, **Y. Sun**, **L. Gao**, **P. H. Hor**, and **C. W. Chu**, *Nature* **345** 326 (1990).
V. Selvamanickam, **C. Partsinevelos**, **A. V. McGuire** and **K. Salama**, *Appl. Phys. Lett.*, **60**, 3313 (1992).
- [41] **C P. Bean**, *Phys. Rev. Lett.* **8**, 250 (1962); *Rev. Mod. Phys.* **36**, 31 (1964).
- [42] **Y. B. Kim**, **C. F. Hempstead** and **A. R. Strnad**, *Phys. Rev. Lett.* **9**, 306 (1962).
Y. B. Kim, **C. F. Hempstead** and **A. R. Strnad**, *Phys. Rev.* **129**, 528 (1963).
- [43] **G. Ravi Kumar** and **P. Chaddah**, *Phys. Rev. B* **39**, 4704 (1989).
- [44] **W. A. Fietz**, **M. R. Beasley**, **J. Silcox**, and **W. W. Webb**, *Phys. Rev.* **136**, A335 (1964).
V. R. Karasik, **N. G. Vasil'ev**, and **V. G. Ershov**, *Sov. Phys. JETP* **32**, 433 (1971)
- [45] **F. Irie** and **K. Yamafuji**, *J. Phys. Soc. Jpn.*, **23**, 255 (1967).
- [46] *"Melt processed high temperature superconductors"*, ed. **M. Murakami**, world Scientific, Chapter 10.
- [47] **A. M. Campbell** and **J. E. Evetts**, *Adv. Phys.* **21**, 199 (1972).
- [48] **W. Gawalek**, **W. Schppel**, **R. Hergt**, **W. Andara**, **K. Fishcer** and **P. Gornert**, *Supercond. Sci. Technol.* **5**, S407 (1992).
- [49] **L. J. Swartzendruber**, **A. Ritburd**, **D. L. Kaiser**, **F. W. Gayle** and **L.H. Bennett**, *Phys. Rev. Lett.* **64**, 483, (1990).
- [50] **U. Welp**, **W. K. Kwok**, **G. W. Crabtree**, **K. G. Wandervoort** and **J. Z. Liu**, *Appl. Phys. Lett.* **57**, 84 (1990).
- [51] **W. Gawalek**, **W. Schppel**, **R. Hergt**, **W. Andara**, **K. Fishcer** and **P. Gornert**, *Supercond. Sci. Technol.* **5**, S407 (1992).
- [52] **L. J. Swartzendruber**, **A. Ritburd**, **D. L. Kaiser**, **F. W. Gayle** and **L.H. Bennett**, *Phys. Rev. Lett.* **64**, 483, (1990).

- [53] K. Yamaguchi, M. Murakami, H. Fujimoto, S. Gotoh, N. Koshizuka and S. Tanaka; Jpn. J. Appl. Phys. 29, L1428 (1990).
- [54] K. Yamaguchi, M. Murakami, H. Fujimoto, S. Gotoh, T. Oyama, Y. Shiohara N. Koshizuka and S. Tanaka; J. Mater. Res. 6, 1404 (1991).
- [55] M. Daeumling, J. M. Seutjens and D. C. Larbalestier: Nature **346**, 332 (1990)
- [56] P. Diko, W. Gawalek, T. Habisreuther, T. Klupsch, and P. Gornert, Phys. Rev. B 52 13658 (1995).
- [57] Z. L. Wang, A. Goyal, and D. M. Kroeger, Phys. Rev. B, **47**, 5373 (1993).
- [58] M. Mironova, D. F. Lee and K. Salama, Physica C **211**, 188 (1993).
- [59] R. Gopalan, T. Roy, T. Rajasekharan, G. Rangarajan and N. Hari Babu, Physica C **244**, 106 (1994).
- [60] M. Murakami, S. I. Yoo, T. Higuchi, N. Sakai, J. Weltz, N. Koshizuka, and S. Tanaka, Jpn. J. Appl. Phys. **33**, L715 (1994).
- [61] M. Murakami, Supercond. Sci. Tech., 9 [12] 1015 (1996).
- [62] T. Egi, J. G. Wen, K. Kuroda, H. Unoki and N. Koshizuka, Appl. Phys. Lett. 67, 2406 (1995).
- [63] M. Nakamura, T. Hirayama, Y. Yamada, Y. Ikuhara and Y. Shiohara Jpn. J. Appl. Phys., Part 1, 35, 3882 (1996).
- [64] W. Ting, T. Egi, K. Kuroda, N. Koshizuka and S. Tanaka, Appl. Phys. Lett., **70**, 770 (1997).
- [65] T. Ishida and H. Mazaki, Phys. Rev. B 20, 131 (1979).
T. Ishida and H. Mazaki, J. Appl. Phys. **52**, 6798 (1981).
- [66] J. R. Clem, Physica C 153-155, 50 (1988)
M. Nikolo and R. B. Goldfarb, Phys. Rev. B 39, 6615 (1988).
- [67] D. X. Chen, A. Sanchez, T. Puig, L. M. Martinez, and J. S. Muñoz, Physica C **168**, 652 (1990).
- [68] T. Ishida and R. B. Goldfarb, Phys. Rev. B 41, 8939 (1990).
- [69] L. Ji, R. H. Sohn, G. C. Splading, C. J. Lobb and M. Tinkham, Phys. Rev. B 40, 10936 (1989).
- [70] Y. Kim, Q. Harry Lam and C. D. Joffries, Phys. Rev. B 43, 11404 (1991).
- [71] X. C. Jin, Y. Y. Xue, Z. J. Huang, J. Bechtold, P. H. Hor and C. W. Chu, Phys. Rev. B **47**, 6082 (1993).
- [72] M. G. Karkut, M. Slaski, L. K. Sagdahl, and K. Fossheim, Physica C **215**, 19 (1993).
- [73] Y. Higashida, Y. Kubo, M. Murakami, H. Fujimoto, K. Yamaguchi, T. Takata; A. Kondoh and N. Koshizuka, Physica C **185-189**, 2653 (1991).
- [74] Th. Schuster, M. R. Koblishka, H. Kuhn, M. Glücker, B. Ludescher, and H. Kronmüller, J. Appl. Phys. **74**, 3307 (1993).
- [75] M. R. Koblishka, Th. Schuster and H. Kronmüller, Physica C 219, 205 (1994).
- [76] S. Gotoh and N. Koshizuka, Physica C **176**, 300 (1991).
- [77] M. V. Indenborn, N. N. Kolesnikov, M. P. Kulakov, I. G. Naumenko, I. Nikitenko, A. A. Polyanskii, N. F. Vershinin and V. K. Vlasko-Vlasov, Physica C **166** 486 (1990).
- [78] I. Chen, J. Liu, R. Weinstein and K. Lau, J. Appl. Phys. 72, 1013 (1992); Y. H. Zhang, A. Parikh and K. Salama, IEEE Trans. Appl. Supercond., 7, 1787 (1997).
- [79] H. Fujimoto, T. Higuchi, K. Kawano and T. Ban, IEEE Trans. Appl. Supercond., 7, 1124 (1997).
- [80] A. M. Campbell, J. Phys. C 2, 1492 (1969).

Chapter 2

Experimental Techniques

In this chapter, the principles and details of the experimental techniques used in the present work are discussed. Special emphasis is given on the methodology of measuring flux profiles. The experimental setup used for measuring the flux profiles, and its calibration, are discussed.

2.1 Optical microscope

The optical microscope is an instrument that magnifies and resolves the structure of objects and it is the most widely used instrument in metallography/ceramography. It consists of four components : A light source, condenser lens, objective lens and eyepiece. The condenser collects light rays from the light source which are focused onto the specimen. The objective lens forms a real, magnified aerial image of the object in the intermediate image plane. This real image is further magnified by the eyepiece to form the final image. The magnification of the objective is given by the ratio $\frac{L}{f}$, where L is the distance between the eyepiece and the objective and f is the focal length of the objective lens.

Polarized light was used extensively to get microstructural features with clear contrast and also surface anisotropy. By introducing a polarizer into the condenser lens system the specimen is illuminated with plane polarized light, i.e, the wave vector is parallel to

a particular plane and thus giving a direct measure of the phase change at the reflecting surface. Application of polarized light microscopy includes the study of grain size and shape, preferred orientation, twinning and phase distribution which are all effectively delineated. A Lietz reflected light microscope with the facility for polarized light was used in this work.

Sample preparation for optical observation

In all metallographic methods emphasis is given to the need for effective sample preparation. Small pieces were cut from the bulk samples, and they were mounted in bakelite metallographic mounts. The mounted specimens were initially ground on coarse silicon carbide paper to get a flat surface. Methanol was used to wash the sample. The samples thus ground were subjected to final polishing on a diamond cloth with diamond pastes of 6 μm , 1 μm , and 0.25 μm . Polishing time with each paste was 4-6 h. The polished surface of the sample was later cleaned with fine polishing cloth. The samples thus prepared were examined using the optical microscope.

2.2 Scanning Electron Microscope

In a scanning electron microscope (SEM) the specimen is scanned with a finely focused electron beam of kilovolt energy. An image is formed by scanning a cathode-ray tube in synchronism with the beam and by modulating the brightness of this tube with beam-excited signals. In this way, an image is built up point-by-point which shows the variations in the generation and collection efficiency of the chosen signal at different points on the specimen.

An important feature of the SEM is that a variety of images can be obtained from the signals from the specimen, like back scattered image, related to the atomic weight of the constituent phase from the back scattered electrons. Also the X-ray and Auger

electrons available in the SEM can provide further information about the composition at the specimen surface.

In the present study A JEOL JSM 840 scanning electron microscope was used. Even though the superconducting NdBaCuO samples are electrically conducting in the normal state, silver paint was used as conducting material to avoid charge accumulation on the specimens during observation.

2.3 Quantitative analysis of microstructures

Since direct observation of a three dimensional microstructure is extremely difficult, quantitative analysis of microstructural features are usually obtained from the measurements made on two dimensional micrographs. The basic principle employed is that the volume fraction of a phase is equal to the area fraction in a random planar section and is **equal** to the linear fraction in a random linear line through the three dimensional microstructure. The volume fraction of a phase is also equal to the point fraction of randomly distributed points which lie within that particular phase [1].

$$V_f = \frac{V_\alpha}{V} = A_f = \frac{A_\alpha}{A} = L_f = \frac{L_\alpha}{L} = P_f = \frac{P_\alpha}{P} \quad (2.3.1)$$

V_f = Volume fraction of α phase

V_α = Volume of a phase in the specimen

V — Total volume of the specimen.

A_f = Area of a phase in a random planar section.

L_f = Linear fraction of α phase in a random linear line.

L_α = Line fraction of a phase in a random linear line.

L = Total length of random linear line.

P_f = Point fraction of α phase.

P_{α} = Number of random points falling in the α phase.

P = Total number of random points.

The results quoted are the average of several measurements.

Measurement of grain size

In metallographic research the most widely used method for the measurement of grain size is the mean linear intercept method. In this method a linear transverse is made on the micrograph, the transverse length L from one grain boundary to the next is measured and the number of grains N counted. The average grain size d is given by

$$d = \Sigma L / N \quad (2.3.2)$$

In the present study, grain size measurements in the microstructure of melt grown samples were carried out by the linear intercept method.

2.4 X-ray diffractometer

A knowledge of the crystal structure of materials is essential in understanding their properties and in identifying them, in predicting their behavior under various conditions, and for the characterization of the material at all stages of its preparation. The reproduction of materials with tightly controlled properties often requires X-ray analysis. Although single crystals are preferred for determining crystal structures of new materials, some materials are available only as small polycrystals. Many structures are already known, and the available information is used with the powder method in many types of studies.

The principal uses of the X-ray powder method are

- (a) identification of crystalline phases, including qualitative and quantitative analysis of mixtures of phases.
- (b) distinguishing between mixtures, various types of solid solutions.

- (c) precision measurement of lattice parameters and crystalline states.
- (d) determination of the degree of preferred orientation and crystalline texture

Principle

When a beam of parallel monochromatic X rays of approximately 0.1 nm wavelength strikes a crystal, the crystal acts as a three-dimensional diffraction grating and produces an X-ray diffraction pattern. This diffraction consists of a three dimensional array of reflections which satisfy the conditions of Bragg's law :

$$n\lambda = 2 d \sin \theta$$

where n is a small integer giving the order of diffraction, λ is the wavelength of the incident X rays, d is the distance between a set of parallel lattice planes, and θ is the angle between the incident X-ray beam and the atomic lattice plane in the crystal.

The reflection angle for a particular set of lattice planes (hkl) is

$$2\theta = 2\sin^{-1}\left[\frac{\lambda}{2d_{(hkl)}}\right]$$

where (hkl) are the Miller indices defining the orientation of the plane with respect to the crystallographic axes.

The powder pattern is a set of reflections in which the lattice spacings and the relative intensities are unique from each crystalline substance. It is this property that makes it possible to identify a substance by comparing its pattern with that of a known substance.

Similar crystal structures give similar x-ray patterns in which the peak positions will be shifted if the materials have different lattice parameters. The lattice spacing d is related to the lattice parameters a_0 in cubic crystals by

$$d_{(hkl)} = \frac{a_0}{(h^2 + k^2 + l^2)^{1/2}}$$

The lower symmetry crystal systems require additional terms.

In the present study we have used a Siemens X-ray **diffractometer** with Cu K_{α} radiation, whose characteristic wavelength is 1.5418 Å. Diffraction lines corresponding to various (hkl) values are recorded in the 2θ range from 20° to 60° and the lattice parameters a , b , and c are calculated from them using a powder diffraction computer package.

2.5 dc electrical resistivity

The electrical resistivity measurements are performed using a home-made apparatus which employs the dc four probe technique. This technique avoids contact resistance. The contacts are made using silver paint with the two outer leads as the current leads and the two inner leads as the voltage leads. The heater wire is wound astatically around the sample holder to heat the sample above the liquid nitrogen temperature. A copper-constantan thermocouple is used to measure the sample temperature. Sample temperatures could be varied upto room temperature from 77 K.

Block diagram of the experimental set up for precise dc electrical resistivity measurements is shown in Fig. 2.1. Constant dc electrical current (I) was supplied to the sample using a Keithley 224 constant current source. A Keithley 181 **nanovoltmeter** was used to measure the voltage drop across the inner leads. To avoid the **thermo e.m.f** due to thermal gradient across the sample, the voltage drop across the inner leads was measured for both the forward (V_1) and reverse (V_2) directions of the current (I) and the resistance was calculated as $R = (V_1 - V_2)/(2I)$. The resistivity is given by RA/l , where A is the area of cross section of the sample normal to the direction of the current, and l is the distance between the voltage leads. The error in the measured resistivity is $\pm 1 \mu\Omega\text{-cm}$.

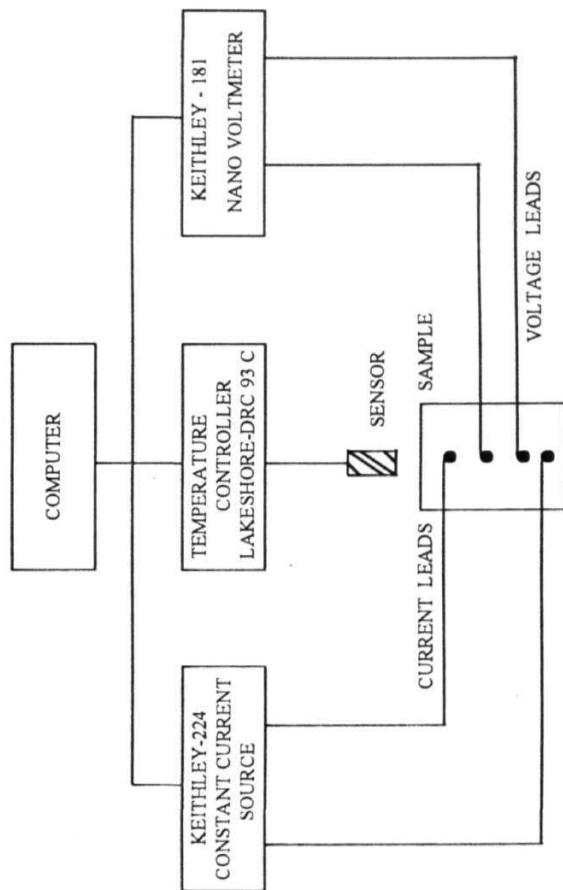


Fig. 2.1 Block diagram of dc electrical resistivity measurement setup.

2.6 ac susceptibility

Principle

The ac susceptibility measurement is based on a mutual inductance coil assembly where a primary coil and two secondary coils with equal number of turns mounted **co-axially**, form the basic unit of the measuring circuitry. In the absence of a sample, the voltage across the secondary coils is zero. In the presence of a sample the induced magnetization due to the ac field in primary coil, will result in off-balance signal of the secondary coils detection system.

Coil assembly and the bridge design

Secondary coils are first wound in 3 cm with an equal number of turns (1250). A 6cm long homogeneous primary coil is wound over the secondaries. Secondary coils are connected in series opposition to give a null output in the absence of a sample. A voltage from a Wavetek 178 waveform synthesizer is applied to the primary coil and off-balance signal from the pair of secondary coils, when the sample is introduced in center of one of the secondaries, is detected using a **EG&G PAR 5210** dual phase lock-in amplifier (**LIA**). A synchronous signal from the Wavetek is fed to the reference channel of the lock-in amplifier. Voltage drop across a standard 10 ohm resistor connected in series with the primary coil is measured using a Kiethley 196 multimeter to calculate the field generated by the primary coil. The temperature of the sample is measured using the copper-constantan thermocouple. All the instruments are controlled through IEEE 488 interface and the data were acquired using a personal computer.

The field produced by a current at any point in a solenoid, is given by

$$H_{rms} = \frac{4\pi N_p I_{rms}}{10L_p} \quad (2.6.1)$$

where N_p is number of turns in the primary coil, L_p is the length of the primary coil in cm and I_{rms} is rms value of the current through the primary coil. The field amplitude H_{ac} in Oe is $\sqrt{2}H_{rms}$.

When the induced voltage in the secondaries is sensed at the input of the dual phase LI A, it gives out a signal in the form of dc voltages ϵ_R, ϵ_I proportional to the real and imaginary parts of M that are in phase and out of phase, respectively, with respect to the applied ac field. In practice, the net output from secondaries is often non-zero even in the absence of any sample and this is eliminated by subtracting the measured background signal from the signal measured after inserting the sample under the same conditions. Additionally, there is a need to correct for the extraneous phase shifts arising from various sources in the setup. This is done by shifting the phase of the references so as to obtain $\chi'' - 0$ well above T_c as well as well below T_c .

The measured voltages ϵ_R, ϵ_I , are related to χ_R and χ_I as [2]

$$\chi_R = \frac{\epsilon_R}{\alpha \omega A N \mu_o H_m (1 - D)} \quad (2.6.2)$$

$$\chi_I = \frac{\epsilon_I}{\alpha \omega A N \mu_o H_m (1 - D)} \quad (2.6.3)$$

Here, N is the number of turns of the secondary across the sample, H_m is the amplitude of the applied ac field, A is the area of cross section of the sample, D is the demagnetization factor and α is the filling factor [3]. The absolute values of susceptibility for non-zero demagnetization (D) values are calculated using the expressions given by Murphy [2]

$$\chi'_1 = \frac{\chi_R - D(\chi_R^2 + \chi_I^2)}{(1 - \chi_R D)^2 + D^2 \chi_I^2} \quad (2.6.4)$$

$$\chi''_1 = \frac{\chi_I}{(1 - \chi_R D)^2 + D^2 \chi_I^2} \quad (2.6.5)$$

Following this procedure, the temperature variation of χ'_1 and χ''_1 are obtained from the measured temperature dependence of ϵ_R, ϵ_I .

2.7 Magnetic flux profile measurements

The magnetic flux profiles are measured using an ac inductive method suggested by Campbell [4].

Coil assembly

Coil assembly to measure the flux profiles is similar to the one which is used for ac susceptibility measurements. Two secondary coils (S1 and S2) with equal number of turns (1115) are first wound on two ends of the perspex cylinder within 12 mm length of each one. A 3.76 cm long homogeneous primary coil (P) to generate ac field is wound over the secondaries. Secondary coils are connected in series opposition to give a null output in the absence of a sample. The size of the coil assembly is chosen so as to fix it in between the poles of a dc electromagnet (Bruker-make). The maximum dc magnetic field that could be applied in this measurement was 1 T at 7 cm pole gap. The experimental setup used for the study is given in Fig. 2.2. The coil assembly is very rigidly fixed between the commercial dc electromagnet poles in order to avoid any relative displacement. A temperature sensor (TS) is placed near the sample. A wave form synthesizer (wavetek 178) is used to generate sinusoidal ac field in primary coil. The voltage across the standard 10 Ω resistor is measured using Keithley 196 digital multi meter (DMM) and this provides a measure of the alternating field applied to the specimen. A maximum ac field of 100 Oe can be obtained with this setup. The TTL output of the wavetek is a square wave with the same frequency and phase as of the voltage applied to the coil generating the ac magnetic field and it is used as the reference signal to the lock-in amplifier (Princeton applied research EG&G model 5210). It is operated in wide-band mode, where it measures all the harmonics of the signal without filtering. All these equipment are controlled by a computer through general purpose interfacing bus (GPIB) card.

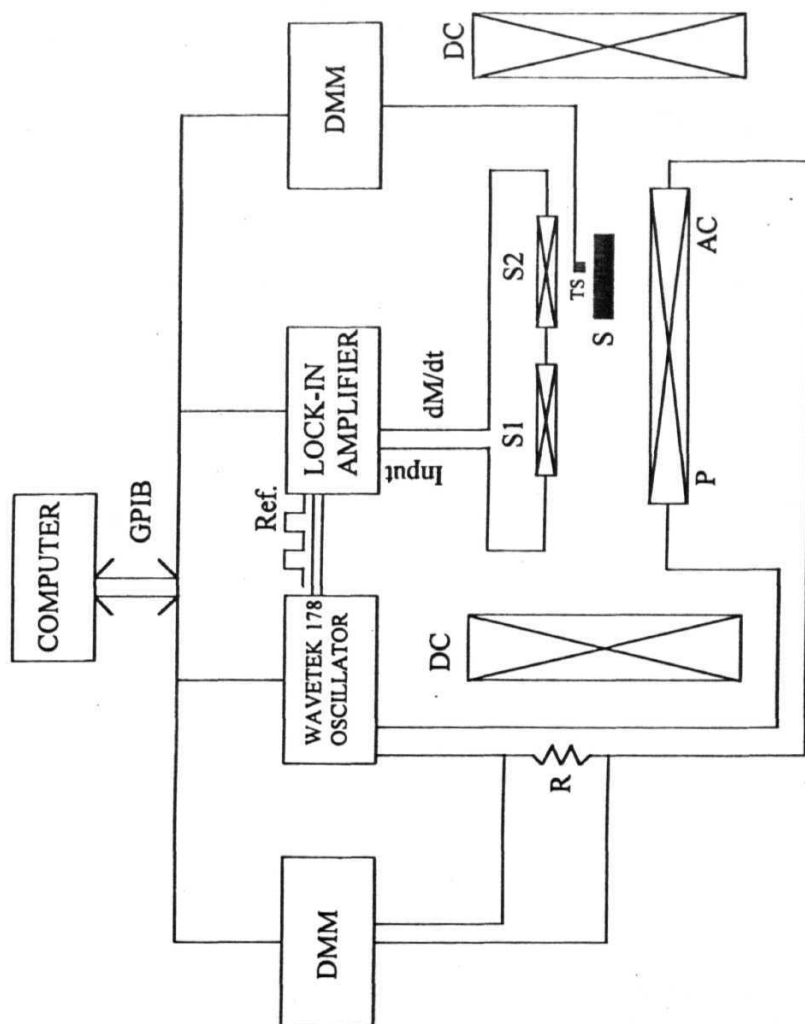


Fig. 2.2 Block diagram of ac magnetic susceptibility/flux profile measurement setup.

ac (33 Hz) and dc fields were applied along the sample length. When the sample is placed in one of the secondary coils the resultant output of secondaries is proportional to the rate of change of magnetization (dM/dt). Campbell [4] and other workers [5-7] have reported a sensitive method in which a lock-in analyzer operated in the flat-band mode is used for performing the integration of dM/dt . The lock-in output is proportional to

$$\int_{\theta}^{\theta+\pi} \frac{dM}{dt} = C \{M(\theta + \pi) - M(\theta)\}$$

where M is the magnetization of the specimen and C is a constant of the apparatus. The in-phase signal, which can be measured by the lock-in amplifier, refers to any signal produced by the flux motion in phase with the oscillating field. Thus it gives the magnetization of the specimen at the peaks of the ac field.

In general, ac field amplitudes are sufficiently small so that J_c is independent of field over the amplitude of the ac signal. If the amplitude H_{ac} is increased by δH_{ac} the extra flux introduced at the peak is

$$\delta\phi = \delta H_{ac}(\pi R^2 - \pi r^2),$$

where r is the radius to which the field has penetrated and R is the radius of the specimen. Hence, if S is the in-phase signal,

$$\begin{aligned} \frac{dS}{dH_{ac}} &= 2C \frac{dM}{dH_{ac}} \\ &= \frac{2C\pi}{\pi R^2} (R^2 - r^2 - R^2) \\ &= -K \frac{r^2}{R^2} \end{aligned}$$

The constant K is determined as the signal per Gauss, when the sample is in perfect Meissner state. The above equation can be rewritten to get the penetration depth, p as

$$p = R - r = R(1 - \sqrt{\frac{-1}{K} \frac{dS}{dH_{ac}}}) \quad (2.7.1)$$

The in-phase signal is measured as a function of the amplitude of the ac field at 77K for all the samples. This is repeated at various fixed dc fields. Flux profiles are obtained by plotting p/R as a function of ac field amplitude.

Calibration of the penetration depth

When the sample is in one of the secondary coils, the output of pair of the secondaries is given by [5-7],

$$\mu_o \alpha N V \omega (1 - D) \frac{dM(\theta)}{d\theta}$$

where N is the number of turns per unit length of the secondary coil, V is the volume of the sample, ω is the angular frequency of the applied ac field, D is the demagnetization factor of the sample, a is the filling factor [3], and $M(\theta)$ is the magnetization at a phase angle θ . The in-phase signal measured by the lock-in amplifier in the flat band mode is given by

$$S = 4\mu_o \alpha N V f (1 - D) M(\theta = 0)$$

$$S = KM$$

Where $K = 4\mu_o \alpha N V f (1 - D)$ is the calibration factor.

2.8 SQUID magnetometer

Principle

A superconducting quantum interference device (SQUID) is used to determine the magnetic moment of a material, in a SQUID magnetometer. The squid response signal is a periodic function of the magnetic flux. The period of this function equals the flux quantum. The magnetic moment due to the specimen is measured by monitoring the change in flux through the pickup coil as the specimen is moved through another coil

in the feed back loop to offset the change in field at SQUID and the voltage output is directly proportional to the feed back current. Therefore the change in field at the main pick-up coil is read as an output voltage from the squid controlling electronics, i.e. $\Delta V_{SQUID} \propto \Delta \Phi$, where Φ is the magnetic flux through the pick-up coil. The magnetic moment of the specimen is then obtained from the SQUID response curve with the help of various algorithms. The SQUID magnetometer used in the present work is a fully automated, computer controlled one from Quantum design.

References

- [1] " *The basis of quantitative metallography*" ed. F. B. Pickering, Institute of Metallurgical Technicians, Monograph No.1.
- [2] S. D. Murphy, K. Renouard, R. Crittenden and S. M. Bhagat, *Solid State Commun.* **69**, 367 (1989).
- [3] M. Couach and A. F. Khoder, in " *Magnetic Susceptibility of Superconductors and Other Spin Systems*" edited by R. A. Hein, T.L.Francavilla, and D. H. Liebenberg (Plenum, New York, 1992).
- [4] A. M. Campbell, *J. Phys. C* **2**, 1492 (1969).
- [5] F. Gömöry, *Rev. Sci. Instrum.* **62**, 2019 (1991).
- [6] H. Jiang and C P Bean, *Rev. Sci. Instrum.* **66**, 3284 (1995).
- [7] G. E. Gough, M. S. Colclough, D. A. O'Conner, F. Wellhofer, N. McN. Alford, and T. W. Button, *Cryogenics* **31**, 119 (1991).

Chapter 3

Melt processing and microstructure of NdBCO superconductor

In this chapter the optimization for melt processing of $\text{NdBa}_2\text{Cu}_3\text{O}_{7-\delta}$ (Nd-123) superconductor with respect to the processing atmospheres, temperatures, and low temperature oxygen loading is described. The microstructural features just after melting at the **pro-peritectic** stage and after the final stage of processing (i.e, after completion of the peritectic reaction) are discussed as a function of increasing $\text{Nd}_4\text{Ba}_2\text{Cu}_2\text{O}_{10}$ content in the starting material. Effect of fast cooling through peritectic temperature (T_p) on the microstructural features is also discussed. Apart from the processing conditions and the features of conventional melt processed NdBCO samples, this chapter describes a new melt processing technique, called Infiltration and Growth (IG) process. In IG process the liquid phases are infiltrated into a shaped Nd-422 preform, and Nd-123 is grown while cooling below T_p at a very slow rate.

3.1 Introduction

Sintering is a commonly used ceramic processing technique for fabrication of bulk high temperature superconductors. It has been recognized that although good critical temperature (T_c) values can easily be achieved, critical current density (J_c) values are very

small in the bulk sintered material due to the weaklink nature of grain boundaries. Several parameters like homogeneity, density, oxygen content, cracks, and coupling at grain boundaries are considered to be very important in determining the J_c in bulk sintered YBCO. The liquid phase along the grain boundaries reduces the grain coupling and thus reduces J_c values. J_c is not an intrinsic property of a superconductor and is strongly dependent on the microstructure. Hence microstructural control is very important for obtaining high J_c .

The development of a new fabrication technique by Jin *et al.* [1] involving partial melting and slow cooling through the peritectic formation temperature of 123, called melt texture growth process, made it possible to improve the current carrying capacity of the YBCO superconductor. The slow cooling through T_p leads to alignment of superconducting grains normal to the c-axis. Melt processed stoichiometric Y-123 supports a current density of only a few hundred A/cm², but when an optimum quantity of fine sized Y_2BaCuO_6 (Y-211) is introduced as inclusions in the Y-123 matrix, the microstructural parameters are substantially modified and the J_c improves by a few orders of magnitude [2-4]. With optimal small sized Y-211 inclusions, the platelet widths and inter-platelet gaps are reduced substantially and fine secondary defects which are believed to aid the pinning of magnetic flux appear at the 211/123 interface [5-7]. The optimal 211 content in Y-Ba-Cu-O system is ~ 28 mol % and about 5 wt % Ag addition has also been reported to be beneficial [2]. The critical current density (J_c) values have been increased to a maximum of 10^4 - 10^5 A/cm² even in the presence of magnetic fields.

The $REBa_2Cu_3O_{7-\delta}$ (RE= Rare Earth element) superconductors with light rare earth atoms whose radii are comparable to that of Ba atoms form solid solutions of the type $RE_{1+x}Ba_{2-x}Cu_3O_{7-\delta}$ in ambient atmospheres whose T_c s are lower than those of the

stoichiometric compounds [8,9]. The extent of solid solution formation increases with the ionic radii of the rare earth atoms [10]. Yoo *et al.* [11] have demonstrated that melt processing of these compounds in low oxygen partial pressures can suppress the formation of the solid solutions to a large extent and enhances the T_c up to a maximum of 95 K. It has been observed that samples melt processed in low oxygen partial pressures show large increase in J_c at high fields. The peak in J_c has been attributed to pinning from the the solid solution regions turning normal at high fields [12-14]. It has also been proposed that the pinning is from the oxygen ordered **Ortho-II** low T_c phases [15]. To study the effect of Nd-422 inclusions on the microstructural and magnetic properties in Nd-123 system, **Nd-123** with various amounts of Nd-422 phase inclusions has been melt processed in the present work. Microstructural alterations by the change in Nd-422 content in the samples have been studied using a polarized light optical microscope and a scanning electron microscope. The results are discussed in comparison with those reported for other **RE-123** systems by other groups. The magnetic properties will be discussed in latter chapters.

3.2 Synthesis of Nd-123 and Nd-422 powder in large scale

3.2.1 $\text{NdBa}_2\text{Cu}_3\text{O}_7$ phase

In NdBCO system, $\text{Nd}_4\text{Ba}_2\text{Cu}_2\text{O}_{10}$ (Nd-422) insulating phase exists, but in other REBCO systems the corresponding phase is $\text{RE}_2\text{BaCuO}_5$ (**RE-211**). The following compositions have been chosen with increasing molar ratios of Nd-422 as given below :

- (i) $\text{NdBa}_2\text{Cu}_3\text{O}_7$(Nd-0)
- (ii) 90% $\text{NdBa}_2\text{Cu}_3\text{O}_7$ + 5 mol% $\text{Nd}_4\text{Ba}_2\text{Cu}_2\text{O}_{10}$(Nd-10)
- (iii) 80% $\text{NdBa}_2\text{Cu}_3\text{O}_7$ + 10 mol% $\text{Nd}_4\text{Ba}_2\text{Cu}_2\text{O}_{10}$(Nd-20)
- (iv) 70% $\text{NdBa}_2\text{Cu}_3\text{O}_7$ + 15 mol% $\text{Nd}_4\text{Ba}_2\text{Cu}_2\text{O}_{10}$(Nd-30)

(v) 60% $\text{NdBa}_2\text{Cu}_3\text{O}_7$ + 20 mol% $\text{Nd}_4\text{Ba}_2\text{Cu}_2\text{O}_{10}$(Nd-40)

The samples processed with the above compositions are referred to as Nd-0, Nd-10, Nd-20, Nd-30 and Nd-40 respectively, throughout the thesis for the sake of comparison with other REBCO systems. The starting materials taken were Nd_2O_3 , BaCO_3 and CuO with 99.9% purity. The materials were weighed out in the required stoichiometries and ball milled for 2 h with acetone as a medium. The total weight of the starting materials used in each case was 200 gms. The dried mixture was sintered at 980 °C for 12 h in air. Ball milling and sintering were repeated once more and the product ground to obtain the powders required for processing. The X-ray diffraction pattern obtained from sintered stoichiometric Nd-123 powder showed (Fig. 3.1) the tetragonal structure of Nd-123. No impurity phases could be detected in the XRD pattern showing that the material is in single phase form. XRD patterns of other Nd-422 rich sintered powders showed some extra peaks corresponding to the Nd-422 phase.

3.2.2 $\text{Nd}_4\text{Ba}_2\text{Cu}_2\text{O}_{10}$ phase

The Nd-422 powder was also prepared by the solid state reaction route. The starting materials were weighed out in the required stoichiometric proportions and ball milled for 2 h in acetone medium. The mixture was sintered at 1000 °C for 12 h in air. Ball milling and sintering were repeated once more and the product grounded to obtain the powders required for processing. The powder was brown in color whereas for other RE-211 phase it is green in color. X-ray diffraction pattern obtained from the sintered powder shows (Fig. 3.2) the tetragonal structure of Nd-422 with unit cell parameters $a = 6.714 \text{ \AA}$ and $c = 5.823 \text{ \AA}$. No impurity phase was seen in the XRD pattern.

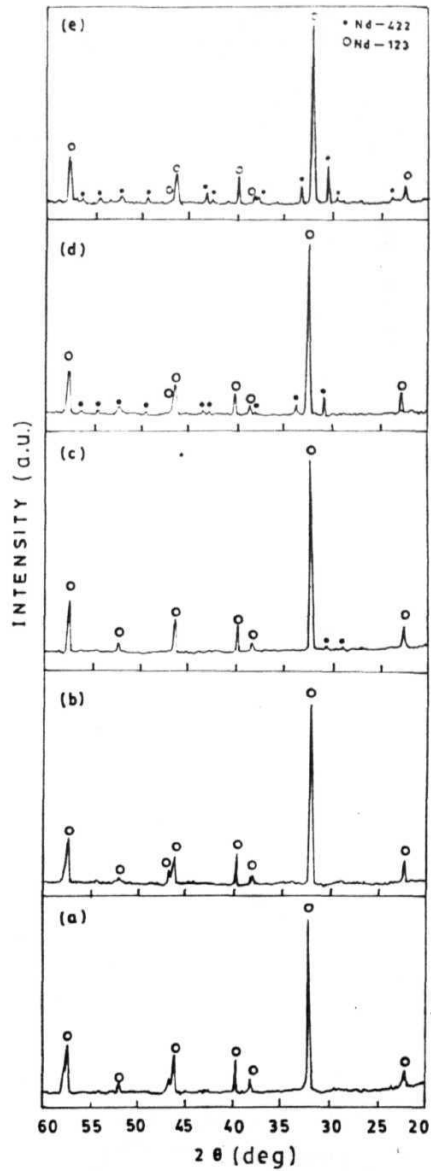


Fig. 3.1 XRD pattern of various powders (a) stoichiometric Nd-123 (b) Nd-123 with 5 mol % (c) 10 mol % (d) 15 mol % and (e) 20 mol % $\text{Nd}_4\text{Ba}_2\text{Cu}_2\text{O}_{10}$ phase.

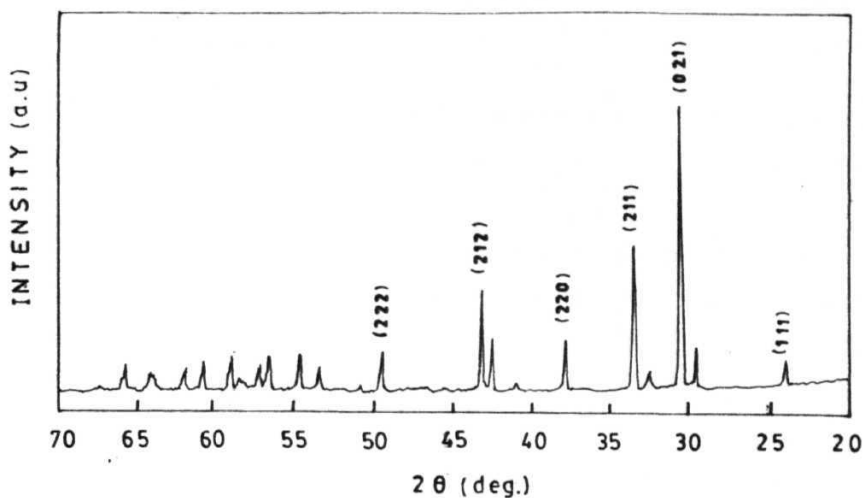


Fig. 3.2 XRD pattern of $\text{Nd}_4\text{Ba}_2\text{Cu}_2\text{O}_{10}$ phase.

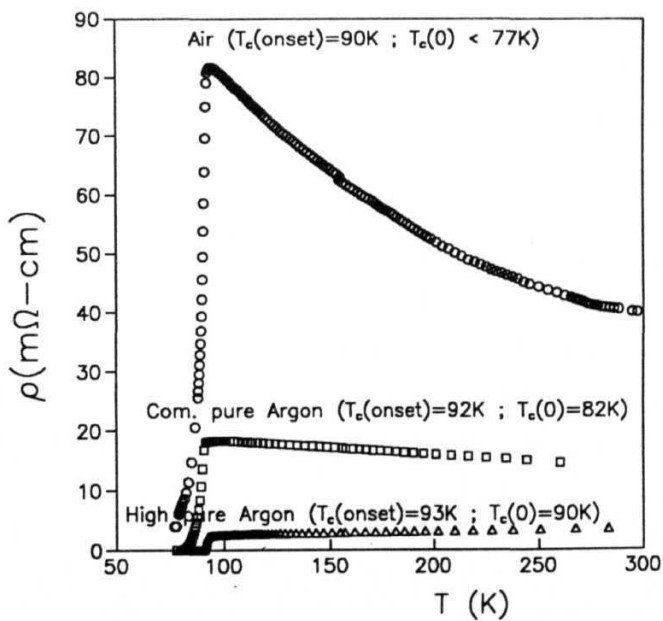


Fig. 3.3 Temperature variation of resistivity for sintered NdBCuO superconductor processed in various atmospheres.

3.3 Sintered NdBCO

The presintered powder (prepared as described in the section 3.2.1) of stoichiometric Nd-123 was pelletized and kept at 980 °C for 12 h. To evolve a method of making samples with a minimum solid solution phase $\text{Nd}_{1+x}\text{Ba}_{2-x}\text{Cu}_3\text{O}_{7-\delta}$, it was processed in different atmospheres like air, commercial Argon and high purity Argon. The oxygen loading schedule will be described in the section 3.4.2. The dc electrical resistivity measurements showed a T_c onset at 90 K and a zero resistance less than 77 K for the samples processed in air, which is shown in Fig. 3.3. Under commercial purity Argon, the T_c onset was at 92 K and zero resistance occurred at 82 K. Under high pure Argon gas (with 4 ppm of O_2), the zero resistance was at 90 K with an onset at 93 K. This shows that T_c s of the samples are highly sensitive to the processing atmosphere.

Figure 3.4 shows the XRD pattern of a sintered Nd-123 sample. It has been indexed to the reported [16] orthorhombic unit cell with parameters $a = 3.862 \text{ \AA}$, $b = 3.918 \text{ \AA}$ and $c = 11.771 \text{ \AA}$. The optical microstructure of the sintered Nd-123 is shown in Fig. 3.5 under polarized light. Large number of interconnected grains with an average grain size $\sim 15 \mu\text{m}$ can be seen in the figure. The grains are randomly oriented crystallographically. Variation in color intensity under polarized light represents randomly oriented grains. Dimos *et al.* [17] have shown that J_c decreases with increasing misorientation angle between two grains using various bicrystalline thin films. It is difficult to achieve high J_c values in randomly oriented samples since the control of the grain boundary structure cannot be performed in the normal sintering method. The weaklink nature of the polycrystalline NdBCO sample is studied using ac susceptibility and magnetic flux profile measurements and the results are described in the Chapters 4 and 5.

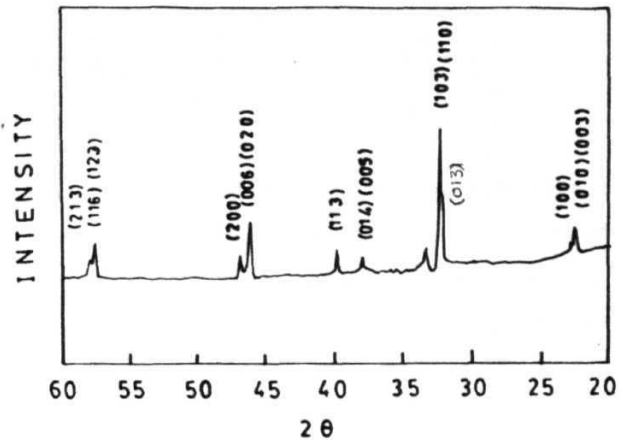


Fig. 3.4 XRD pattern of sintered $\text{NdBa}_2\text{Cu}_3\text{O}_{7-\delta}$, processed in high purity Argon atmosphere.

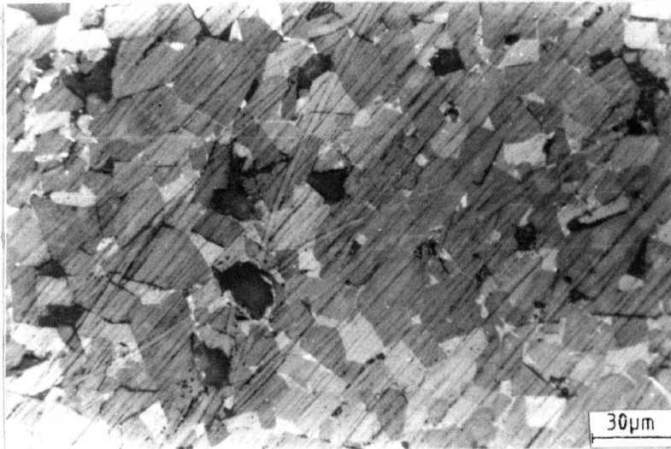


Fig. 3.5 Optical micro graph under polarized light of polycrystalline Nd-123 superconductor. Randomly oriented small sized ($\sim 15 \mu\text{m}$) grains can be seen.

3.4 Melt Processing

3.4.1 Furnace configuration

A simple, home-built tubular furnace was used for melt growth processing. It has a recrystallised Alumina tubular muffle of 5 cm inner diameter and 100 cm in length. The heating elements are wound uniformly so as to produce a hot zone length of 10 cm at the center of the furnace. The uniformity of the hot zone was such that there was no measurable temperature gradient in the volume occupied by the samples (~ 15 mm length). The temperature inside the muffle was controlled to $\pm 1^\circ\text{C}$ with a programmable PID controller (WEST 2054). Proper care was taken in sealing the furnace from air leak, especially when high pure Ar gas was flowing through the muffle.

Presintered powders having the compositions mentioned in section 3.2 were pelletized by uniaxial press in a square die of 15 mm side under a pressure of 8 tonnes. Nd-422 preform was used as substrate material to prevent liquid phase outflow. The pellets were melt processed in the tubular furnace. They were kept at 980°C for 2 h, rapidly heated to 1115°C (where 123 melts incongruently into $\text{Nd}_4\text{Ba}_2\text{Cu}_2\text{O}_{10}$ + Liquid), held for 10 minutes; cooled rapidly to 1045°C (just above peritectic temperature) and slowly cooled at a rate of 1°C/h to 980°C for the growth of 123 to occur. The above processing was done on two sets of samples : one set in Ar gas of commercial (8 ppm of oxygen) and another in high purity (4 ppm of oxygen) Ar. The heat treatment profile is given in Fig. 3.6(a). The samples were oxygen loaded by the following schedule in flowing oxygen : 1h at 600°C , cooled to 500°C in 2 h, cooled to 400°C in 12 h, cooled to 250°C in 150 h. The oxygenation schedule is given in the Fig. 3.6(b).

3.4.2 The melt processing experiments

An outline of the melt processing experiments have been given in section 3.4.1. The temperature schedule used for processing of various compositions is shown in Fig. 3.6(a). In this section, various specific problems encountered during the experiments aimed at melt processing Nd-123 with different amounts of Nd-422 are discussed along with the solutions developed.

It was observed that when the amount of Nd-422 content was reduced in the presintered composition, the porosity increased in the melt textured samples. It was not possible to process pure melt textured Nd-123 sample using the schedule given in Fig. 3.6(a), since the liquid phase flow from the Nd-422 preform was severe. This flow of liquid was suppressed by slow cooling from 1080 °C instead of 1045 °C, which is nearly sintering temperature of the Nd-422. A possible reason for this suppression of the liquid phase out flow, is a further compaction of the Nd-422 preform due to a change in the morphology of the Nd-422 phase at those temperatures.

Processing atmospheres

Since the ionic radius of the Nd atom is comparable in size with Ba atom [18], solid solution of the type $\text{Nd}_{1+x}\text{Ba}_{2-x}\text{Cu}_3\text{O}_{7-\delta}$ forms when it is processed in air. The extent of solid solution is $0 < x < 0.6$ [8]. Yoo *et al.* [11] processed Nd-123 samples under lower oxygen partial pressures and successfully suppressed the solid solution formation to a large extent. In the present case, the samples were processed under flowing Ar gas. Gas of two grades of purity were used in the present experiments (i) of commercial purity and (ii) of high purity (with 4 ppm of O_2). The samples processed in commercial purity Argon after the low temperature oxygen anneal, had the onset at T_c 90 K but with a very broad transition width as shown in Fig. 3.7. Zero resistance was observed at around 80

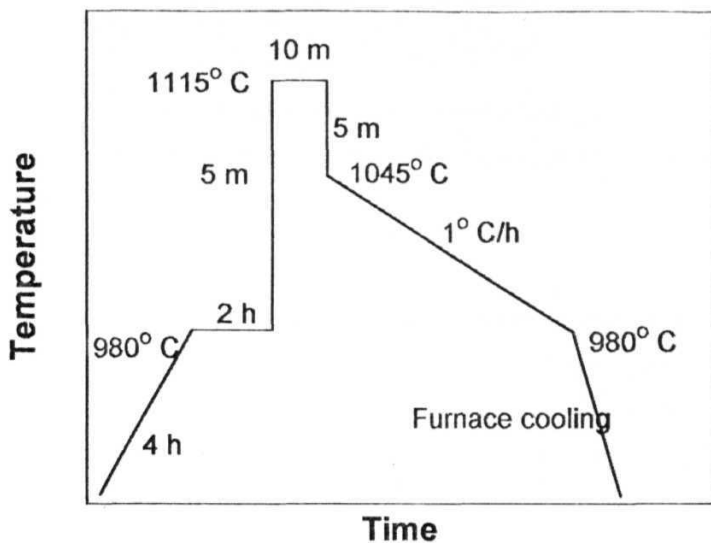


Fig. 3.6(a) Heat treatment profile for melt processing of NdBCO samples.

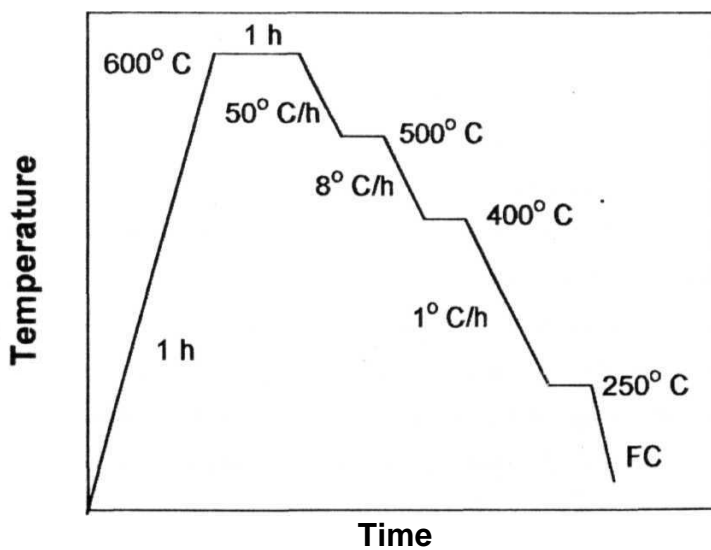


Fig. 3.6(b) Heat treatment schedule for oxygenation.

K - 87 K for all the samples. The samples processed in high purity Argon, after proper oxygen loading, had T_c onset around 93 K with transition widths less than 1.2 K as shown in Fig. 3.8.

Oxygen loading

All the samples after they were processed in Ar atmosphere were non-superconducting with a tetragonal structure. In general the tetragonal to orthogonal phase transformation takes place at 600 °C to 450 °C in oxygen atmosphere for Y-123 system [2]. Since the melt textured samples are highly dense it is difficult to fully oxygenate them and they have to be annealed for prolonged durations for complete oxygenation. Murakami *et al.* [2] followed a slow cooling schedule from 600 to 400 °C in oxygen for Y-123 samples. Initially, the same schedule was adopted for the melt textured Nd-123 superconductor and it was found that the samples had a T_c around 85 K. Suspecting insufficient oxygen intake by the samples, they were annealed using the same schedule several times. Even then there was no improvement in T_c . The samples were then annealed at various higher temperatures for longer time. T_c was found to decrease as the annealing temperature was increased. By annealing at different temperatures, it was found that transformation of tetragonal to orthorhombic phase takes place only at lower temperatures. Because of this observation, Murakami's oxygenation schedule was extended to lower temperatures. Since lower temperatures are involved in the oxygenation, longer durations of oxygenation are needed. Figure 3.9 shows the optical micrograph of a partially oxygenated sample under polarized light. Since the fully oxygenated region has good reflectivity, it can be easily distinguished between the transformed (Ortho) and untransformed (tetra) regions. The transformed region is along the cracks in the sample. The presence of the cracks thus, helps in faster oxygenation in melt processed samples.

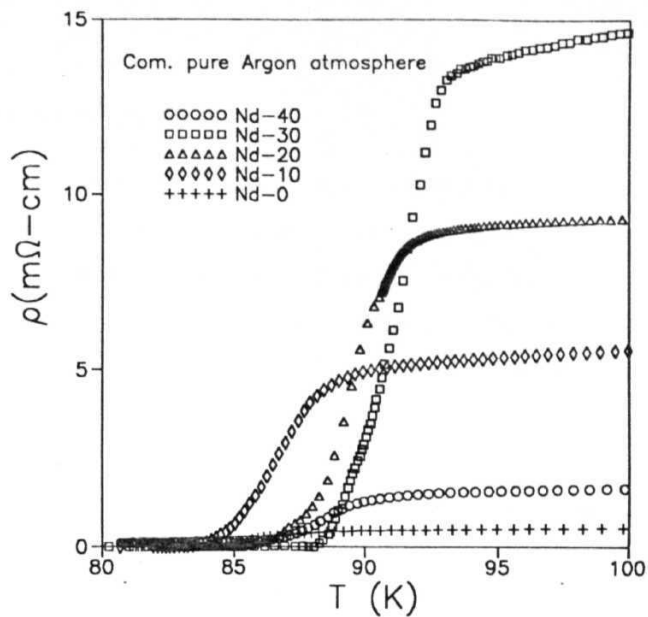


Fig. 3.7 Resistivity versus temperature for various melt textured NdBCO superconductors processed in commercial purity Argon atmosphere.

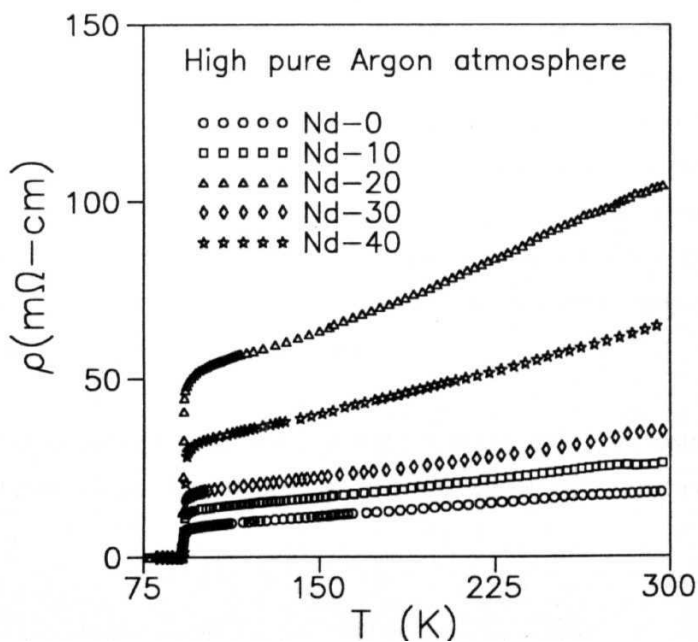


Fig. 3.8 Resistivity versus temperature for various melt textured NdBCO superconductors

3.5 Microstructural investigations

Figures 3.10(a) - (d) show the optical microstructures under polarized light for melt textured Nd-0, Nd-20, Nd-30 and Nd-40 samples with at least one domain boundary included in the field of view. All the samples had 6-8 mm² domains oriented in different directions with respect to the sample surface, as observed by their different shades under polarized light. The Nd-422 particles appear in different colour contrast compared to the Nd-123 matrix.

In Fig. 3.11, the average diameter of the pores observed in the microstructure is plotted as a function of the Nd-422 content. A large variation in going from 0 mol % Nd-422 to the one with 10 mol % is seen in comparison with in going from 10 mol % to 20 mol % Nd-422. The reason for the origin of such pores have been discussed in the literature. They have been attributed to the evolution of oxygen gas during the melting of 123 phase [19]. The observed pore size variation with Nd-422 concentration cannot be explained by the gas evolution mechanism. An alternative mechanism has also been proposed elsewhere [20]. The mechanism proposes that, the pore size variation with Nd-422 concentration, is due to the packing of Nd-422 particles at the molten stage. In the molten stage, stoichiometric Nd-123 contains poorly packed large acicular Nd-422 particles. Due to these largely spaced Nd-422 particles, the pores are caused by the liquid phases moving to such particles to react during texturing stage. In the Nd-422 rich samples, due to closely packed Nd-422 particles, the liquid phase moves little distance to react during texturing and causes small sized pores.

The domain boundaries in these samples cooled at 1 °C/h through T_p , are clean and there is no liquid phase left out after the **peritectic** reaction. Some domain boundaries in

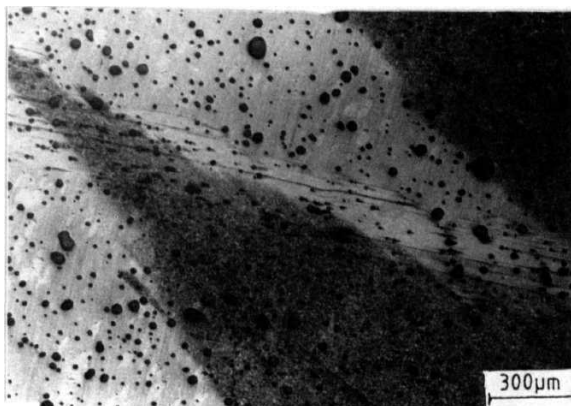


Fig. 3.9 Optical micrograph of a **partially oxygenated** melt textured sample. Both tetragonal and orthorhombic **Nd-123** phases can be seen.

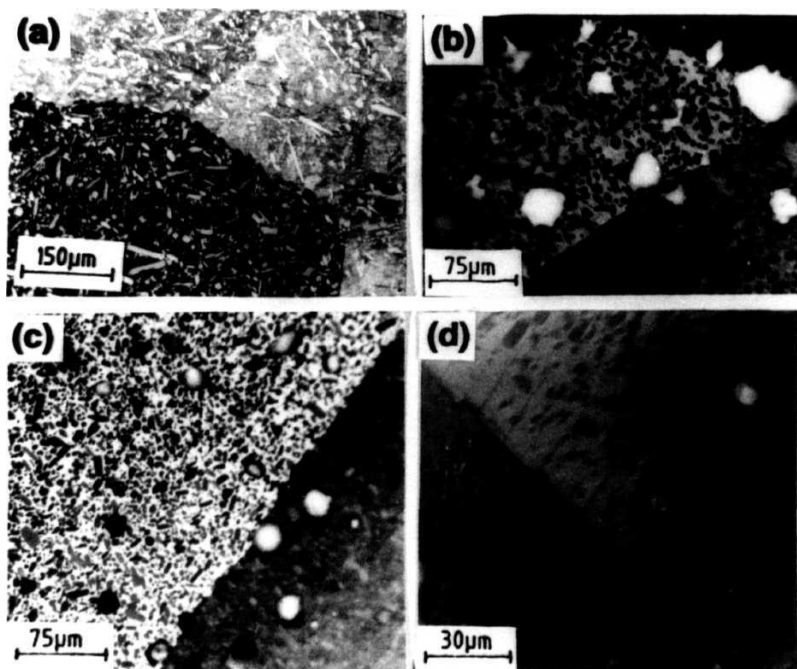


fig. 3.10 Optical micrographs under polarized light, showing domain boundaries of melt textured (a) Nd-0, (b) Nd-20, (c) Nd-30 and (d) Nd-40 samples. Clean domain boundaries can be seen without any liquid phase. An unusual. Nd-422 free region can be seen at the domain boundary in Nd-40 sample.

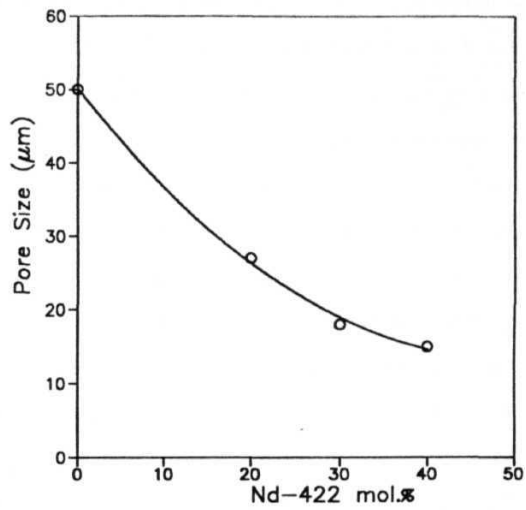


Fig. 3.11 The observed average pore size with Nd-422 content in various melt textured samples. Solid line is guide to the eye.

the Nd-40 sample were found to be free of Nd-422 precipitates. The domain boundaries with wide 422 - free regions are shown in Fig. 3.10(d), which have not been observed in any RE-123 systems. These unusual domain boundaries may not affect the transport critical current very much, because most of the domain boundaries were of the usual type seen in low Nd-422 concentration samples. However, the unusual domain boundaries are interesting from a view point of nucleation and origin of platelets. It can be noted that the inter-platelet gaps appear in the 422 - free region at the boundary and different platelets protrude by different extent into the next domain. This observation evidences the view that different platelets nucleate separately and grow [21,22], rather than form by the cracking up of a single domain due to various stresses after solidification as is generally believed in the literature [23]. The 422 - free domain boundaries may be hypothesized to occur as follows : When two domains (collection of parallel plates) impinge during melt growth, the liquid phases residual from the incomplete peritectic reaction collect at the boundary. They completely convert the locally present Nd-422 into Nd-123 phase.

Figure 3.12 shows the **microstructure** of Nd-0, **Nd-10**, Nd-20, Nd-30 and Nd-40 samples under higher magnification, obtained using a scanning electron microscope (SEM). The domains are seen to be sub-divided into parallel platelets. All the 123 platelets within a single domain have a common orientation. The platelets are separated from one another by small gaps. These gaps are not continuous across the width of the domains unlike in the Y-123 system. The length of the interplatelet gaps decreases with increase in Nd-422 concentration. This observation could be relevant from the point of view of increasing the critical current density of the samples, because the inter-platelet gaps are weaklinks and get progressively reduced with increasing Nd-422 content. Since it is now more or less established that the gaps between platelets occur at the solidification stage,

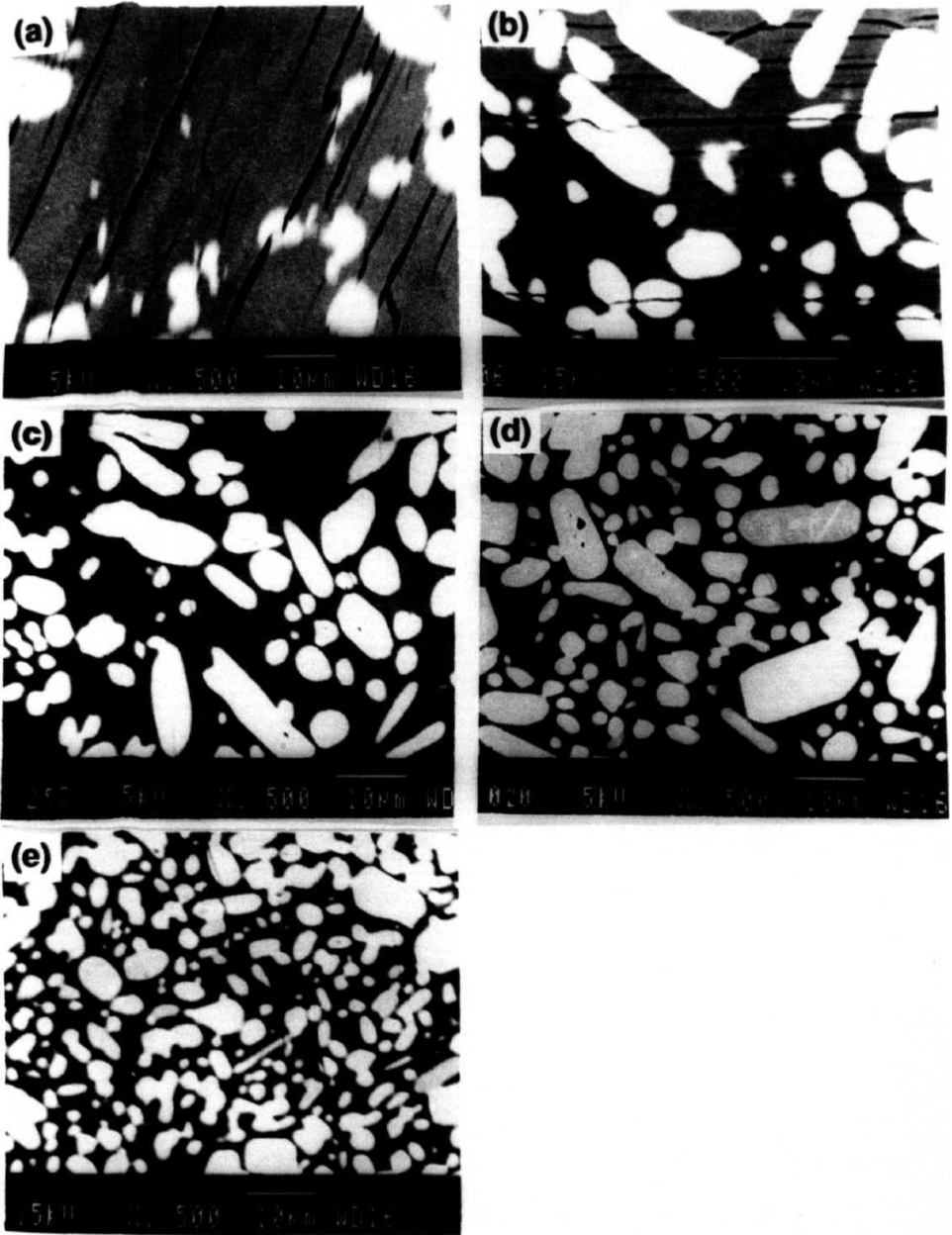


Fig. 3.12 SEM micrographs of (a) Nd-0, (b) Nd-10, (c) Nd-20, (d) Nd-30 and (e) Nd-40 melt textured samples.

a mechanism of separate nucleation of platelets rather than their formation by the cracking up of a single domain has to be considered to explain the above observation. The gaps can then be hypothesized to be a result of the very low solubility of the Y-ions in the liquid. It can be proposed that the relatively high solubility of Nd-ions in liquid and the corresponding wider reaction zones around Nd-422 particles would account for the observation of discontinuous inter-plate gaps in the Nd-123 system. Separately nucleated and growing parallel platelets would merge into one another when the reaction zones surrounding the dissolving Nd-422 particles are wider. This is unlike in the Y-123 system, where the slope of the liquidus in the pseudo-boundary phase does not change at T_p [24], and the Y-ions are hardly soluble in the liquid below T_p [25], and hence the reaction zones surrounding the dissolving Y-211 particles are only a few micrometers in width [26]. On the contrary, the slope of liquidus changes considerably at T_p for the Nd-123 system [27] and Nd-123 is known to crystallize rapidly the liquid and a larger reaction zone rich in Nd-ions in the liquid surrounding the dissolving particles [28].

From Fig. 3.12, it can be seen that the Nd-422 particles are uniformly distributed in the Nd-123 matrix for all the samples. There are two kinds of Nd-422 particles, one spherical in shape, and the other one acicular in shape. Acicular particles are observed to be randomly oriented in the Nd-123 matrix.

The average width of the platelets and that of the gaps between the platelets, decrease with increasing Nd-422 content as shown in Fig. 3.13. It is seen that the variation of gap width versus platelet width is nearly linear (Fig. (3.14)). It is interesting to note that the variation of gap width versus the inter-platelet width is the same in the Nd-123 system as observed for the Y-123 system. The slope of the linear line in Y-123 system is 3.6, whereas in Nd-123 system it is found to be ~ 15 . A model by Schmitz *et al.* [21]

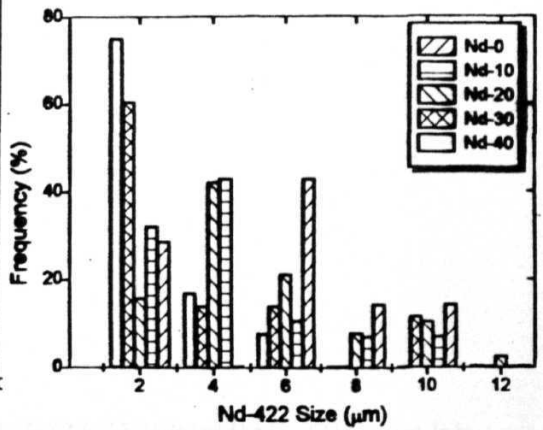
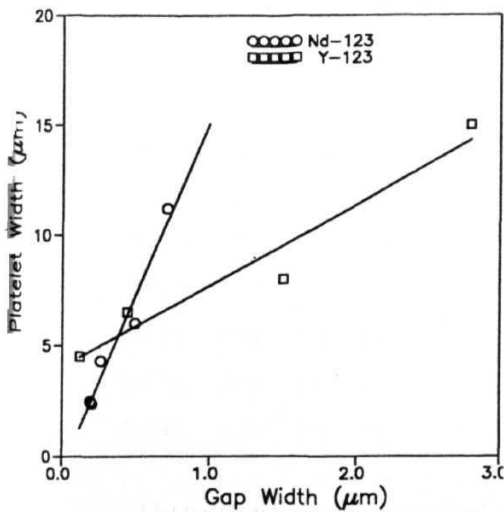
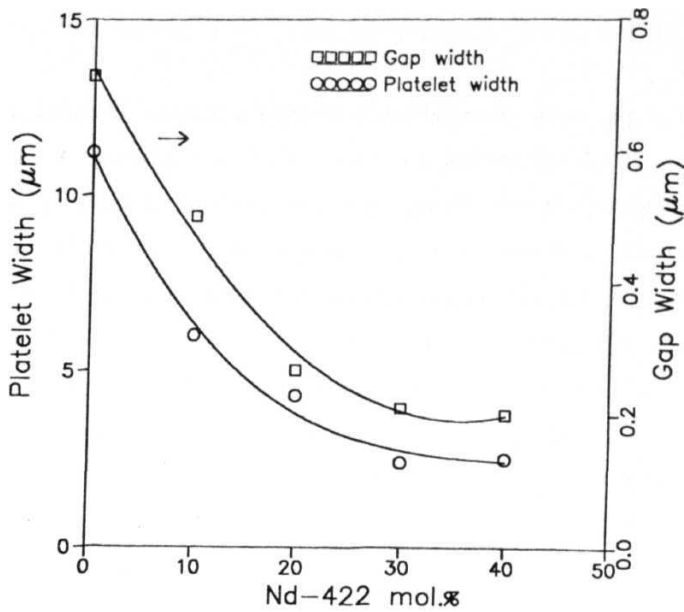


fig. 3.14 Platelet width versus gap width obtained from microstructures of various melt textured NdBCO and YBCO samples. A linear relationship between platelet and crack widths can be seen.

Fig. 3.15 Size distribution of Nd-422 phase particles in melt textured NdBCO samples.

discussed in detail the interaction between platelets rapidly advancing in the in-plane directions and 211 particles in the melt. This model predicts platelet like growth of the 123 phase being caused by the strong anisotropic growth velocities [30] (growth velocity in ab plane direction is greater than the growth velocity in c-direction). The anisotropy of growth velocities leads to a preferred growth of the ab planes parallel to the temperature gradient. The low growth velocity parallel to the c-direction results in planar defects (interplatelet gaps) between the ab planes. Microstructural parameters such as platelet width P_w , crack width C_w and the average size of 422/211 particle d , are compared in the Table 3.1 for the Nd-123 and Y-123 systems. It can be seen from the Table 3.1 that, the gap widths are much smaller in Nd-123, in comparison to Y-123 system.

Table 3.1 Microstructural Parameters in Y-123 [6] and Nd-123 system.

	μm	μm	μm
Y-0	2.8	15	
Y-20	1.5	8	8-10
Y-30	0.45	6.5	4-6
Y-50	0.125	4.5	1-3
Nd-0	0.70	10	6.0
Nd-10	0.43	5.0	4.2
Nd-20	0.30	4.0	3.0
Nd-30	0.21	2.4	2.5
Nd-40	0.20	2.3	2.0

The particle size of Nd-422 inclusions becomes smaller as the Nd-422 content is increased. The particle size distribution of Nd-422 is shown in Fig. 3.15 for all the samples.

More number of particles per unit area become circular with increase in Nd-422 content. There are 60% - 70% spherical Nd-422 particles with an average diameter of 2 μm or less, in the Nd-30 and Nd-40 samples, whereas only 20% - 30% particles are spherical in Nd-0, Nd-10 and Nd-20 samples. This variation can be correlated to the progressive change in size and morphology of the Nd-422 particles in the liquid above T_p . Figure 3.16 shows the SEM micrographs of Nd-0, Nd-10, Nd-20, Nd-30 and Nd-40 samples quenched after holding at 1115 °C for 15 minutes to decompose Nd-123 into Nd-422 and liquid phases. The progressive decrease in size of the Nd-422 particles (Fig. 3.17) in liquid with increase in Nd-422 content is due to the excess Nd-422 in the initial composition, forms nuclei for the crystallization of Nd-422 formed by the decomposition of Nd-123 at high temperatures. When such a large number of nuclei are present, the Nd-422 formed by the decomposition of 123 would be distributed over the larger number of nuclei and all of them would grow only to a smaller extent. When the number of Nd-422 particles growing in the liquid are large, they would not grow freely into the acicular shape promoted by their crystal structure, but rather into small spheres in spatially restricted growth. In the case of melt processed Y-123 samples, smaller spherical Y-211 inclusions are known to favor the formation of secondary defects in the 123 matrix at the 123/211 interface. In the literature, it is reported that Y-211 particles with a large surface curvature are associated with numerous dislocations and they aid flux pinning [6,7]. Samples containing 30 and 40 mol% Nd-422 have spherical inclusions with average size < 2 μm which are favorable for flux pinning.

The aspect ratio, here defined for an acicular particle as the ratio between major and minor axis is analyzed for the Nd-422 particle. In the **pro-peritectic** stage as it can be seen in Fig. 3.16(a), the aspect ratio of Nd-422 particles in the liquid is around 8, whereas after solidification (Fig. 3.12(a)) by slow cooling, the aspect ratio of trapped

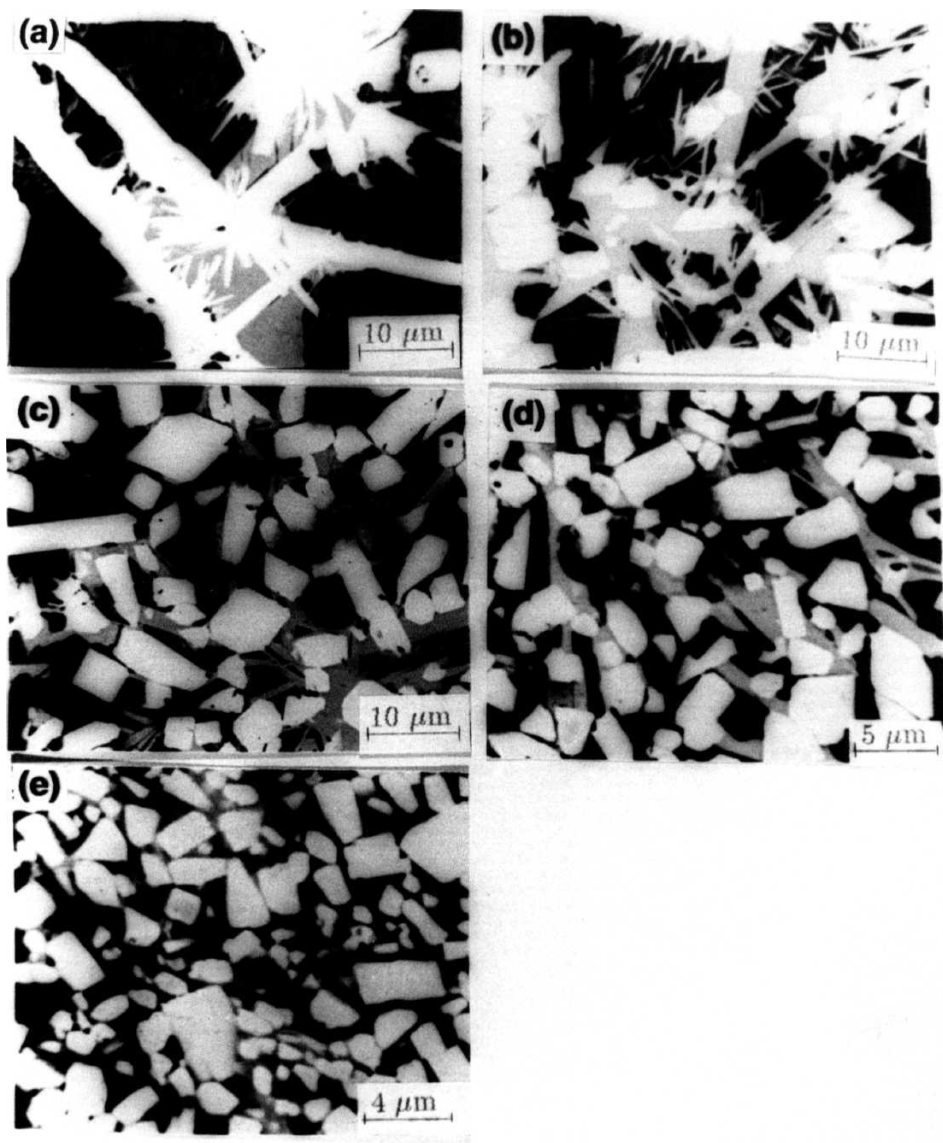


Fig. 3.16 Quenched (from 1115°C after holding for 15 minutes) microstructures of (a) Nd-0, (b) Nd-10, (c) Nd-20, (d) Nd-30 and (e) Nd-40 samples. Different sizes and morphologies of Nd-422 particles in the Ba-Cu-0 melt can be seen.

Nd-422 particles is only around 3. The reduction in aspect ratio is a result of the faster dissolution of Nd-422 particles in the liquid at points where the curvature of its interface with the liquid is sharper.

It may be noted that not only the size of the residual Nd-422 inclusions in the melt processed material vary with Nd-422 concentration as does the size of the Nd-422 particles in the liquid at the melting stage, but also the platelet widths, gap widths and even the pore size. This observation suggests that the nucleation of platelets is strongly correlated to the number of Nd-422 particles available in the liquid, and the width of the gaps between the platelets is probably connected to the inter-particle spacing at the melting stage. The observations in the Nd-123 system are mostly similar to those in the Y-123 system pointing to a similar mechanism being operative in controlling the microstructure. The differences like the discontinuous gaps between platelets in the Nd-123 system and the continuous ones in the Y-123 system are a result of the faster crystallization rate of Nd-123.

3.6 Effect of cooling rate on microstructural features

It is well known that very slow rate of cooling (1°C/h) is needed to develop highly textured superconducting matrix in $\text{YBa}_2\text{Cu}_3\text{O}_{7-\delta}$ (Y-123) because of low Yttrium solubility limit in the Ba-Cu-O melt [25]. Thus, it takes a longer time to melt process Y-123 superconductor, which is a drawback and restricts the practical application. High oxygen partial pressure increased the growth rate 2.5 times higher than that of the crystal grown under air [31,32]. This high growth rate was mainly attributed to the increased Y-solubility in high oxygen partial pressure. It is found that certain RE-123 type compounds containing the rare earth (RE) element Nd or Sm possess a high solubility in the Ba-Cu-O melt [25,33]. When they are processed in air a solid solution phase of the form

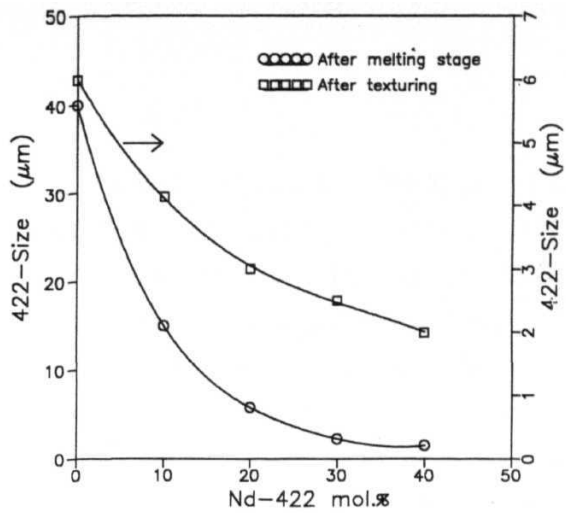


Fig. 3.17 Average Nd-422 particle size after melting stage and after texturing.

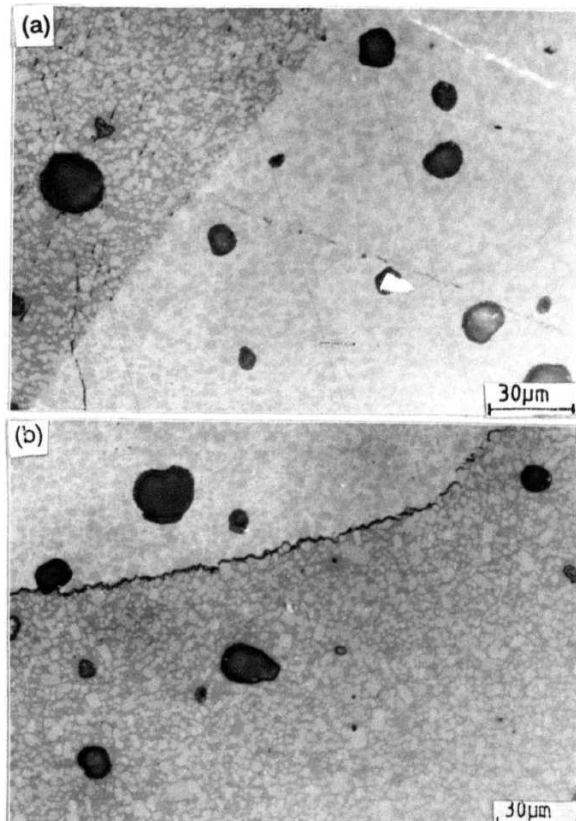


Fig. 3.18 Microstructures of fast cooled (40 °C/h) sample showing (a) a clean domain boundary and (b) domain boundary with liquid phase.

$\text{RE}_{1+x}\text{Ba}_{2-x}\text{Cu}_3\text{O}_{7-\delta}$ is formed locally, which is a low T_c phase [34]. Salama *et al.* [35] directionally solidified Nd-123 and could obtain a well textured Nd-123 even with fast pulling rates (50 mm/h). We have examined the texturing of Nd-123 superconductor with various rates of cooling through the peritectic temperature in the melt textured growth process. The results of microstructural investigations of melt textured samples cooled at various rates through T_p are presented here.

Pellets with the composition $\text{NdBa}_2\text{Cu}_3\text{O}_{7-\delta} + 20 \text{ mol\% Nd}_4\text{Ba}_2\text{Cu}_2\text{O}_{10}$ (Nd-40) are melt processed using the heat treatment schedule (Fig. 3.6(a)), with 1, 4, 10, 20, 40 °C/h rates of cooling through peritectic temperature. The process was carried out in Ar atmosphere to suppress the solid solution phase formation. After texturing, these samples were oxygenated using the schedule given in Fig. 5.6(b) to obtain superconducting phase.

All the samples processed with the rates of cooling 1, 4, 10, 20 and 40 °C/h have well textured domains and showed good levitation and suspension properties. The optical microscope with polarized light revealed that the samples cooled at 1, 4 and 10 °C/h rates contained a well textured domains of average size 7-8 mm, and clean domain boundaries without any liquid phase. But the samples cooled at 20 and 40 °C/h contained many boundaries with an average domain size of 3-4 mm. Most of the domain boundaries for the sample with 40 °C/h rate of cooling were clean, i.e, only few of them have unreacted liquid phase at the domain boundaries. Optical micrographs of domain boundaries without and with unreacted liquid phase are shown in Fig. 3.18. When the growth directions of the two growing domains are normal or nearly normal to the boundary plane between them, impurities and excess solute rejected into the liquid ahead of the growth front can be trapped at the domain boundary. In the case of Y-123 system, the samples cooled at 4 °C/h rate showed the residual liquid phase along the most of the

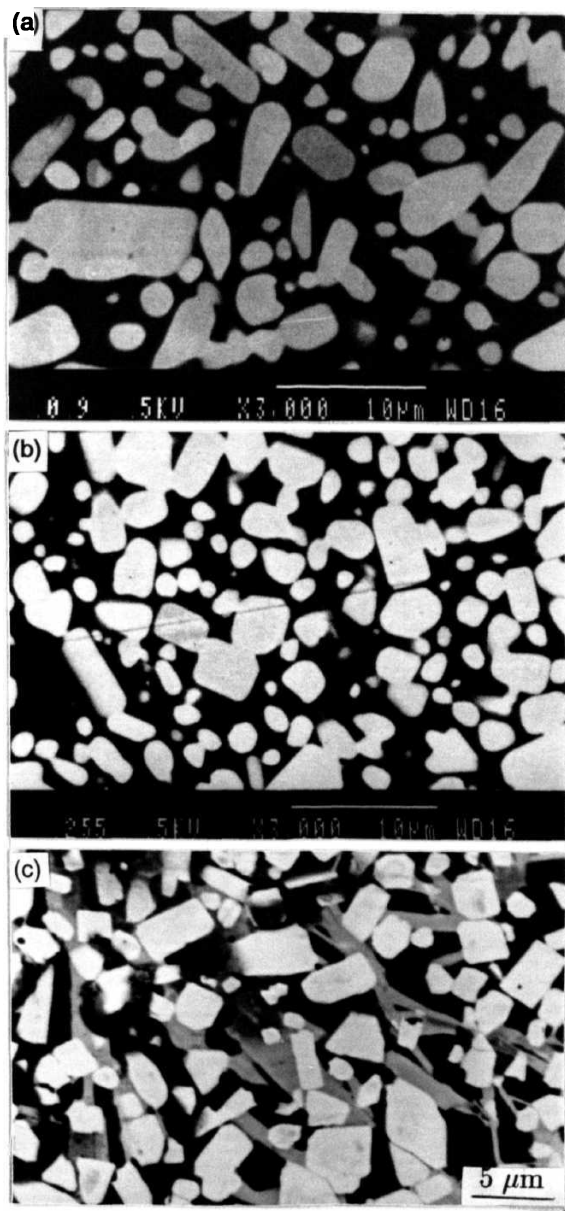


Fig. 3.19 SEM micrograph of (a) 1 °C/h, (b) 40 °C/h cooled sample, and (c) Quenched microstructure at pro-peritectic stage of Nd-40 sample.

domain boundaries [22]. Contaminated domain boundaries suppress the transport bulk critical current density, indicating that the **Y-123** system has to be **melt** processed with slow rate of cooling for good **microstructural** and magnetic properties. But the Nd-123 melt processed samples cooled at 1,4, 10, 20 °C/h rates showed clean domain boundaries without any unreacted liquid phases. Presence of few contaminated domain boundaries in 40 °C/h sample represents the marginal cooling rate in Nd-123 system to obtain good quality of melt textured samples.

The microstructure within the domains shows that the average size of the Nd-422 particles decreases with increasing cooling rates, which is similar to the observation reported by **Salama et al.** [35] in directionally solidified samples. Slow cooled samples contained considerable amount of large size acicular Nd-422 particles with average diameter of 4-5 μm and a length of 15 μm as shown in Fig. 3.19(a). But in the fast cooled samples, the length of the acicular particles is reduced to 5 μm (Fig. 3.19(b)) and also the number of large sized acicular particles is less in comparison with the slow cooled samples. Origin of the small sized Nd-422 particles in fast cooled samples can be understood from the microstructure of the sample at pro-peritectic stage i.e, just after decomposition of Nd-123 phase into Nd-422 and liquid phase. It can be seen from the Fig. 3.16(c) that the average size of the pro-peritectic Nd-422 particles are $< 1 \mu\text{m}$. Due to higher processing temperatures involved for Nd-123 system, the size of the pro-peritectic Nd-422 in the liquid increases rapidly with residence time above peritectic temperature, T_p . Therefore, it is difficult to obtain fine Nd-422 particles in the melt processed microstructure with slow rate of cooling. But in the fast cooled samples, the growth of Nd-422 phase in the liquid is suppressed due to low residence time near T_p . The uniformly distributed fine spherical insulating particles are necessary in enhancing the flux pinning [2-7].

The micro gaps with average size of $0.2\ \mu\text{m}$ observed in the samples are not continuous. There is no effect of cooling rates on the gap and platelet widths. Even in the $40\ ^\circ\text{C/h}$ cooling rate, the microstructure consists of long well grown platelets. Presence of well aligned platelets in Nd-123 sample, processed at $40\ ^\circ\text{C/h}$ rate, suggests that the growth rate of Nd-123 is one order of magnitude higher than the Y-123 system. In the case of YBCO system, the platelets are bent at $15\ ^\circ\text{C/h}$ rate of cooling [22]. In the fast cooled ($40\ ^\circ\text{C/h}$) Nd-123 sample, the domain boundaries had some residual liquid phases. This is because of the fast cooling rates, the advancement of growth front will be slower than the cooling rate which hinders planar growth and leads to liquid phase residual along the domain boundaries.

3.7 Infiltration and Growth process

Shape forming simultaneous with critical current enhancement is a must for realizing applications. Conventionally melt processed samples shrink by 25 % and have large hollow regions within their interiors due to liquid phase outflow. This section describes the use of a process termed as "Infiltration and Growth (IG) process" to eliminate most of the difficulties associated with the melt growth process as applied to the Nd-123 superconductor. This process can enable the fabrication of large complex shapes without distortion, with good dimensional tolerances and high critical current density for applications.

In the melt growth process, an intimate mixture of the pro-peritectic $\text{RE}_2\text{BaCuO}_5$ (RE-211) phase (or $\text{RE}_4\text{Ba}_2\text{Cu}_2\text{O}_{10}$ (RE-422) phase, in the case of the Nd system) and liquids ($\text{Ba}_2\text{Cu}_3\text{O}_7/\text{BaCuO}_2$ and CuO) are cooled very slowly through the peritectic formation temperature, T_p . In the reported variations of the melt growth process, a mixture of RE-211 and liquids are obtained by an incongruent melting of RE-123 at high temperatures [1,36,37], or by mixing the constituent powders at room temperature [38,39].

Large amounts of liquid phase losses occur in the samples during processing. This leads to a substantial shrinkage during processing with accompanying distortions and cracking, and to millimeter-sized internal defects within the products due to liquid phase outflow. Such problems severely limit the shaping of the products into useful geometries.

It is reported that the Nd-422 grains coarsen in the liquid during melt processing, at temperatures above T_p [29]. Pro-peritectic grain coarsening is more pronounced in the case of **RE-123** samples with higher T_p because of the higher processing temperatures involved. The peritectic formation temperature, T_p , as well as the existence range of the solid solutions, increase in direct proportion to the ionic radii of the RE ions [40]. Hence, in **Nd-123** system, the size of the pro-peritectic Nd-422 in the liquid increases rapidly with residence time above T_p , and it is difficult to obtain fine Nd-422 precipitates in the melt processed microstructure. It is shown that the Nd-422 phase particles are refined with faster rate of cooling through T_p (section 3.6) and could be correlated well to the size of Nd-422 particles in the molten stage. Recent literature [41] discusses the addition of CeO_2 to refine the Nd-422 size in melt processed Nd-123.

In this section, microstructure of Nd-123 obtained by an infiltration of liquid phases into Nd-422 preforms and subsequent texturing is discussed [42]. The fabrication of 3-D components of **Y-123** superconductors with high J_c using this process, which is referred to as the Infiltration and Growth (**IG**) process, has been reported recently [43]. The process is similar to the ones used for the fabrication of metal/ceramic matrix composites by infiltration of liquids into pre-shaped preforms and the formation of product phases by a reaction with the preform [44]. It is well known that such processes enable the fabrication of large near-net shaped components due to avoidance of shrinkage during heat treatment. It may be noted that conventional melt processing has mostly yielded only disk shaped

specimens or bars.

Experimental

The Infiltration and Growth (IG) process, in its simplest form, uses porous Nd-422 disks as preforms and Nd-Ba-Cu compounds with suitable Nd:Ba:Cu ratios as the source of liquid phases. The quantity of the liquid phases available from the sources was varied by choosing a few compositions shifted from Nd-123 to the Nd-422 rich region of the Nd-Ba-Cu-0 phase diagram [8]. A double layered pellet of Nd-422 and Nd-123 were pressed uniaxially in a square steel die of side 15 mm, at a pressure of 8 tonnes, with the Nd-422 at the bottom. Four more pellets were pressed using Nd-123 containing 10%, 20%, 30% and 40% Nd-422 at the top. The processing was done in a tube furnace which was first heated up to 1115 °C for 15 minutes to melt the liquid phase sources and to allow the liquid phases to infiltrate completely into the preforms. Whether the infiltration was complete and uniform was inferred from microstructural studies of samples quenched after the 15 minutes hold. The samples were then cooled to 1040 °C, and from there to 980 °C at 1 °C/h. After a dwell for 2 h at 980 °C, the sample was furnace cooled to room temperature. The above processing was done in Ar gas of commercial purity (8 ppm of oxygen) as well as high purity (4 ppm of oxygen). The samples were oxygen loaded by the thermal treatment schedule is discussed in section 3.4.2.

Microstructure of the IG processed samples

Figures 3.20 (a), (b), (c), (d) and (e), show the optical microstructures of Nd-422 preforms infiltrated with liquid phases at 1115°C for 15 minutes and quenched. The compositions of the liquid phase sources were Nd-123 with 0%, 10%, 20%, 30% and 40% Nd-422, respectively and the samples will be referred to as Nd-O(IG) to Nd-40(IG). A uniform infiltration of the liquids is evident in Figs. 3.20(b), (c) and (d). The ease with

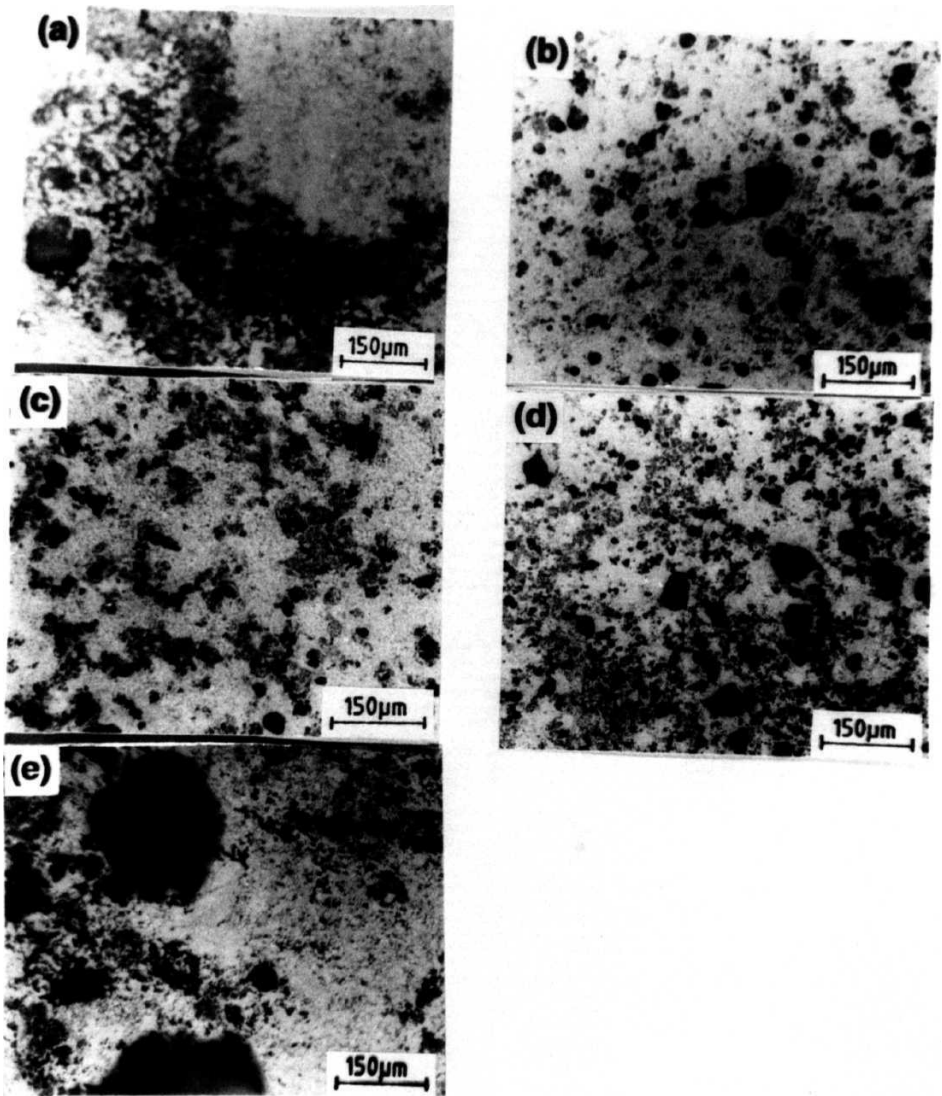
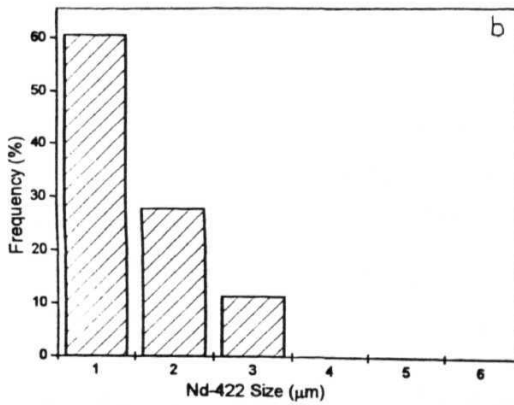
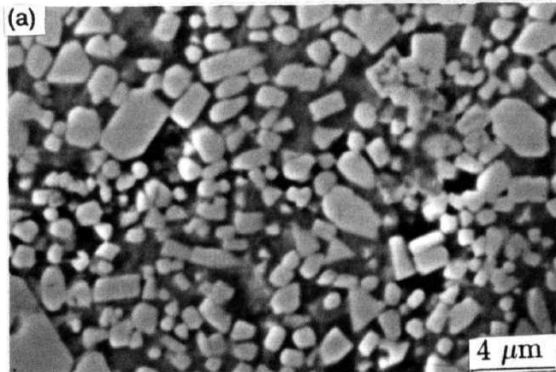


Fig. 3.20 Quenched **microstructures** of Nd-422 preforms infiltrated with liquid phases at 1115°C . The compositions of the liquid phase sources are Nd-123 with (a) 0%, (b) 10% (c) 20%, (d) 30% and (e) 40% Nd-422 respectively.

which the preforms are wetted and infiltrated by the liquids, **without** the aid of any externally provided driving force, is very significant for the fabrication of large complex-shaped components. Figure 3.21 (a) is an SEM micrograph of an infiltrated and quenched sample. The **distribution** of the initial Nd-422 in the liquid can be seen from it. The particles are rounded by interacting with the liquid phase. The size distribution of the particles is shown graphically in Fig. 3.21 (b). The initial Nd-422 are found to be fine-sized and its distribution in the liquid after infiltration is very uniform. The size distribution can be modified to a large extent by varying the experimental conditions.

The above characteristics of the pro-peritectic mixture may be compared with the characteristics of the pro-peritectic Nd-422 + Liquid in the case of other variations [1,36,37] of the melt growth technique. Most of the shrinkage in the conventionally melt processed sample occurs at the melting stage leading to uneven size changes and distortions. The outflow of the low viscosity liquid, and uneven shrinkage at high temperatures leave behind macroscopic 'hollows' as big as a few millimeters in size in the interior of the samples. The escape of gases due to oxygen evolution during the melting of 123 and moving of liquid phase towards poorly packed Nd-422 acicular particles causes microporosity [19,20] and segregation. The liquid phase that fill such pores cause 422-free regions, liquid phase pools etc. in the final **microstructure**. All the above sources of problems are eliminated in the present process involving the infiltration of liquid phases into a preform of Nd-422 from a separate source for the former. The smaller particle size and uniform distribution of the pro-peritectic Nd-422 in the liquid promotes quicker and uniform completion of the peritectic reaction leading to Nd-123 phase. The quicker reaction results from the fact that the peritectic reaction leading to Nd-123 is driven by the small size of the Nd-422 particle in the liquid through the Gibbs-Thomson undercooling.



3.21 (a) SEM micrograph showing infiltrated liquid in Nd-422 preform, (b) distribution of initial Nd-422 size in the liquid phase.

It is well known that in conventional ceramic processing, the shrinkage accompanying heat treatment of the sample can give rise to cracks and distortions. The Infiltration and Growth (IG) processed samples were free of macroscopic internal defects. The samples revealed no shrinkage or distortions. The final melt textured sample has the same size of the preform (1.5 cm x 1.5 cm x 0.5 cm). These observations are relevant to the fabrication of large complex-shaped samples in near-net shape form.

The domains in the IG processed samples were nearly of the same size and geometry as those in the conventionally melt (CM) processed **Nd-123** [45] (section 3.5). As is to be expected from the fact that no 123 decomposition takes place in the preform, minimal microporosity occurs in the final microstructure of the melt processed sample.

Figures 3.22(a), (b), and (c) show the microstructure after melt processing (i.e., after slow cooling through the peritectic temperature at 1°C/h) of the IG samples of Nd-20(IG), Nd-30(IG) and Nd-40(IG), respectively, under polarized light. Nd-20(IG), Nd-30(IG) and Nd-40(IG) refer to the melt processed samples fabricated with the liquid phase source compositions Nd-123 : Nd-422 = 80 : 20; 70 : 30 and 60 : 40 respectively. Clean and defect-free domain boundaries (high angle boundaries) without any liquid phase segregation can be seen in the case of Nd-20(IG) and Nd-30(IG). There are 422-free regions along some domain boundaries in Nd-40(IG) (Fig. 3.22(c)). Since most of the boundaries are free of such defects in Nd-40(IG) the transport J_{cs} are not likely to be affected by such defects.

In the IG processed samples, the domains also consist of parallel platelets of 123 with a common c-axis, separated by nearly equal gaps. The parallel platelets are on an average $2.5\ \mu\text{m}$ in width and the gaps between the platelets are $\sim 0.25\ \mu\text{m}$ in width. In

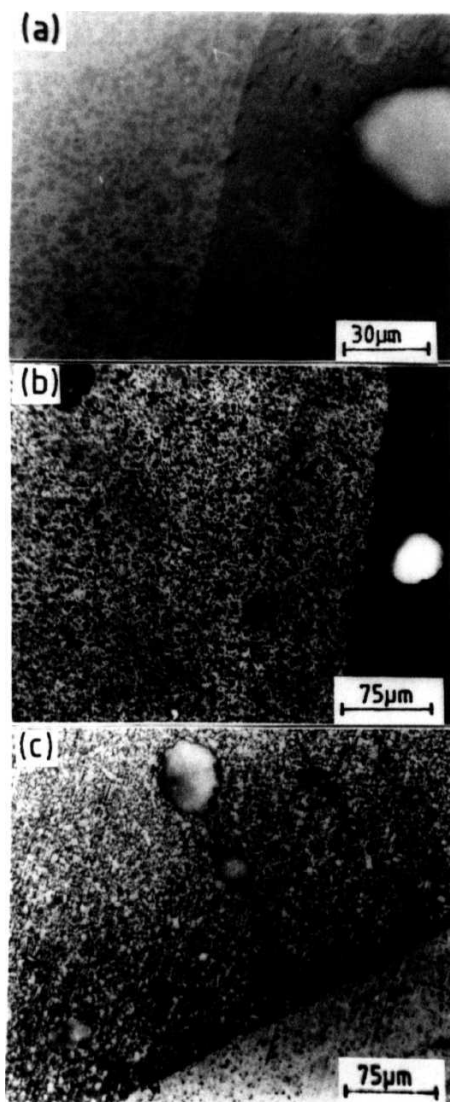


Fig. 3.22 Polarized optical micrograph of final composite (i.e, after slow cooling through the **peritectic** temperature) of (a) Nd-20, (b) Nd-30 and (c) Nd-40 IG processed samples.

conventionally melt processed Nd-123, the **platelet** widths and the gap widths systematically decrease with increasing amounts of Nd-422 [45]. The concentration of Nd-422 at which the Nd-123 platelet and gap widths match with that of the IG processed sample is ~ 36 mol % of Nd-422. The Nd-422 content in the IG processed sample, estimated using standard **metallographic** techniques is in agreement with the above from the values of average platelet and gap widths. It is interesting to note that the amount of Nd-422 present in the IG processed sample is nearly equal to that in compositions optimized for the best J_c values in conventionally melt processed **Y-123**.

It can be seen from Fig. 3.23 (a) and (b) for **Nd-20(IG)** and Nd-40(IG), respectively, that the spherical shaped Nd-422 particles are uniformly distributed in the Nd-123 matrix. The **microstructure** of a conventionally processed 123 sample with comparable Nd-422 concentration is shown in Fig. 3.23(c). The Nd-422 particles are found to be larger in size and to be acicular in the latter case with a relatively large aspect ratio. It is well known [6,7] that smaller spherical Y-211 particles cause secondary defects of sizes comparable to the coherence length in the 123 matrix at the **Y-211/Y-123** interface. Such defects start occurring when the radius of curvature of the 123/211 interface is less than $0.2 \mu\text{m}$ [6,7]. The smaller spherical Nd-422 particles obtained in IG processed samples will be of interest from the point of view of their potential to generate flux pinning secondary defects. Recent TEM studies in Nd-123 system reveals that Nd-123/Nd-422 interfacial pinning has limited effect on flux pinning [46]. The interface in Nd-123/Nd-422 is not as sharp as in **Y123/Y211** materials. The interfacial pinning plays a dominant role at high temperatures and low fields. Enhancement of J_c in considerable amount at low fields has been achieved by adding extra 10-20 mol% Nd-422 phase inclusions in Nd-123 system [47,48].

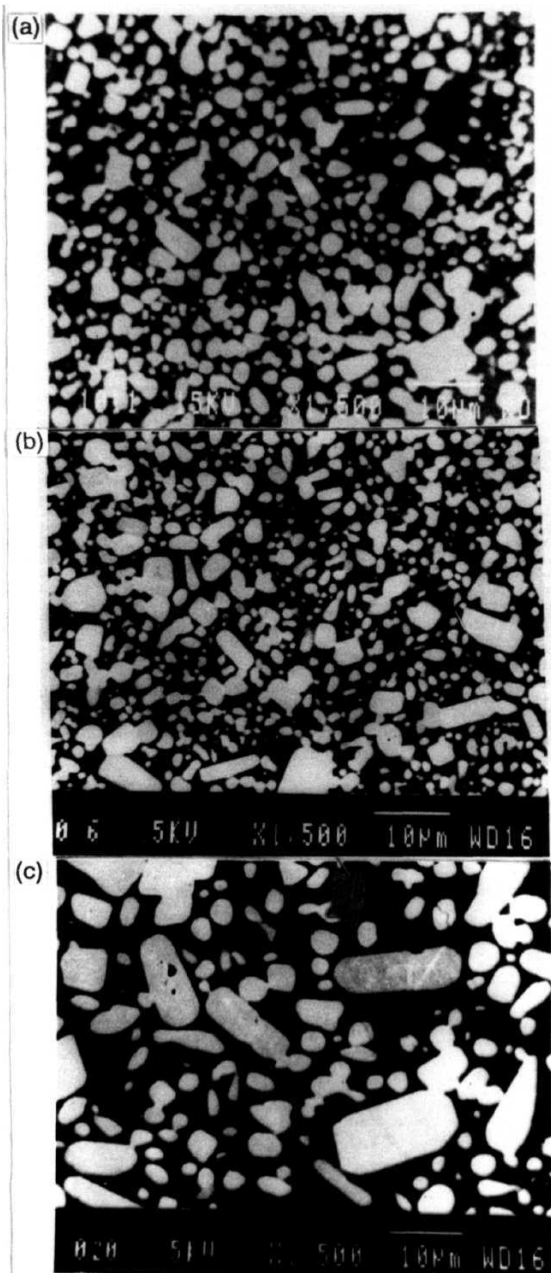


Fig. 3.23 SEM micrograph of final composite (i.e, after slow cooling through the **peritectic temperature**) of (a) Nd-20 and (b) Nd-40 IG processed samples. (c) SEM micrograph of CM processed sample.

Figure 3.24 shows a quantitative analysis of Nd-422 particle size obtained using standard **metallographic** technique for the samples whose microstructures are shown in Figs. 3.23 (a), (b) and (c). The behavior of the **IG** processed samples, processed with two different compositions for the liquid phase (Nd-20(IG) and Nd-40(IG)) have almost identical microstructural parameters. It is encouraging to note that the composition of the liquid phase source is thus not very critical as long as it is not outside a relatively wide range (in the present case $123 : 422 = 90 : 10$ to $70 : 30$) so as not to leave liquid phase free regions in the infiltrated sample. It is also seen from Fig. 3.24 that the IG processed samples have nearly 80% of these Nd-422 particles of size less than $1\ \mu\text{m}$ which could be small enough to cause the required secondary defects. This is nearly 42% in the case of samples produced by the usual melt processing route.

In Fig. 3.25, the effect of melt processing the Nd-123 samples in commercial Argon (8 ppm of oxygen) and in high purity Argon (4 ppm of oxygen) on T_c is shown. The samples processed in high purity Ar show sharp resistive transitions around 93 K. The samples processed in commercial Ar show broad transitions, with an onset transition temperature around 89 K and the zero resistance occurs only at 80 K. The high T_c phase formation in Nd-123 is highly sensitive to the atmosphere in which the processing is carried out. In Fig. 3.26, we show the X-ray diffraction patterns of IG processed Nd-20(IG) and Nd-40(IG) samples. The presence of Nd-123 with a high degree of c-axis texturing can be noticed in the pattern for Nd-20(IG). The pattern also evidences the presence of Nd-422 phase. However, in the case of Nd-40(IG), the X-ray lines from Nd-123 phase are extremely weak. The low intensity of the Nd-123 lines could be due to the relatively lower amount of the phase present in the Nd-422 rich sample.

The results of magnetization measurements performed on the IG sample were discussed in the Chapter 6. This IG **process**, avoids shrinkage during **processing** and also

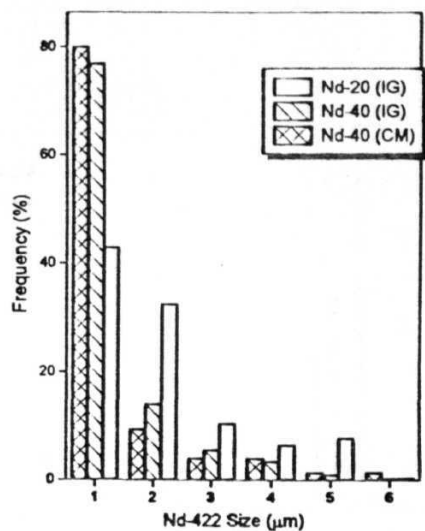


Fig. 3.24 Nd-422 particle size distribution for IG processed and CM processed samples.

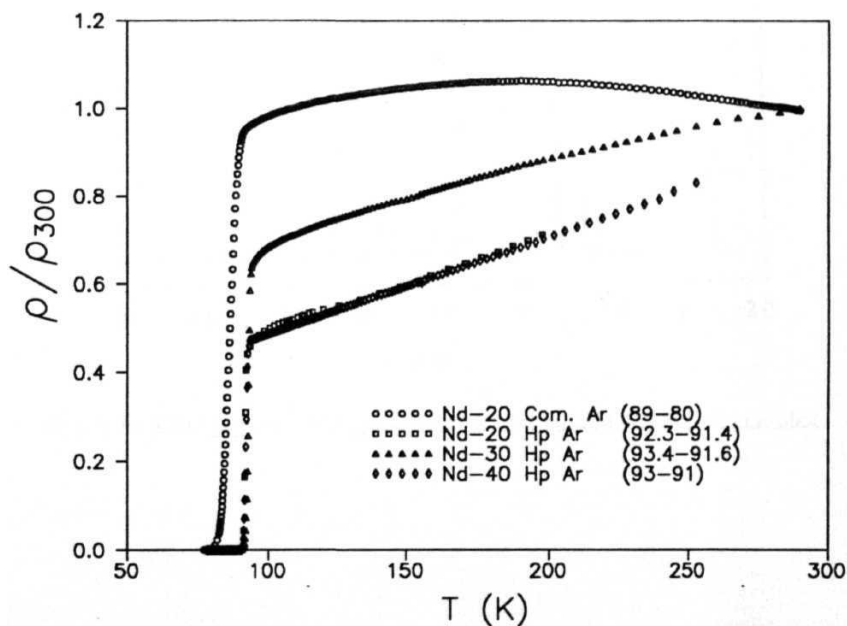


Fig. 3.25 Temperature variation of normalized resistivity for IG samples, processed in various atmospheres.

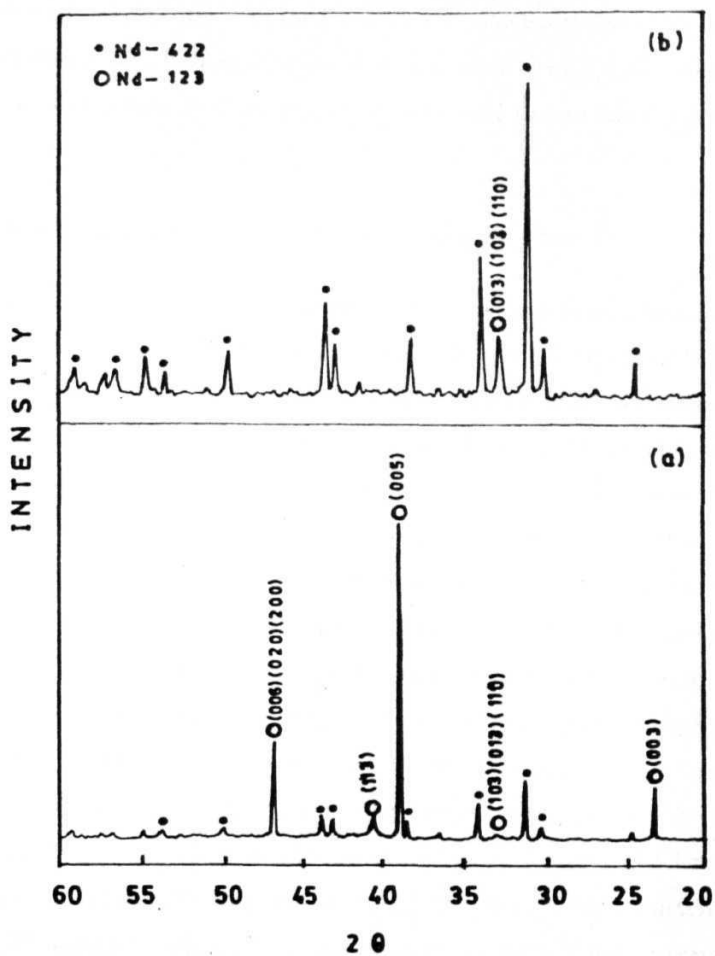


Fig. 3.26 XRD pattern of IG processed (a) Nd-20 and (b) Nd-40 sample

avoids **macroscopic** hollows in large extent, which **occur** in the interior of conventionally melt processed samples. Its use in the fabrication of a hollow **cylinder** had been demonstrated elsewhere [43]. It offers a means of fabrication of large, complex-shaped high J_c components with nearly the final 'geometry', with good surface finish and dimensional control.

3.8 Effect of rates of cooling on IG processed samples

Melt growth experiments through IG process were carried out as described in the section 3.7 at various rates of cooling. The cooling rates were 1, 4, 10, 20, and 40 °C/h through the peritectic temperature (T_p). All the IG processed samples with different rates of cooling had an average domain size of 5-6 mm². Figure 3.27 shows the optical microstructure of a domain boundary for a sample cooled at a rate of 40 °C/h. Even for this fast rate of cooling (40 °C/h), majority of the domain boundaries were sharp with no unreacted secondary phases, which is similar to the observed features in a conventionally melt processed sample (see section 3.6). Also, the domain boundaries were free from macrocracks. Each domain contains **fine** sized Nd-422 particles embedded in Nd-123 matrix. These fine Nd-422 particles are uniformly distributed in the Nd-123 matrix as shown in Fig. 3.27(c). Figure 3.28 is the SEM pictures of **intradomain** region for various rates of cooled samples, which shows the morphology of Nd-422 particles in Nd-123 matrix. Nearly spherical shaped Nd-422 particles can be seen for all the samples. Textured platelets were also observed even at higher (40 °C/h) rates of cooling. This type of microstructure with fine sized Nd-422 particles is difficult to obtain in other conventional melt processes due to coarsening of Nd-422 particles in the liquid. The above results suggest that the Nd-123 can be melt processed in a short time, with fine Nd-422 particles embedded in textured Nd-123 matrix, using the IG process.

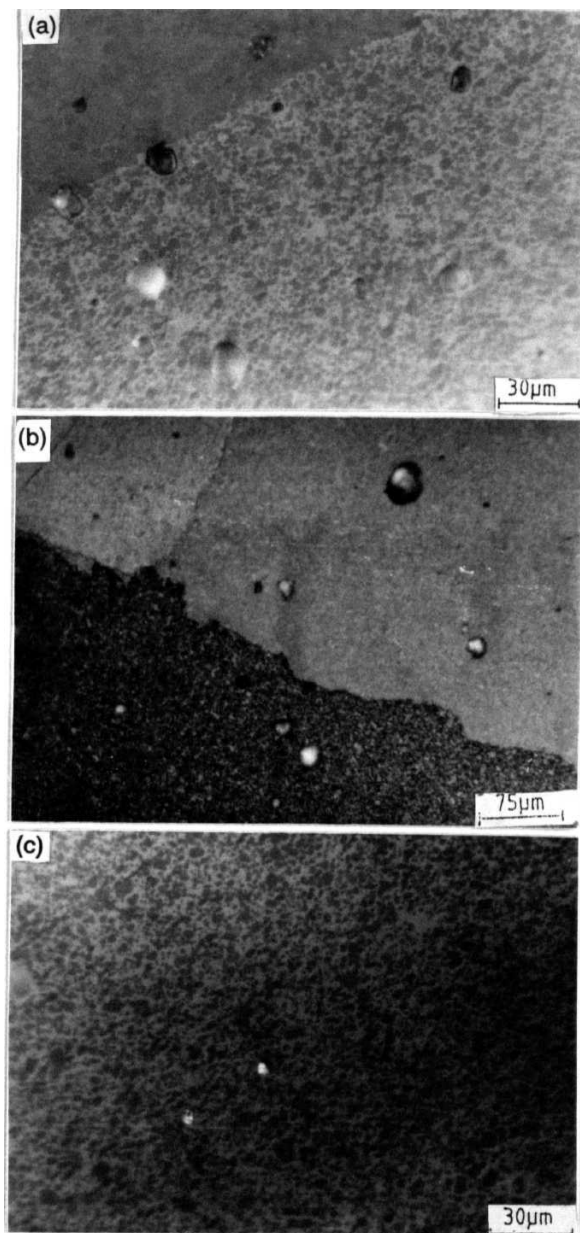


Fig. 3.27 Microstructures of IG processed sample cooled at 40 °C/h, showing (a) clean domain boundary, (b) domain boundary with liquid phase and (c) uniform distribution of fine sized Nd-422 particles. Absence of microporosity can also be seen.

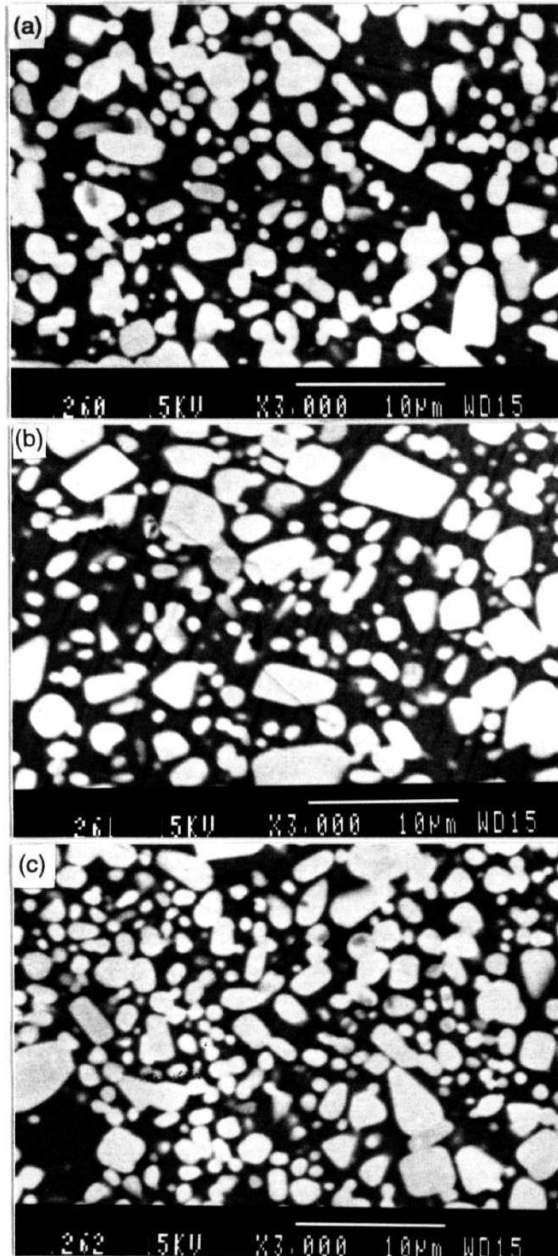


Fig. 3.28 SEM micrographs of IG processed samples cooled at (a) 10 °C/h, (b) 20 °C/h and (c) 40 °C/h.

References

- [1] S. Jin, T. H. Tiefel, R. C. Sherwood, M. E. flavin, R. B. Van Dover, G. W. Kammlott, R. A. Fastnacht, and H. D. Keith, Appl. Phys. Lett. 52, 2074 (1988).
- [2] M. Murakami, S. Gotoh, N. Koshizhuka, S. Tanaka, T. Matsushita, S. Kambe, and K. Kitazawa, Cryogenics, 30, 390 (1990).
- [3] D. F. Lee, V. Selvamanickam and K. Salama, Physica C 202, 83 (1992).
- [4] D. Shi, S. Sengupta, L. S. Lou, C. Varanasi and P. J. McGinn, Physica C **213**, 179-184 (1993).
- [5] M. Murakami, S. Gotoh, H. Fujimoto, K. Yamaguchi, N. Koshizuka and S. Tanaka Supercond. Sci. Technol. 4 S43 (1991).
- [6] R. Gopalan, T. Roy, T. Rajasekharan, G. Rangarajan and N. Hari Babu, Physica C **244**, 106 (1994).
- [7] M. Mironova, D. F. Lee and K. Salama, Physica C **211**, 188 (1993).
Z. L. Wang, A. Goyal, and D. M. Kroeger, Phys. Rev. B, 47, 5373 (1993).
- [8] S. I. Yoo, R. W. Mc Callum, Physica C **210**, 147 (1993).
- [9] T. B. Lindemer, E. D. Specht, P. M. Martin and M. L. Flitcroft, Physica C **255**, 65 (1995).
- [10] K. Takita, H. Katoh, H. Akinaga, M. Nishino, T. Ishigaki and H. Asano, Jpn. J. Appl. Phys. **27**, L57 (1988).
- [11] S. I. Yoo, N. Sakai, H. Takaichi and M. Murakami, Appl. Phys. Lett. 65, 633 (1994).
- [12] M. Murakami, S. I. Yoo, T. Higuchi, N. Sakai, J. Weltz, N. Koshizuka, and S. Tanaka, Jpn. J. Appl. Phys. 33, L715 (1994).
- [13] T. Egi, J. G. Wen, K. Kuroda, H. Unoki and N. Koshizuka, Appl. Phys. Lett. 67, 2406 (1995).
T. Egi, J. G. Wen, K. Kuroda, H. Mori, H. Unoki, N. Koshizuka, Physica C **270**, 223 (1996).
- [14] T. Higuchi, S. I. Yoo, K. Sawada, N. Sakai and M. Murakami, Physica C, 263, 396 (1996).
- [15] N. V. N. Viswanath *et al*, Appl. Phys. Lett., (1997) (In press).
- [16] H. Shaked, B. W. Veal, J. Faber, R. L. Hetterman, U. Balachandran, G. Tomlins, H. Shi, L. Morss, and A. P. Paulikas, Phys. Rev. B **41**, 4173 (1990).
- [17] D. Dimos, P. Chaudhari, and J. Mannhart, Phys. Rev. B **41**, 4038 (1990).
- [18] R. D. Shannon, Acta Crystallogr. A 32 751 (1976).
- [19] C. J. Kim, G. H. Lee, K. B. Kim and G. W. Hong, J. Mater. Res., 10, 2235 (1995).
- [20] E. Sudhakar Reddy and T. Rajasekharan, Supercond. Sci. and Tech. (In press).
- [21] G. Schmitz, J. Laakmann, C. Wolters, S. Rex, W. Gawalek, T. Habisreuther, G. Bruchlos and P. Gönert, J. Mater. Res. **8**, 2774 (1993).
- [22] E. Sudhakar Reddy and T. Rajasekharan, Phys. Rev. B, (1997) (In press).
- [23] C. J. Kim, Y. S. Lee, H. S. Park, I. H. Kuk, T. H. Sung, J. J. Kim and G. W. Hong, Physica C **276**, 101 (1997).
- [24] S. Jin, T. H. Tiefel, R. C. Sherwood, R. B. van Dover, M. E. Davis, G. W. Kammlott, and R. A. Fastnacht, Phys. Rev. B 37, 7850 (1988).
- [25] C. Krauns, M. Sumida, M. Tagami, Y. Yamada and Y. Shiohara, Z. Phys. B 96, 207 (1994).
- [26] M. A. Rodriguez, B. J. Chen and R.L. Snyder, Physica C **195**, 185 (1992).
- [27] M. Nakamura, M. Kambara, T. Umeda, Y. Shohara, Physica C **266**, 178 (1996).

- [28] **K Salama, A. S. Parikh, L. Woolf, Appl Phys. Lett. C8, 1993 (1996).**
- [29] **X. Yao, K. Furuya, Y. Nakamura, J. Wen, A Endoh, M. Sumida and V. Shiohara, J Mater. Res 10 [12], 3003(1995).**
- [30] **K.B Alexander, A. Goyal, D. M. Kroeger, V. Selvamanikam, and K Salama, Phy». Rev. B 45, 5622 (1992).**
- [31] **Yao, X , Mizukoshi, T., Egami, M., Zama, H , Nakamura, M., and Shiohara, Y.: Jpn. J Appl. Phys. 35, 2126 (1996).**
- [32] **Yao, X., Mizukoshi, T., Egami, M., Shiohara, Y.:** Physica C **263** 197 (1996).
- [33] **Nakamura, M., Kutami, H., Shiohara, Y.:** Physica C **260**, 297 (1996).
- [34] **Li, S., Hayri, E.A., Ramanujachary, K.V., Greenblatt, M.:** Phys. Rev. B 38, 2450 (1988).
- [35] **Salama, K., Parikh, AS., Woolf, L.:** Appl. Phys. Lett. 68, 1993 (1996).
- [36] **K. Salama, V. Selvamanickam, L. Gao and K. Sun, Appl. Phys. Lett., 54 [23] 2352 (1989).**
- [37] **M. Murakami, M. Morita, K. Doi and K. Miyamoto, Jpn. J. Appl. Phys., 28 [7] 1189 (1989).**
- [38] **Z. Lian, Z. pingxian, J. Ping, W. Keguang, W. Jingrong and W. Xiaozu, Supercond. Sci. Tech., 3 490 (1990).**
- [39] **D. Shi, S. Sengupta, L. S. Lou, C. Varanasi and P. J. McGinn, Physica C, 213 179 (1993).**
- [40] **M. Murakami, Supercond. Sci. Tech., 9 1015 (1996).**
- [41] **C. J. Kim, H. W. Park, K. B. Kim, K. W. Lee, I. H. Kul and G. W. Hong, Mater. Lett. (in press).**
- [42] **N. Hari Babu, T. Rajasekharan, L. Menon and S.K Malik, J. American Ceramic Society, 1998 (In press).**
- [43] **T. Rajasekharan, E. Sudhakar Reddy, N. V. N. Viswanath and N. Hari Babu, Proc. of ASMCCD, Mumbai, India. September 17-20, 1996; E. Sudhakar Reddy and T. Rajasekharan, J. Mater. Res. (In press).**
- [44] **A. W. Urquhart, Mater. Sci. Engg., A144 75 (1991).**
- [45] **N. Hari Babu and T. Rajasekharan (To be published).**
- [46] **R. Yu, F. Sandiumenge, B. Martinez, N. Vilalta, and X. Obradors, Appl. Phys. Lett., 71, 413 (1997).**
- [47] **S. I. Yoo., N. Sakai, H. Kojo, S. Takebayashi, N. Hayashi, M. Takahashi, K. Sawada, T. Higuchi, and M. Murakami, IEEE Trans. Appl. Supercond. 7, 1781 (1997).**
- [48] **A. Takagi, T. Yamazaki, T Oka, Y. Yanagi, Y. Itoh, M. Yoshikawa, Y. Yamada, U. Mizutani, Physica C 250 222 (1995).**

Chapter 4

ac susceptibility measurements

This chapter deals with the experimental results obtained from ac susceptibility measurements performed using a home made mutual inductance setup described in Chapter 2. Initially, the methods of analysis were established using the data obtained from sintered Bi-Sr-Ca-Cu-O (BSCCO) sample, and were later extended to sintered and melt textured Nd-Ba-Cu-O (NdBCO) samples.

4.1 Introduction

Characterizing a superconducting transition is commonly achieved by measuring the temperature dependence of electrical resistivity. This works very well in the case of homogeneous samples where both the critical temperature T_c , and the transition width ΔT_c , are unambiguously defined and can be used as a check for purity. However, in practice, a superconducting transition is associated with a more complicated behavior in the case of granular samples where superconducting grains of higher critical current density (J_c) are linked by low J_c regions like grain boundaries, impurity phases that form the intergranular region, with distinct critical parameters (T_c , H_c , J_c etc.). Accordingly, chemical inhomogeneities are known to exist in the case of $\text{NdBa}_2\text{Cu}_3\text{O}_{7-\delta}$ (Nd-123) superconductor because it forms low T_c solid solution phases of the type $\text{Nd}_{1+x}\text{Ba}_{2-x}\text{Cu}_3\text{O}_{7-\delta}$, when processed in air. Formation of these extra phases can be suppressed by processing Nd-123 in reduced oxygen partial pressure. However, there could be some minor amounts of

these phases **that** form locally in the Nd **123** matrix. In this case the **electrical** transition corresponds only to the percolation limit and is not characteristic of the whole volume of the sample. Magnetic **characterization** techniques offer a higher sensitivity to the individual phases present in the **sample**. They are also easier because of the absence of problems associated with making electrical contacts.

The magnetic response of conventional superconductors was initially studied by Maxwell and Strongin [1], Ishida and Mazaki [2], Khoder [3] and Hein [4]. ac susceptibility is measured as $\chi = \chi' + i\chi''$, where the real part χ' is the in-phase signal and the imaginary part χ'' is the out of phase signal with respect to the applied ac field. The real part reflects the screening properties expressed as a difference in the energy (associated with the magnetic field) of the sample between the nonsuperconducting and the superconducting states. The imaginary part corresponds to the ac losses that represent the amount of ac magnetic energy converted to heat in the sample.

Bean's critical state model for the magnetization of **type-II** superconductors, which assumes J_c to be independent of local magnetic field, predicts the existence of only odd-harmonic susceptibilities. Experimental studies on fundamental and higher-harmonic susceptibility were carried out by Ishida and Mazaki [5] in a **multi** connected low temperature superconductor and similar studies were reported later in HTSCs by many other groups [6-18].

4.2 Temperature variation of ac susceptibility

4.2.1 Polycrystalline NdBCO sample

The **temperature** variation of fundamental ac susceptibility measured at different ac fields on the polycrystalline (sintered) NdBCO sample is shown in Fig. 4.1. $\chi'(T)$ has a broad transition, reaching the value of -1 at low temperatures when the **Meissner** state (complete shielding) is reached. The broadness of the transition is seen to increase with the ac field amplitude, but the dc electrical resistivity measured on the same sample shows a relatively sharp transition at 93 K (Fig. 3.3) with a transition width of 2 K. The electrical transition measures the T_c to be 93 K which is the percolation limit through the high T_c phase and is not characteristic of a transition throughout the whole volume of the sample. The appearance of a peak in the χ'' versus temperature is a very common feature associated with the superconducting transition. The maximum occurs at a temperature T_m which is lower than the critical temperature T_c . The full width at half maximum of the peak increases and T_m decreases with increasing applied ac field. The peak in χ'' occurs at the point where the ac **magnetic-field** just reaches to the center of the sample [19]. The reason for the occurrence of the peak is that if one first considers a temperature far below T_c , and H_{ac} is less than the lower critical field of the intergranular region, H_{ci1} , the screening current generated by the alternating field is confined to a region near the sample surface, and little or no magnetic flux enters the bulk of the sample. Then χ'' is small or even zero. As the temperature is allowed to increase, and both J_c and H_{ci1} decrease, the field begins to penetrate the sample and the intergranular ac loss ($\propto \chi''$) increases as the magnetic energy absorption increases. This process continues until the field penetrates the sample completely and reaches the center of the sample. As the temperature increases further, less and less of the sample volume remains superconducting as the magnetic flux penetrates more and more into the sample, so that less and less

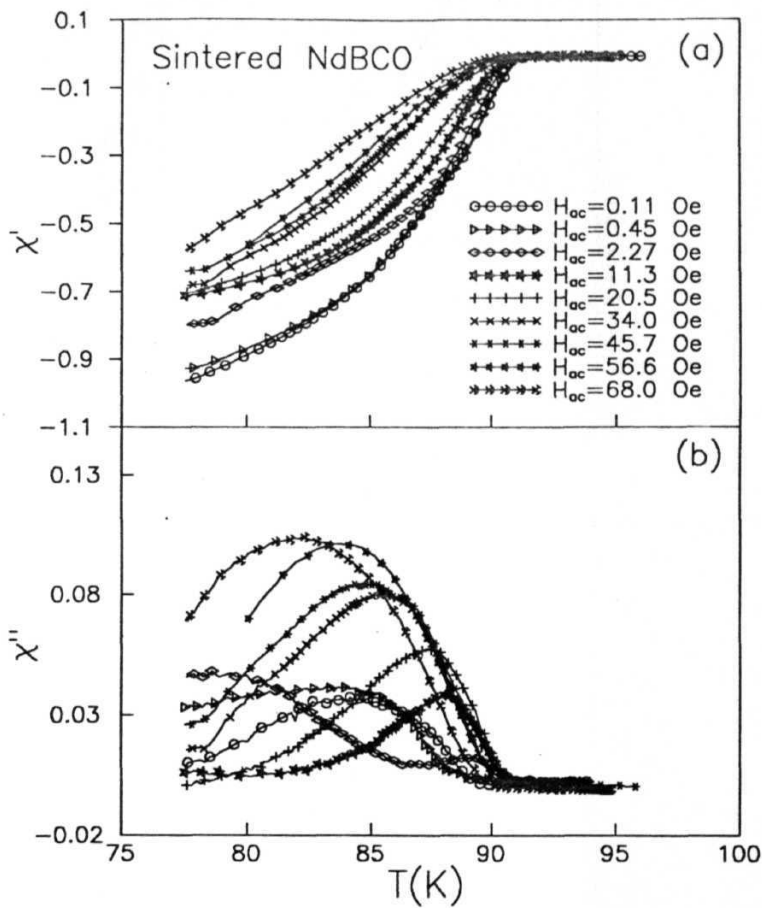


Fig. 4.1 Temperature dependence of the (a) real part (χ') and (b) imaginary part (χ'') of the fundamental susceptibility of the sintered $NdBa_2Cu_3O_{7-\delta}$ for different ac fields at 77 K.

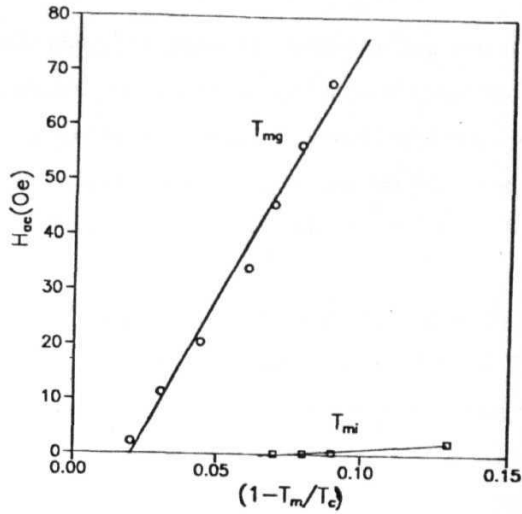


Fig. 4.2. Field dependence of the ac loss peak position for sintered NdBCO sample. Solid line shows the fit-to $H_{ac} \approx H(o)(1 - (T_m/T_c))$.

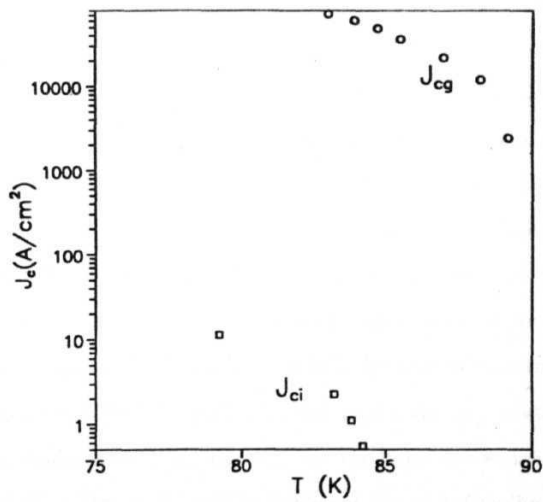


Fig. 4.3. Temperature variation of critical current density, calculated from the peak position of ac loss using Bean's model.

magnetic loss takes place and χ'' decreases, eventually **reaching** zero at T_c . Existence of two loss peaks (Fig. 4.1 (b)) in **the** sample is an **indication** of granularity of **the** specimen wherein the grains are coupled by weak links or Josephson-type junctions [10-18]. Here, the peak in χ'' close to T_c is due to the loss in the grains, and can be understood on lines similar to those discussed for **the** intergranular peak.

The loss peak is found to shift towards lower temperatures as the ac field strength is increased. The origin of such a shift can be understood as follows. The pinning force at temperature T_m has a value such that Abrikosov vortices just reach the center of the sample. To attain the same situation at a higher ac field amplitude, strong pinning forces are required. Therefore, the maxima of χ'' shift to lower temperatures with increasing H_{ac} . The field dependence of the loss peak positions allows a qualitative estimate of the pinning force density. Figure 4.2 shows the variation of the peak temperatures of χ'' **for** the intergranular and intragranular regions, T_{mi} and T_{mg} respectively, with the ac field amplitude. The intergranular peak position is found to vary as $H_{ac} \propto (1 - T_{mi}/T_c)$. Variation in the intragranular peak position is found to follow the relation $H_{ac} \propto (1 - T_{mg}/T_c)^2$, which is unusual since the pinning force in the grains is proportional to H_{cg}^2 for Abrikosov vortices, where H_{cg} is the **thermodynamical** critical field of the grains [20]. The expected behavior is $H \propto (1 - (T_{mg}/T_c)^2)$ for the grains [20]. By applying Bean's critical state model, it is possible [21] to use the field dependence of loss peak temperature (T_{mi} or T_{mg}), to determine the temperature dependence of the critical current density close to T_c . According to the model, the critical current is a consequence of the gradient of the flux lines that exist as the flux is driven into the superconductor. For a granular superconductor there are both intergrain J_{ci} , and intragrain, J_{cg} , components given by $H^* = J_{ci}d/2$, $H_g^* = J_{cg}R_g$, where H^* and H_g^* are the fields for which flux just reaches the center of a slab of thickness d and the center of a grain of radius R_g , respectively.

Figure 4.3 clearly shows that $J_{cg} \gg J_{ci}$, as expected. J_{cg} is very high due to the strong pinning of flux within the grains. The rapid shift in the intergranular loss (χ'') peak position with respect to H_{ac} represents a strong temperature and field dependence of J_{ci} for the intergranular region, indicating that there are no strong pinning along the boundaries of the grains. The drastic variation in χ'' grain peak position with H_{ac} is unusual since grains exhibit larger pinning forces when compared to intergranular region [20]. But in this particular sample, the grain loss peak position is also significantly field dependent which might have its origin in the solid solution formation as evidenced by broad diamagnetic transition.

4.2.2 Melt textured NdBCO samples

In this section we present the results of temperature variation measurements of ac susceptibility on various multidomain bulk melt textured NdBCO samples, which were prepared as described in section 3.4.2. The sizes of the samples used for the study are 4 mm x 4 mm x 12 mm.

Figure 4.4 shows the ac susceptibility measured on various samples, viz. **Nd-123** with 0, 10, 20, 30 and 40 mol% Nd-422, which are here referred to as Nd-0, **Nd-10**, Nd-20, Nd-30 and Nd-40 respectively. All these samples were processed in high purity Argon atmosphere and the rate of cooling through peritectic temperature (T_p) was 1 °C/h (see Fig. 3.6). Temperature variation of χ' shows single sharp diamagnetic transition around 92 K with a transition width of ~ 2 K and that of χ'' shows a narrow peak for all the samples. These observations are indicative of suppression of solid solution phase formation in melt textured NdBCO samples.

The Nd-40 sample processed in commercial Argon atmosphere (referred to as **Nd-40-S**)

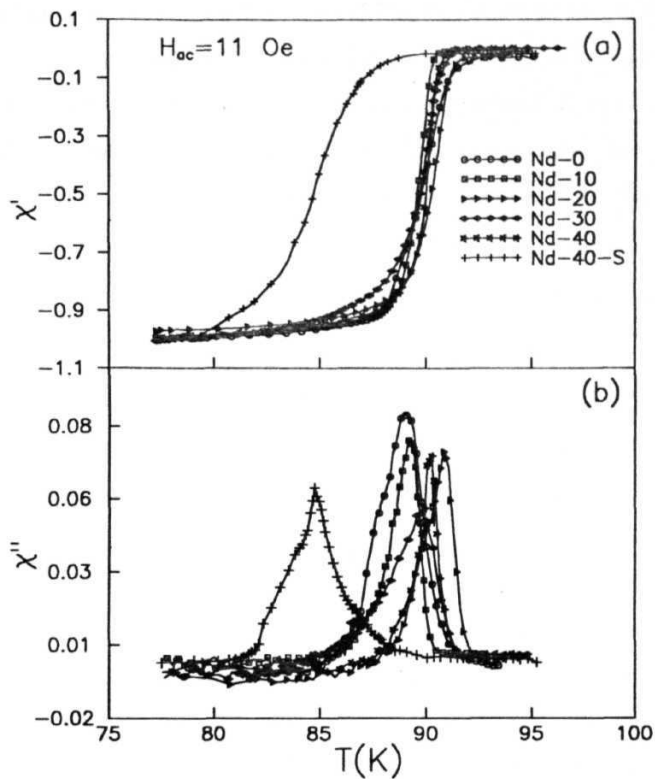


Fig. 4.4 Temperature dependence of measured fundamental susceptibility, (a) χ' and (b) χ'' of various melt textured N123-Nd422 composites. Solid lines are guide to the eye.

shows a broad diamagnetic transition at 90 K with a transition width of 8 K and a broad χ'' peak, indicating a distribution of T_c s. This could be due to either oxygen deficiency or existence of solid solutions. Even though the samples were annealed in oxygen atmosphere for a long time, there was no change in the transition width suggesting the formation of solid solutions to be more likely. Since the samples processed in high pure Argon atmosphere showed sharp diamagnetic transition at 92 K, the purity of Argon seems to be an important parameter during processing.

ac susceptibility measurements at different ac fields applied along the longer axis of the samples.

Figure 4.5 shows the temperature variation of ac susceptibility measured on Nd-0 sample at various ac fields. The maximum applied ac field strength was 68 Oe. The χ' curve is found to become slightly broader with increasing H_{ac} values, but no kink or shoulder appeared in the transition region of the curve. For all H_{ac} values, measured χ'' exhibited only a single peak as opposed to the behavior of the sintered material (see Fig. 4.1). As H_{ac} is increased, features like an increase in the broadness of χ'' , an increase in the peak height followed by saturation, and a shift in the peak temperature towards lower temperatures are observed. The decrease of ac loss peak height with decrease of H_{ac} is attributed to reversible fluxoid motion and is discussed in section 4.3. Figures 4.6, 4.7, 4.8 and 4.9 show the measured temperature variation of the in phase and out-of phase components of ac susceptibility on Nd-10, Nd-20, Nd-30 and Nd-40 samples at various fields respectively. Similar features are seen in these samples as well, but with relatively sharper diamagnetic transition and sharper peaks in χ'' when compared to the stoichiometric Nd-123 (Nd-0). However, in the case of Nd-40 sample alone, a shoulder appeared at low temperature beside the χ'' peak. The shifts in the peak positions are less dependent on the applied field. Due to strong pinning of vortices, in the melt textured samples, the peak in χ'' appears at a higher temperature, and its position is only slightly

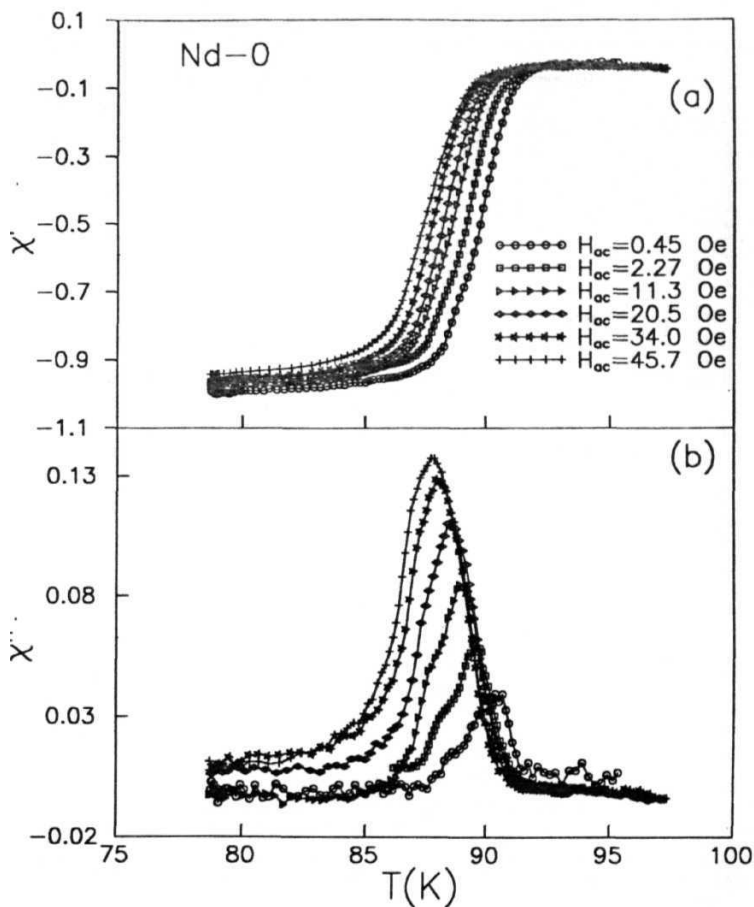


Fig. 4.5 Temperature dependence of measured fundamental susceptibility, (a) χ' and (b) χ'' of the melt textured multidomain Nd-0 superconductor for different ac fields. Solid lines are guide to the eye. Peak value of the χ'' can be seen to be reducing with decrease of H_{ac} , which is attributed to reversible fluxoid motion of a pinned vortex lattice.

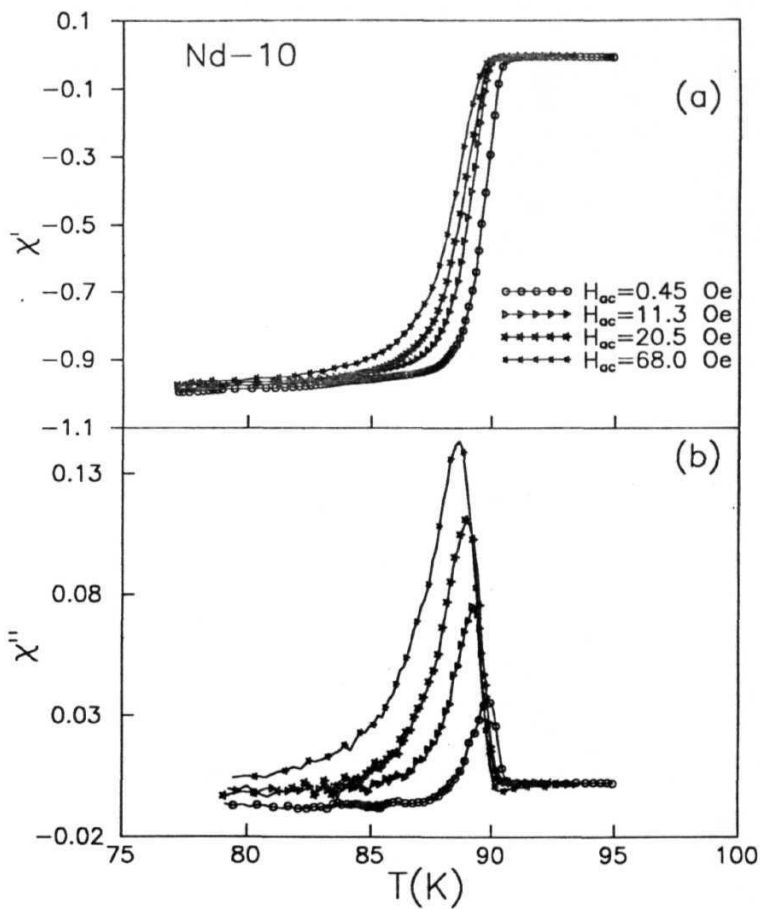


Fig. 4.6 Temperature dependence of measured fundamental susceptibility, (a) χ' and (b) χ'' of the melt textured multidomain Nd-10 superconductor for different ac fields. Solid lines are guide to the eye.

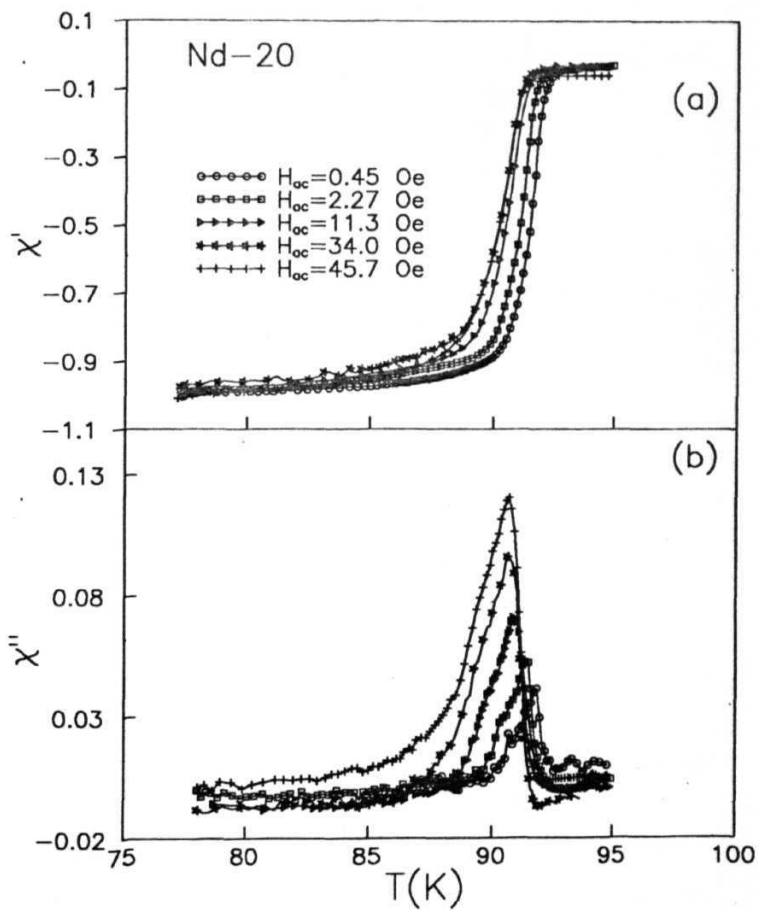


Fig. 4.7 Temperature dependence of measured fundamental susceptibility, (a) χ' and (b) χ'' of the melt textured multidomain Nd-20 superconductor for different ac fields. Solid lines are guide to the eye.

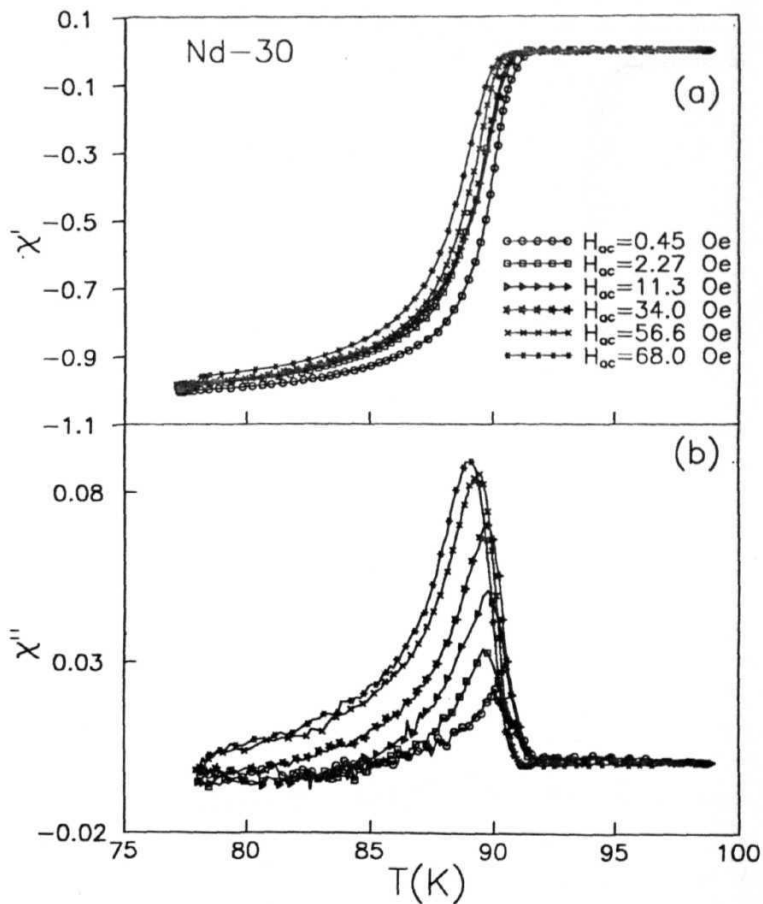


Fig. 4.8 Temperature dependence of measured fundamental susceptibility, (a) χ' and (b) χ'' of the melt textured multidomain Nd-30 superconductor for different ac fields. Solid lines are guide to the eye.

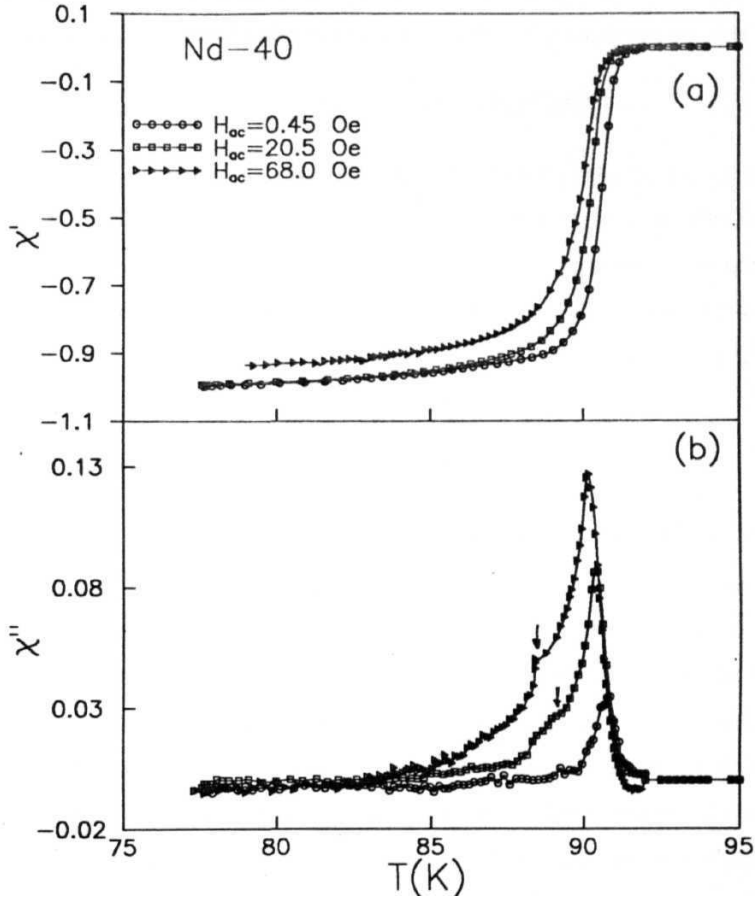


Fig. 4.9 Temperature dependence of measured fundamental susceptibility, (a) χ' and (b) χ'' of the melt textured multidomain Nd-40 superconductor for different ac fields. Solid lines are guide to the eye. Development of a second loss peak in χ'' is due to anisotropy in pinning.

affected by the changing field amplitude due to a weak field dependence of J_c . This is analogous to the behavior of the intragrain peak in the sintered samples [22]. The field dependence of the peak position is found to follow the empirical formula,

$$H_{ac} = H(o)(1 - (T_m/T_c)^2)^4 \quad (4.2.1)$$

and is shown in Fig. 4.10; here $H(o)$ is a constant and is related to the pinning force density at $T = 0$. As H_{ac} is increased, the penetrated flux front just reaches the cylinder axis at the value $H_{ac} = H_p$, where $H_p = J_c R$, this situation corresponds to a maximum in the dissipative component χ'' . In the critical state models, $J_c(H)$ is assumed to vary as K/H_o and $K/(H+H_o)$ by Bean and Kim respectively, where K is the pinning force density and is dependent only on the temperature. In the limit $H \rightarrow 0$, $J_c(H = 0, T) = K(T)/H_o$. This implies that the temperature dependence of $J_c(H = 0, T)$ is just that of pinning force density $K(T)$. Muller *et al.* [22] reported $K(T) \sim (1 - (T_mj/T_c)^2)$ for YBCO sintered rods, leading to $J_{cj}(T) \sim (T_c - T)^2$. For single crystals of YBCO, Wu and Sridhar [23] reported $K(T) \sim (1 - (T/T_c)^2)^2$. The parameter $H(0)$ is tabulated for all the samples in Table 4.1. Estimated bulk critical current density J_c at 88 K from Eqn. 4.2.1 is also tabulated. The critical current density is found to have increased as the Nd-422 content in the sample is increased upto Nd-30 sample and decreased for Nd-40 sample. If the melt textured samples were to exhibit weaklink nature we would observe two peaks in χ'' with the position of the low temperature peak being strongly affected by the external field and also two different diamagnetic transitions in χ' as in the case of sintered samples. Absence of a second peak and an observation of a sharp diamagnetic transition indicate that melt textured NdBCO samples prepared by the above route do not have significant amount of weaklink regions inside the sample.

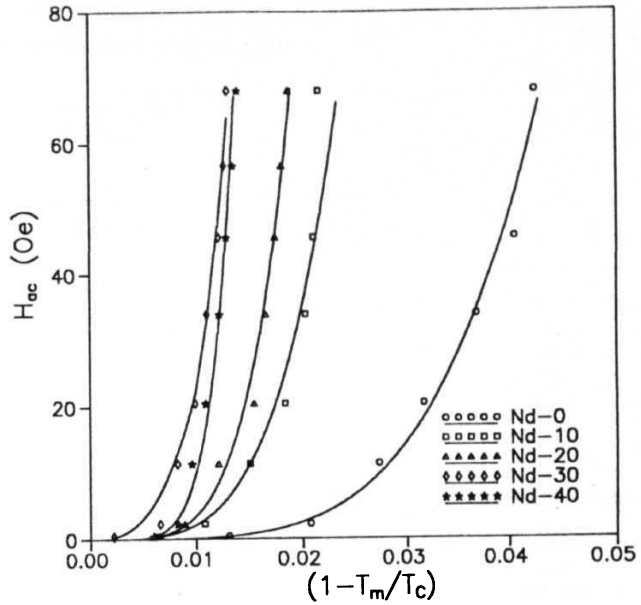


Fig. 4.10 Field dependence of the ac loss peak position for various melt textured samples. Solid line shows the fit to $H_{ac} = H(0) (1 - (T_m/T_c)^2)^4$.

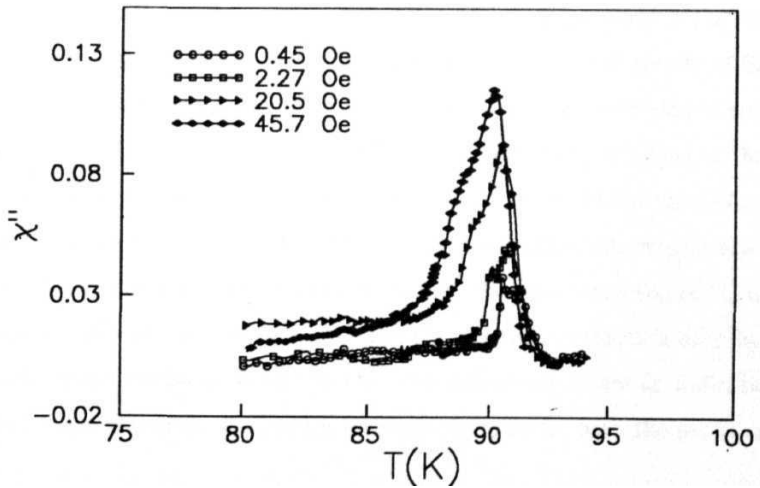


Fig. 4.11 Temperature dependence of χ'' when the field is applied perpendicular to the length of the sample showing two peaks. When the field was applied along the length of the sample, a major sharp peak was observed (Fig. 4.9) with a minor peak.

Table 4.1 Fit parameter $H(o)$ in Eqn. 4.2.1.

	$H(o)$	J_c (88 K)
		A/cm^2
Nd-0	1.31×10^6	1.7×10^2
Nd-10	1.72×10^7	6.0×10^2
Nd-20	2.39×10^7	1.9×10^3
Nd-30	1.42×10^8	3.0×10^3
Nd-40	1.05×10^8	2.2×10^3

It is seen in Fig. 4.9 that there is an additional peak (shoulder) in the χ'' **peak** which is also weakly field dependent. In order to understand the origin of this, ac susceptibility is recorded when the field is applied perpendicular to the longer axis of the sample. Figure 4.11 shows the data that exhibits two peaks in χ'' . The most important aspect in the data on the imaginary components is that the boundary between the two loss peaks becomes indistinct as the ac magnetic field increases to > 15 Oe. This phenomenon is entirely different from the case of sintered NdBCO sample, and also from the results of Shinde *et al* [24]. In the sintered case (Fig. 4.1), the two separate peaks always stayed apart as H_{ac} increased from about 1 to 68 Oe and the distance between the maxima of the two loss peaks became larger and larger. Here (Nd-40 sample), the widths of the peaks have increased as the ac magnetic field is increased, but the maximum width remains less than 2 K when the field is increased from 0.45 Oe to 68 Oe. The peak temperature T_m moves to low temperatures when ac field increases, but the total displacement is only by 1 K when the field changes between 68 to 0.45 Oe. These observations are an indication of a weak field dependence of the loss, which is nearly the same for both the peaks and is

given by

$$J_c(T) = J_c(0)(1 - (T/T_c)^2)^2$$

On the contrary, for a weak-link junction, the critical current density at temperature T is given by [25],

$$J_c(T) \propto [\pi \Delta(T)/2e R_n \tanh[\Delta(T)/2k_B T]] \quad (4.2.2)$$

where R_n is the tunneling resistance per unit area of the junction in the normal state and $2\Delta(T)$ is the energy gap. For T close to T_c , $J_c(T) \propto (1 - T/T_c)$. Since the observed field dependence is much weaker, it can be concluded that the two peaks are not associated with the loss at weaklinks.

The melt textured sample consists of several domains which do not necessarily have the same orientation [26]. As a result, ac magnetic response can be resolved as c and ab components. The above two observed peaks can be ascribed to χ'' loss, associated with the c and ab components. In other words, the two peaks are caused by anisotropy of pinning in the ab (basal) plane and along the c-axis. Resolution of ab and c components is observed as shown in Fig. 4.9. Better resolution of the two peaks, when H is applied perpendicular to the longer axis of the sample is observed. This is analogous to the observations made by Couach *et al.* [27] in Y-123 single crystals, where they obtained multiple peaks when the field was applied in the ab (basal) plane and a single major peak when H was parallel to c. Since the high T_c superconductors are layered compounds, in a large sized multidomain sample, misorientation of domains can cause two peaks due to the anisotropy in pinning. The pinning strength along the ab plane is stronger than that parallel to c-axis. Therefore for a well aligned melt textured sample with slightly misoriented domains, the peak at higher temperature is associated with the ab component.

4.3 Reversible fluxoid motion

In the melt textured samples (Figs 4.5-4.9), the peak value of the imaginary χ'' is found to decrease remarkably with decreasing ac magnetic field, accompanied by a shift of its position to higher temperatures. The former behavior contradicts the prediction of the critical state model in which the flux pinning is assumed to be completely irreversible. According to Bean's critical state model [28], χ'' in low frequency range is

$$\chi'' = \frac{4\mu_o H_m}{3\pi J_c d}; \quad H_m \leq J_c d/2 \quad (4.3.1)$$

$$= \frac{\mu_o J_c d}{\pi H_m} \left(1 - \frac{J_c d}{3H_m}\right); \quad H_m > J_c d/2 \quad (4.3.2)$$

where d is the sample size. Thus χ'' takes a maximum value of $3/4\pi = 0.239$, at $H_m = 2/3 J_c d$. The ac loss calculated using the Bean's model predicts that the height of the loss peak is constant. But the observed height of the ac loss peak increases with the applied ac field. A similar observation was made in conventional multifilamentary wires with very fine superconducting filaments [29]. Since all the measurements here were carried out at a low frequency of 33 Hz, the flux line lattice is stable without any creep and the deviation from the critical state model could be due to the reversible fluxoid motion inside the pinning potentials as proposed by Campbell [30]. The reversible ac penetration depth (λ'_c) is the characteristic shielding length of a pinned vortex lattice and hence takes larger values for higher temperatures and for more weakly pinned superconductor. It can be expressed in terms of J_c as $\lambda'_c = (B d_i / \mu_o J_c)^{1/2}$, where B is the magnetic flux density and d_i is the interaction distance representing the radius of the averaged pinning potential. Since the theoretical calculations for fundamental harmonic susceptibilities based on Campbell's reversible fluxoid motion can be done only numerically and are complicated, some approximate formulae have been proposed [31] as

$$\chi'_r = \frac{-\mu_o H_p}{[1 + 3(2\lambda'_c/d)^2]H_p + H_m} \quad (4.3.3)$$

$$\chi_r'' = \frac{2\mu_o}{\pi} \frac{H_p H_m}{3[1 + 2(2\lambda'_c/d)^2]^2 H_p^2 + H_m^2} \quad (4.3.4)$$

where H_p is the full penetration field and equals $J_c d/2$. In the case of $A' \ll d$, the critical state model describes the phenomenon approximately. In order to discuss the temperature dependence of χ' and χ'' , we assume the temperature dependence of J_c and λ'_c . As the temperature approaches T_c , J_c is reduced to zero and λ_c diverges. Here we simply assume,

$$J_c(T) = J_c(o)(1 - t^2)^m \text{ and } \lambda'_c(T) = \lambda'_c(o)(1 - t^2)^{-n} \quad (4.3.5)$$

where $t=T/T_c$ is the reduced temperature and m and n are positive constants. The calculated χ'_r and χ''_r versus temperature at various applied fields are respectively shown in Fig. 4.12, where it has been assumed that $J_c(o) = 8 \times 10^7$ A/cm², $\lambda_c(o) = 0.11$ μ m, $d = 2.5$ μ m, $m = 4$ and $n = 0.5$. The results shown in Fig. 4.9 agree quite well with the theoretical calculations as shown in Fig. 4.12. Figure 4.13 shows the maximum value of measured χ'' , (i.e. χ''_m) versus the applied field obtained from Fig. 4.9 as data points, and the solid line represents the theoretical fit to Eqn. (4.3.4). From this it can be concluded that the observed decrease in the peak value with decrease of ac field could be well described by considering reversible fluxoid motion.

For the appearance of reversible fluxoid motion, the size of the superconducting region in which the current flows uniformly should be smaller than the size of the bulk sample [31]. Microstructure of the Nd-40 sample shows domains consisting of Nd-123 platelets of average size 2-3 μ m separated by 0.2 μ m size gaps. At close to T_c , these gaps prevent the flow of uniform transport current through the sample and the size of the superconducting specimen, in which current flows uniformly, becomes the size of platelets. The platelet size is comparable or less than the Campbell's reversible ac penetration depth (λ'_c) and hence the reduction in ac loss peak.

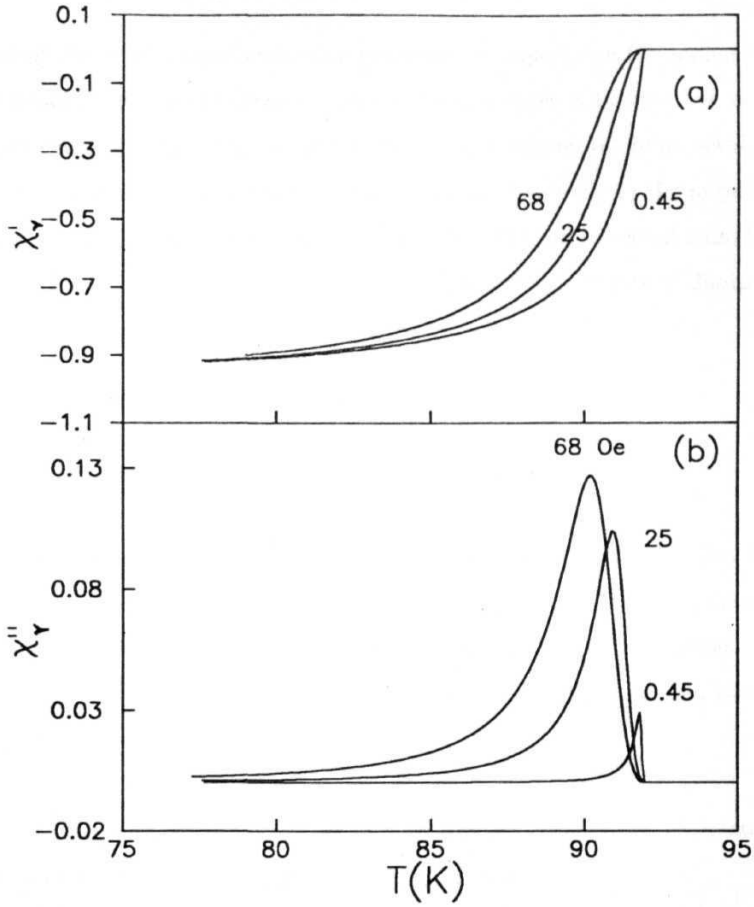


Fig. 4.12 Variation of χ'_r and χ''_r , calculated from the Eqns. (4.3.3) and (4.3.4) for the Nd-40 sample having an average platelet size of $2.5 \mu\text{m}$. Good agreement with the experimental data (Fig. 4.9) can be seen.

4.4 Bulk-pinning hysteresis loss

One of the crucial superconducting properties of importance for applications as power transmission cables operating at elevated temperatures is to have low ac losses at the operating conditions. The loss per cycle per unit volume W_v in an ideal, pinning free, type-II superconductor depends strongly upon the frequency. In the presence of pinning, magnetic hysteresis plays a significant role, and if hysteretic losses dominate, the loss per cycle W becomes independent of frequency. For $J > J_c$, the rate of dissipation per unit volume can be written as [32],

$$JE = E^2/\rho_f + J_c E$$

where E is electric field, and ρ_f is flux flow resistivity.

The first term on the right hand side represents the eddy-current, flux flow or viscous losses. The second term, which describes the pinning losses, gives the rate of heat generation per unit volume near the pinning centers that impede vortex motion. The hysteretic losses dominate when $E \ll \rho J_c$, i.e., when the electric field generated by vortex motion is at a relatively low level.

The energy dissipation W_v , per unit volume per cycle can be calculated as the area enclosed by the $B - H$ loop for $H(t) = H_{ac} \cos(\omega t)$.

$$W_v = \int B dH = \pi \chi'' \mu_o H_{ac}^2 \quad (4.4.1)$$

It is important to recognize, from the orthogonality relations of the trigonometric functions, that Eqn. (4.4.1) remains unchanged inspite of higher harmonic components.

$$i.e., W_v = \pi \chi_1'' \mu_o H_{ac}^2$$

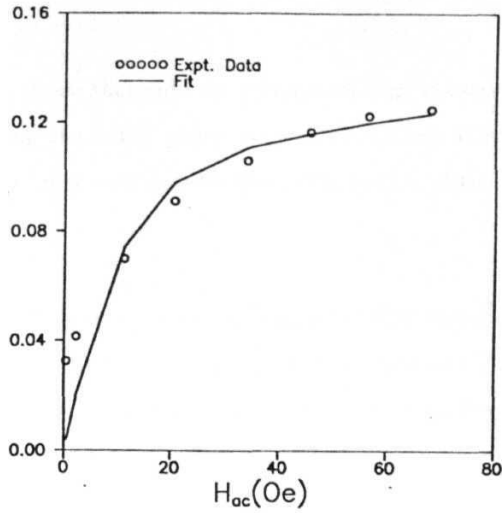


Fig. 4.13 Plot of ac loss peak height with ac field strength, obtained from the Fig. (4.9b). Solid line is a fit to Eqn. (4.3.4).

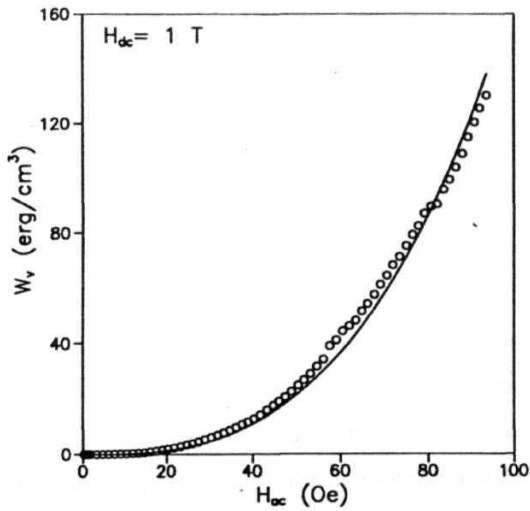


Fig. 4.14 The ac loss per unit volume per cycle of Nd-40 sample at 77 K and 33 Hz, obtained from the imaginary component, χ'' . Solid line is a fit to Eqn. (4.4.2).

The above equation shows that only the fundamental signal carries the energy loss information. Measuring the out-of phase **component** of either fundamental (χ'') or flat band (χ_f'') ac susceptibility would enable the **determination** of the bulk hysteresis losses in HTSCs.

The ac loss per unit **volume** per cycle of sample Nd-40, determined from the measured out-of phase component of flat band susceptibility, is shown in Fig. 4.14 as a function of ac field. The solid line in the figure shows the loss estimated by Bean's critical state model which for small ac fields, is given by,

$$W_v = 5H_{ac}^3/6\pi J_c d \quad (4.4.2)$$

It can be seen that the experimental data is well described by the above expression. Here, since the applied ac field is low, the ac loss is confined only to the surface of the sample and it increases with the ac field following the cubic law.

4.5 Universal behavior of ac susceptibility

There are many reports on the analysis of the temperature dependence of χ based on critical state models [28,33-35]. Chen *et al.* [36] have suggested a way to determine the intergranular J_c , as a function of temperature and the local field from ac susceptibility measurements. Subsequently, there are many reports on the temperature dependence of average J_c obtained for a $\text{YBa}_2\text{Cu}_3\text{O}_7$ (YBCO) sample [36-38] and for the superconducting phases of (Bi,Pb)-Sr-Ca-Cu-O (BSCCO) system [39,40]. Ishida and Goldfarb [41] reported a detailed experimental study of the field (both ac and dc) and temperature dependences of the harmonic susceptibilities of a YBCO superconductor and showed that their results agree well with the predictions of Ji *et al.* [42]. Kim *et al.* [43,44] have

reported a study of the dependence of χ' and χ'' on applied ac and dc fields using a modified critical state model, assuming a critical current density $J_c(h) = H^{-2}$, where h is the local field. Yamaguchi *et al.* [45] have analyzed the frequency and ac field dependence of χ'' versus H_{dc} curves measured for a $Bi_2Sr_2CaCu_2O_8$ single crystal, on the basis of the thermally assisted flux flow model. Shatz *et al.* [46] derived universal expressions for the harmonic susceptibilities of type-II superconductors, using critical state models with a general dependence of the critical current on the magnetic field. The basic assumption of their analysis is that the alternating field acts as a small perturbation to the steady field, i.e. $H_{ac} \ll H_{dc}$, since the flux profile in the regions of the slab affected by the ac field is then approximately linear with a slope $S = \pm 4\pi J(H_{dc})/c$. This slope is related to a parameter $\delta = H_{ac}/(Sa)$ which is a measure of the extent of penetration of the alternating field into the slab. Here, a is the half-thickness of the slab. For a given field dependence of J_c , one can arrive at a universal curve : χ_m versus δ (here δ absorbs the dependence of χ_m on ac, dc fields and the temperature) by choosing an appropriate expression for δ .

δ is given below for various models in the linear regime :

$$\text{Bean's model : } \delta = H_{ac}/H^*$$

$$\text{Anderson - Kim model : } \delta = 2H_{ac}H_{dc}/H_o^2$$

$$\text{Powerlaw model : } \delta = (2 - \gamma)H_{ac}H/H_p^{(2-\gamma)}$$

$$\text{Exponential model : } \delta = H_{ac}\exp(H_{dc}/H_o)/H_o(\exp(H_p/H_o))$$

where γ is a constant. H^* and H_p denote the full penetration fields in Bean's model and the other field dependent models respectively. Fundamental χ'_m and χ''_m are calculated

in terms of δ as given by [46]

$$\chi'_m = -1 + \delta/2 \quad \delta < 1 \quad (4.5.1)$$

$$\cdot -(6/2 - 1)(\alpha/\pi - 1/2) + (\delta/2 + 2/3\delta - 2/3) \cos \alpha/\pi) \quad \delta > 1 \quad (4.5.2)$$

Where $Q = \sin^{-1}(1 - 2/6)$, $\pi/2 < \alpha < 3\pi/2$

$$\chi''_m = 2\delta/3\pi \quad \delta < 1 \quad (4.5.3)$$

$$= 2(3 - 2/\delta)/(3\pi\delta) \quad \delta > 1 \quad (4.5.4)$$

The experimental intergranular matrix susceptibility is extracted from the measured susceptibility using the following equations, [36]

$$X' = f_g x'_g + (1 - f_g) \chi'_m \quad (4.5.5)$$

$$\chi'' = f_g \chi''_g + (1 - f_g) \chi''_m \quad (4.5.6)$$

where f_g is the effective volume fraction of the grains, χ'_m and χ''_m are the components of intergranular matrix susceptibility, χ'_g and χ''_g are that of measured susceptibility. Here, it is assumed that the grain susceptibility $\chi'_g = -1$, at temperatures well below the transition temperature. Shatz *et al.* have demonstrated the universality of the third-harmonic susceptibilities from the measured temperature dependence of susceptibility at different dc fields, in a polycrystalline sample of YBCO.

Here, we initially determined the flux profile in the BSCCO sample at different dc fields using a phase sensitive detection method suggested by Campbell [47,48] and identified the regime where linearity is observed. Further details of flux profiles are discussed in Chapter 5. Then suitability of different models describing field dependence of J_c have been examined through a fit of the field dependence of χ'_m and χ''_m to Eqns. 4.5.1-4.5.4 derived from individual models. Universality of the fundamental intergranular

matrix susceptibility obtained for sintered $Bi_{1.2}Pb_{0.3}Sr_{1.5}Ca_2Cu_3O_y$ superconductor is first demonstrated. **Subsequently** the universal **behavior** of the fundamental ac susceptibility measured for melt textured NdBCO (Nd-40) superconductor is examined from an analysis of the dc field and temperature dependences of the measured susceptibility, $\chi(H_{dc}, H_{ac})_T$ and $\chi(T, H_{dc})_{H_{ac}}$ respectively. Here the magnitude of ac field is chosen to be much less than H_{dc} so that the variation of critical current density over the ac field amplitude is a constant.

4.5.1 Field dependence of ac susceptibility in BSCCO superconductor

The ac susceptibility χ' and χ'' are measured as a function of dc field (H_{dc}) in the range of 0 to 80 Oe, which was superimposed by an ac field (H_{ac}) at fixed temperatures 77 K and 85 K. The plots of χ' and χ'' as a function of $\log_{10}(H_{dc})$ at 77 K and 85 K are shown in Fig. 4.15 and Fig. 4.16 respectively. The position of χ''_{\max} shifts towards lower dc fields as the ac field amplitude is increased. For $H_{ac} \ll H_{dc}$, where the flux profile in the regions of the slab affected by the alternating field is nearly linear, $\chi''(H_{dc})$ curves show a single peak while for ac fields higher than 96 A/m an anomalous behaviour (a dip) is observed. χ' is found to show a dip at $H_{ac} = H_{dc}$, which is attributed to an increase of average J_c of the sample due to the effective field being zero during a short time. To determine the experimental intergranular matrix susceptibility $\chi_m(H_{dc}, H_{ac})_T$ from Eqns. 4.5.5 and 4.5.6, we need to know the f_g value. Firstly, the components χ'_m and χ''_m of experimental intergranular matrix susceptibility are extracted from the measured susceptibility using equations 4.5.5 and 4.5.6, and by choosing appropriate f_g that satisfies the equations, as described in Ref. 39. Then, χ_m is calculated from the values of χ'_m and χ''_m . Figure 4.17 shows the experimental χ'_m and χ''_m (discrete points) along with the theoretical matrix susceptibility derived from the Kim's, power-law and the exponential models as a function of the field. From the figure it can be seen that the

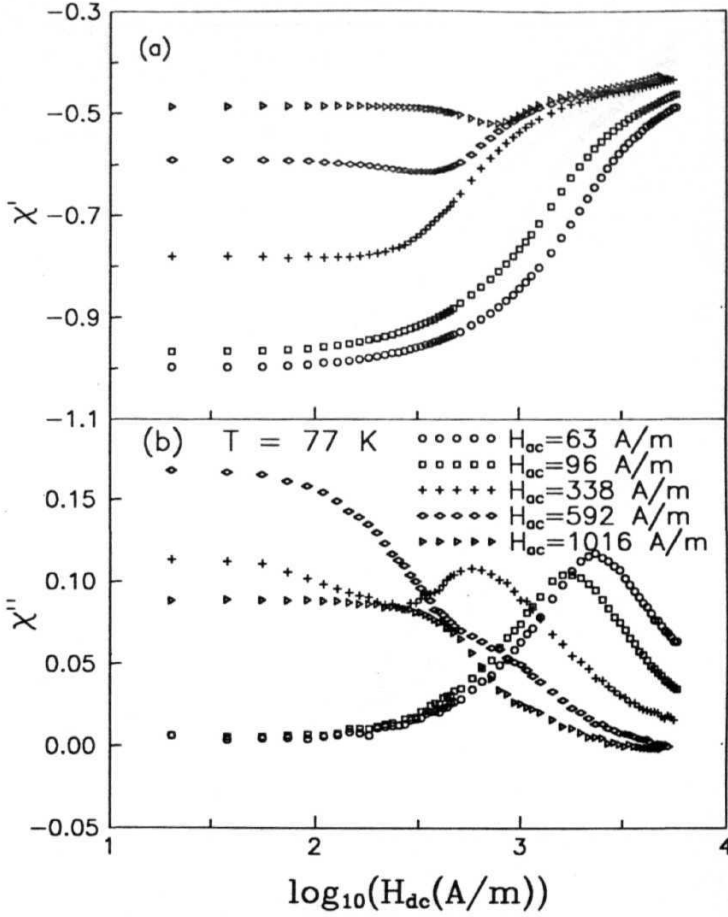


Fig. 4.15 The dc field dependence of measured fundamental ac susceptibility, (a) χ' , and (b) χ'' of the $Bi_{1.2}Pb_{0.3}Sr_{1.5}Ca_2Cu_3O_{10}$ slab for different ac fields (H_{ac}) at 77 K.

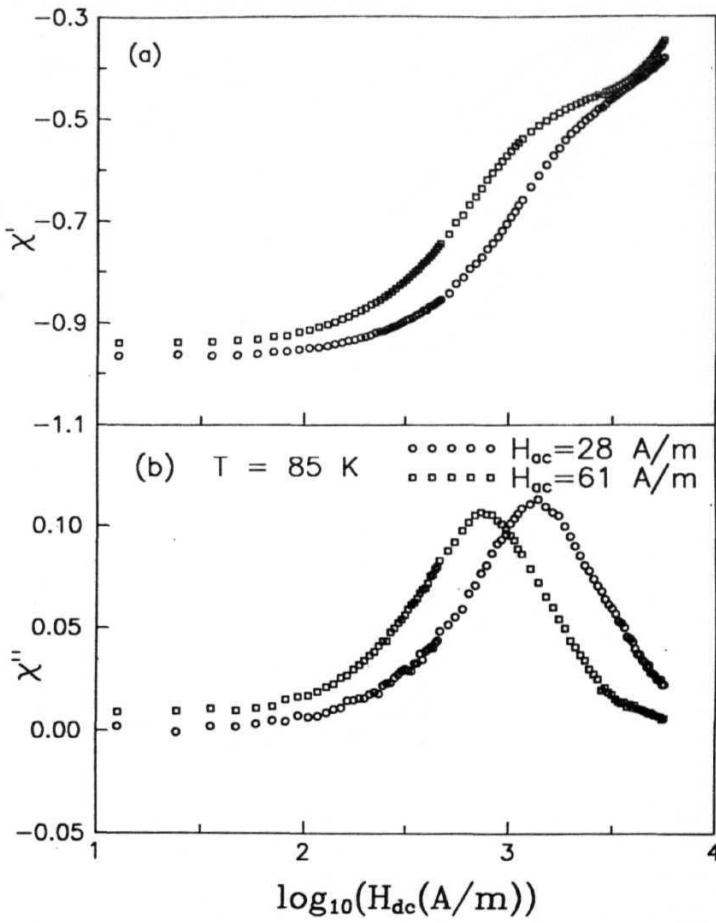


Fig. 4.16 The dc field dependence of measured fundamental ac susceptibility, (a) χ' , and (b) χ'' of the BSCCO slab for two different ac fields (H_{ac}) at 85 K.

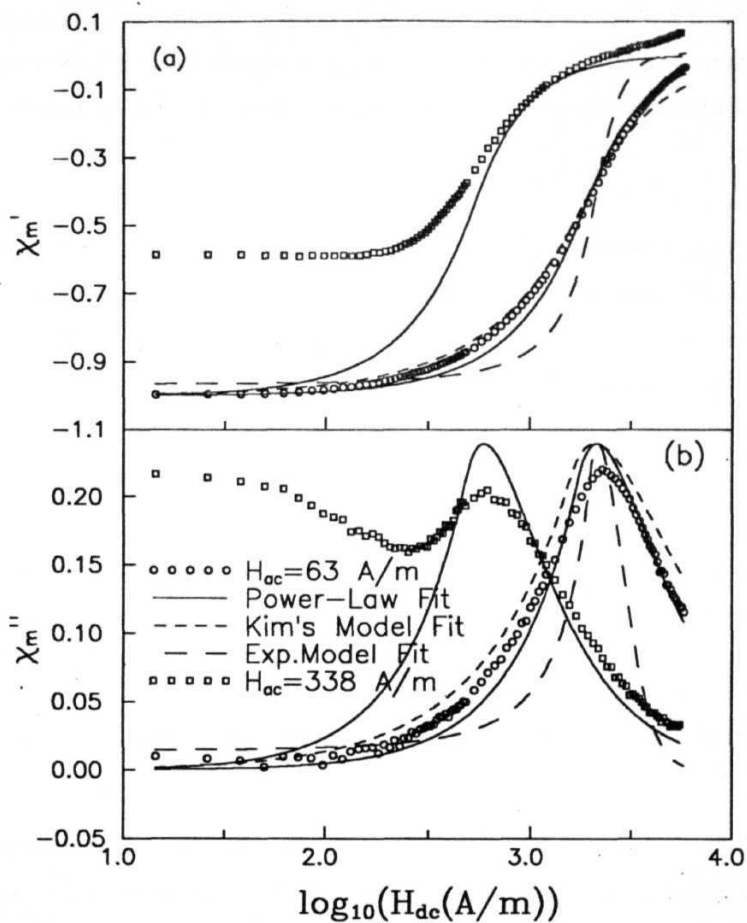


Fig. 4.17 Field dependence of (a) real and (b) imaginary components of intergranular matrix susceptibility (χ'_m, χ''_m) at 77 K determined from the measured susceptibility (Fig. 4.15) is shown as discrete points. The theoretical fits to different models are shown as solid and dashed lines.

power-law with $\gamma = -0.4$ and $H_p = 000$ A/m gives the best fit. Sharpness of χ_m'' peak increases as one goes from Kim's model to exponential model. $\delta(H_{dc}, H_{ac})_T$ values are determined from the experimental χ_m , using equations 4.5.1-4.5.4 and are shown in Fig. 4.18 as discrete points. Field dependence of δ is found to be described well by

$$\delta = (2 - \gamma) H_{dc}^{(1-\gamma)} H_{ac} / H_p^{(2-\gamma)} \quad (4.5.7)$$

derived based on the power law model with $\gamma = -0.4$, for small ac fields. The full penetration fields (H_p) at 77 K and 85 K are obtained as 600 A/m and 309 A/m. Theoretical $\delta(H_{dc}, H_{ac})_T$ are seen to deviate from the experimental data at higher ac fields, since the Eqs. 4.5.1- 4.5.4 are valid only in the regime of linear flux profile in the slab. As a result, at higher ac fields the experimental χ_m cannot be analyzed in terms of the universal model of Shatz *et al.*.

The universal curve is then obtained by plotting the measured $\chi_m(H_{dc}, H_{ac})_T$ as a function of δ (determined from the fit parameters using Eq. (4.5.7)) and is shown in Fig. 4.19, as the four curves with $T = 77$ K and 85 K.

4.5.2 Temperature dependence of ac susceptibility in BSCCO superconductor

The temperature dependence of ac susceptibility $\chi(T, H_{dc})_{H_{ac}}$ was measured in the temperature range from 77 to 120 K. A small ac field at 33 Hz and a high dc field were chosen to be applied, such that $H_{ac} \ll H_{dc}$ for the flux profile in the slab to be linear. $\chi'(T)$, and $\chi''(T)$ measured at different dc fields and a constant ac field of 17 A/m are shown in Figs. 4.20(a) and 4.20(b). The experimental $\chi_m(T, H_{dc})_{H_{ac}}$ is determined from Eqs. 4.5.5 and 4.5.6 and $\delta(T, H_{dc})_{H_{ac}}$ is then determined using equations 4.5.1-4.5.4. Figure 4.21 shows the T dependence of δ at different H_{dc} as discrete points. Power law model

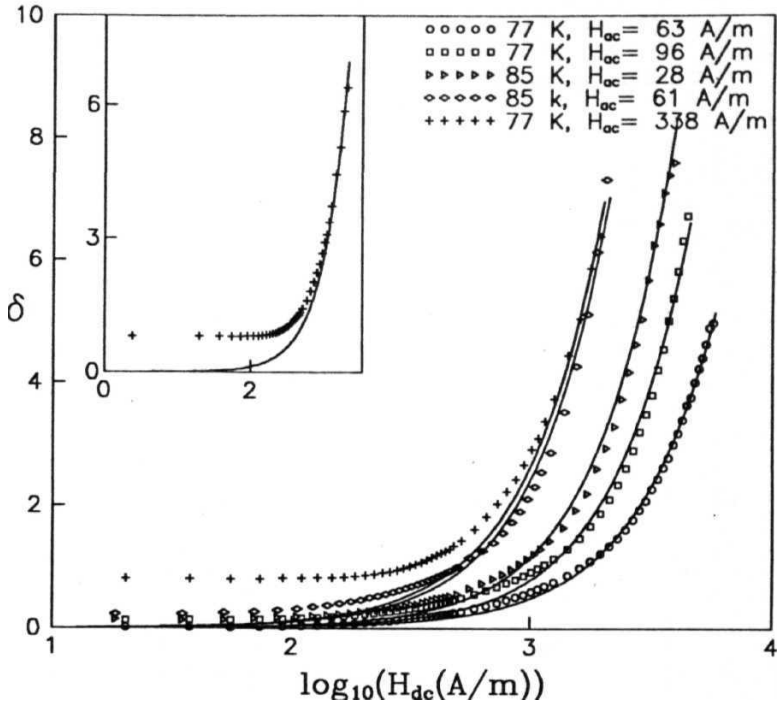


Fig. 4.18 Field dependence of δ extracted from $\chi_m(H_{dc})$ data obtained at 77 K and 85 K for various ac fields (discrete points). Theoretical fits of the S to power-law model (Eqn. 4.5.7) are shown as lines. Inset shows deviation of fit from the data at higher ac fields.

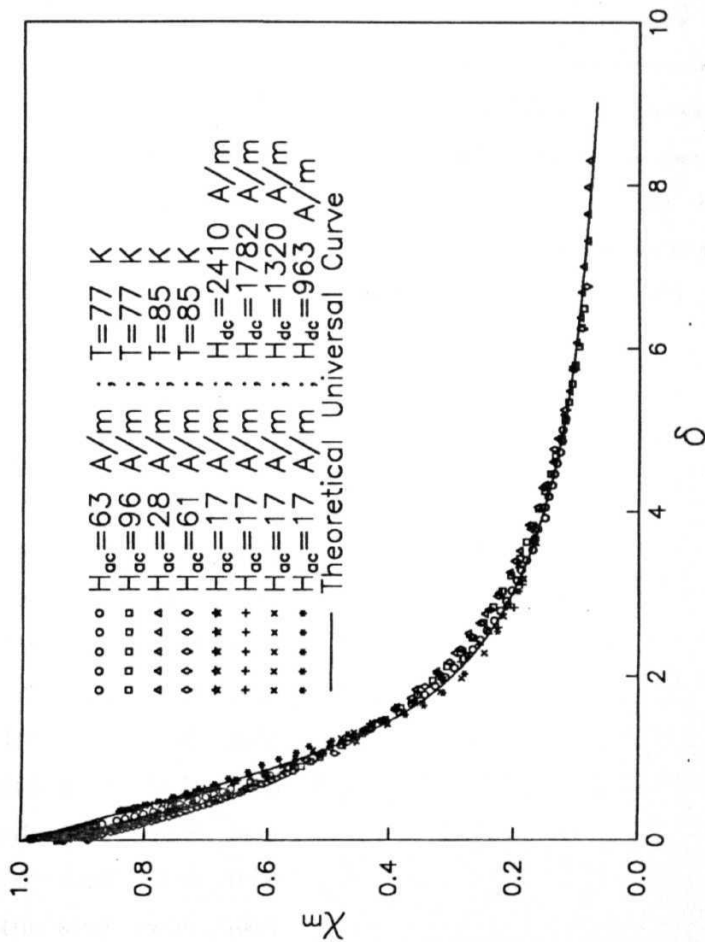


Fig. 4.19 A number of curves plotted for experimental χ_m as a function of δ , using both the measured field and temperature dependences of χ_m , are shown to demonstrate universality of fundamental susceptibility in BSCCO sample.

is chosen to define the relationship between J_c and H_{dc} . The variation of H_p with T is assumed [49,50] to be $H_p(T) = 7/(0)[[1 - (T/T_c)^2][1 - (T/T_i)^2]^\beta]$, where β is a constant. Strong dependence of δ on T suggests that $\delta(T)$ can be expressed as

$$\delta(T) = P_0/[1 - (T/T_c)^2][1 - (T/T_i)^2]^n \quad (4.5.8)$$

Here, the $[1 - (T/T_c)^2]$ term arises from the temperature dependence of pinning force, which is field independent, and varies slowly with temperature. The second term is derived from an assumed [49] temperature dependence of critical current, and T_i is the irreversibility temperature. Our data is found to fit well for $n = 1$. The values of the best fit for P_0 , T_i , and T_c from the curves obtained for different H_{dc} are shown in Table 4.2 and the corresponding theoretical curves of $S(T)$ calculated from Eqn. 4.5.8 are shown in Fig. 4.21 as solid lines. The universal curve is then obtained by plotting the measured $\chi_m(T, H_{dc})_{H_{ac}}$ against the $\delta(T)$ determined from the fit parameters and is shown in Fig. 4.19 as the curves for different H_{dc} .

Table 4.2 Fit parameters in Eqn. 4.5.8.

H_{dc}	P_0	T_i	T_c
A/m		K	K
120	0.021	100.86	103.4
240	0.023	99.87	103.2
358	0.024	97.48	102.9
477	0.030	97.29	102.8
716	0.044	96.08	102.3
962	0.046	94.71	101.6
1320	0.046	92.96	101.4
1782	0.053	91.78	101.0
2410	0.059	91.01	100.7

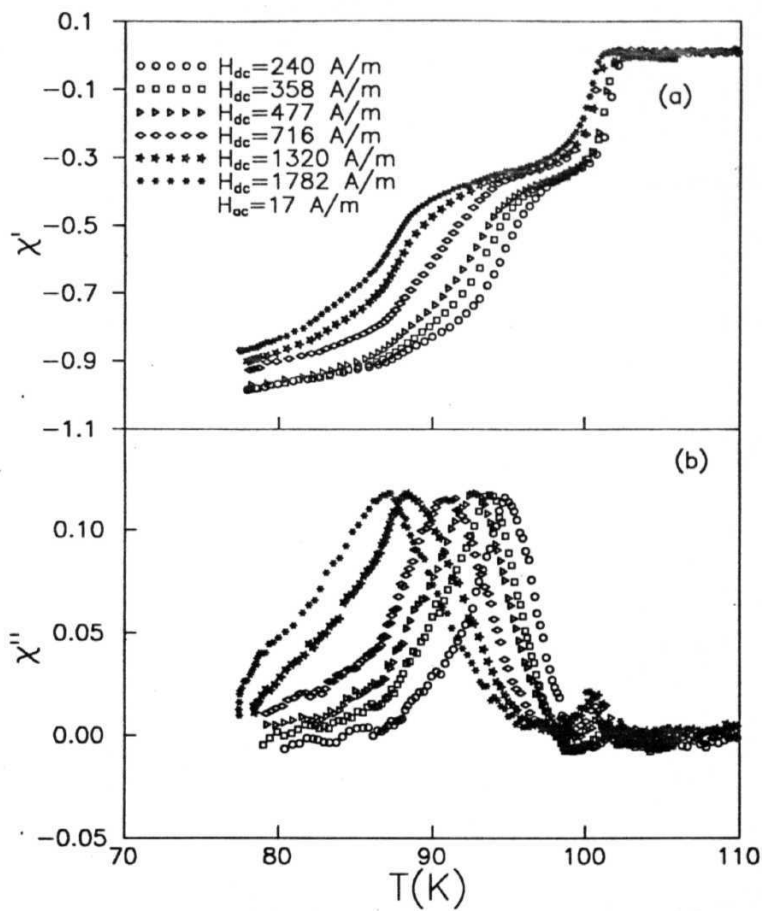


Fig. 4.20 Temperature dependence of measured fundamental susceptibility, (a) χ' and (b) χ'' of the BSCCO slab for different dc fields (H_{dc}), with $H_{ac} = 17$ A/m.

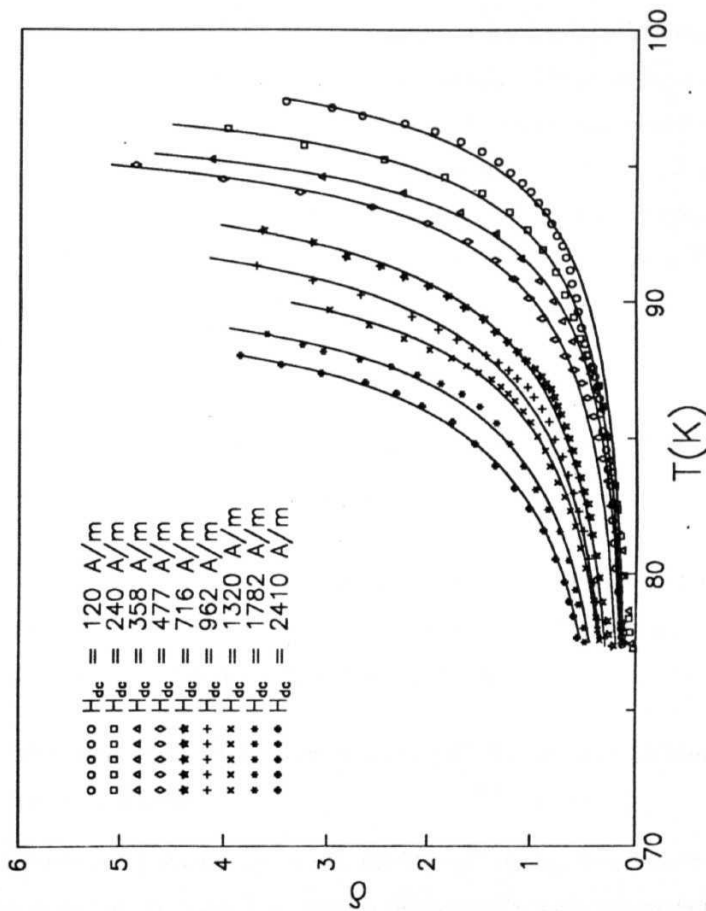


Fig. 4.21 Temperature dependence of $\delta(T, H_{dc})H_{ac}$ extracted from $\chi_m(T)$ data, derived using measured susceptibility shown in Fig. 4.20 for various dc fields, is shown as discrete points. Theoretical fits of the δ to Eq. (4.5.8) are shown as lines.

4.5.3 Field variation of ac susceptibility in melt textured NdBCO superconductor

The fundamental ac susceptibility χ' , and χ'' are measured on Nd-40 melt textured sample as a function of dc field (H_{dc}) in the range 0 to as large as 10 KOe at fixed temperature 77 K and are shown as discrete points in Fig. 4.22. Even though the applied maximum dc field is 10 KOe, we could not see the complete ac loss peak (χ'') in the sample, since the flux has not yet penetrated the sample completely. The grain fraction in the melt textured sample can be considered as 1, since weaklinks are suppressed in the sample. The theoretical susceptibility calculated from the Kim's critical state model, is shown as solid lines and is found to agree well with the experimental data. $\delta(H_{dc}, H_{ac})_T$ values are determined from the experimental χ , and are shown in Fig. 4.23 as discrete points. Field dependence of δ is found to be described well by,

$$\delta = 2H_{dc}H_{ac}/H_p^2 \quad (4.5.9)$$

derived based on Kim's model for small ac fields superimposed on large dc fields. The full penetration field H_p is obtained as 2.2×10^5 A/m.

The universal curve is then obtained by plotting the measured $\chi(H_{dc}, H_{ac})_T$ as a function of δ (determined from the fit parameter using the above equation) and is shown in Fig. 4.24, as the four curves with different ac fields.

4.5.4 Temperature variation of ac susceptibility in melt textured NdBCO superconductor

The temperature dependence of ac susceptibility $\chi(T, H_{dc})_{H_{ac}}$ was measured in the temperature range from 77 to 100 K. A small ac field at 33 Hz and a high dc field were chosen to be applied such that $H_{ac} \ll H_{dc}$ for the flux profile in the slab to be linear. $\chi'(T)$,

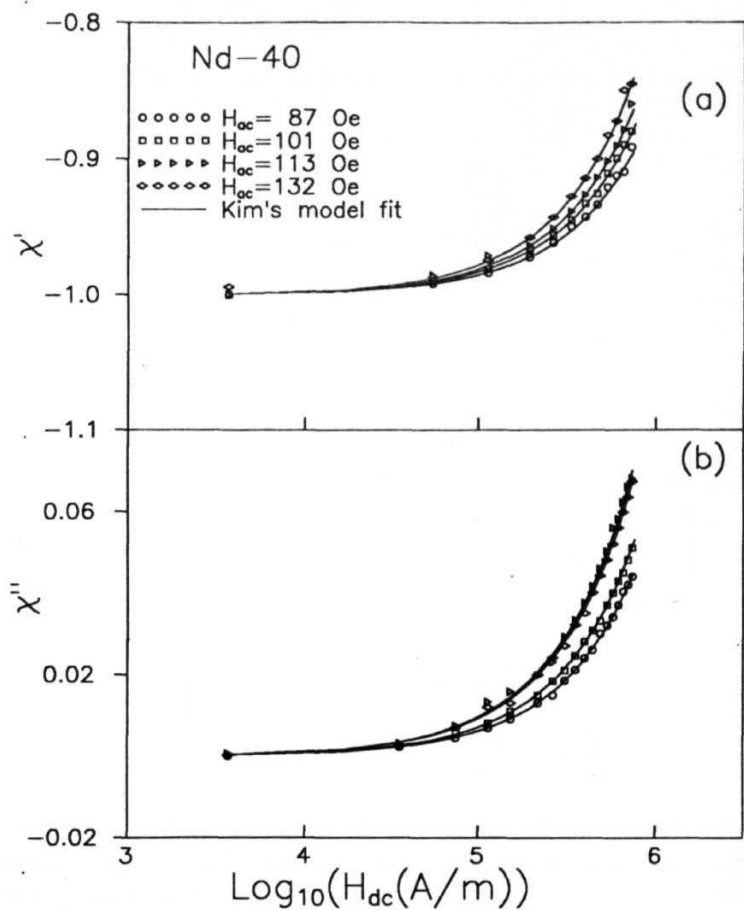


Fig. 4.22 The dc field dependence of measured fundamental susceptibility, (a) χ' , and (b) χ'' of the melt textured Nd-40 slab for different ac fields (H_{ac}) at 77 K. Data points are experimental data and the solid lines are fits to Kim's critical state model.

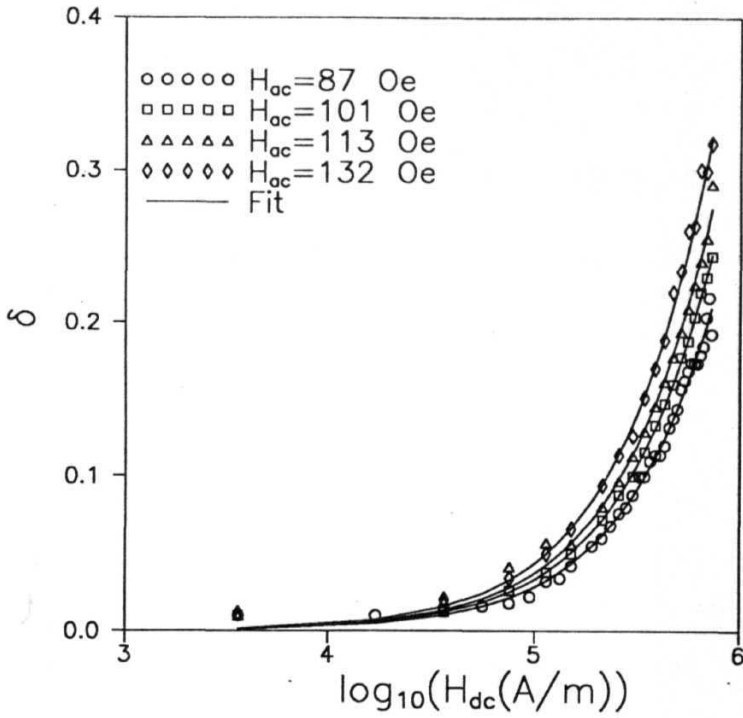


Fig. 4.23 Field dependence of b extracted from $\chi(H_{dc})$ data shown in Fig. 4.22 obtained at 77 K for various ac fields (discrete points). Theoretical fits of the b to Kim's model (Eq. (4.5.9)) are shown as lines.

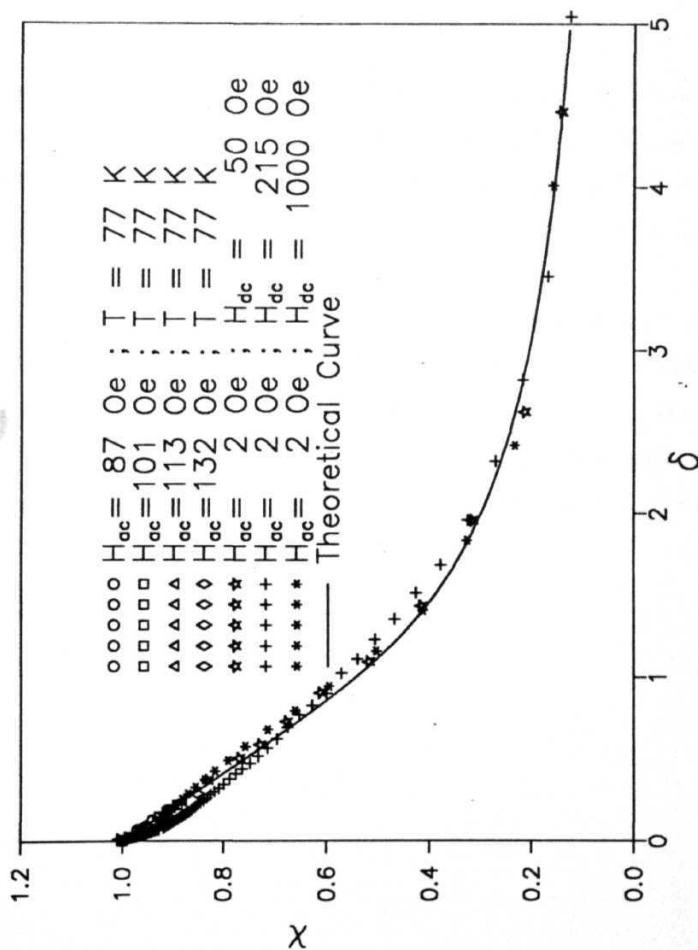


Fig. 4.24 A number of curves plotted for experimental χ as a function of δ , using both the measured field and temperature dependences of χ , are shown to demonstrate universality of fundamental susceptibility in melt textured NdBCO sample.

and $\chi''(T)$ measured at different dc fields and a constant ac field of 2 Oe are shown in Fig. 4.25. $\delta(T, H_{dc})$ is then determined using the Eqs. 4.5.1-4.5.4. Figure; 4.20 shows the T dependence of f_i at different H_{dc} as discrete points. Kim's model is chosen to define the relationship between J_c and H_{dc} . The variation of H_p with T is assumed to be $H_p(T) = H(0)((1 - (T/T_c)^2)(1 - (T/T_i)^2)^4)$. Strong field dependence of δ on T suggests that $b(T)$ can be expressed as

$$\delta(T) = P.I((1 - (T/T_c)^2)(1 - (T/T_i)^2)^4) \quad (4.5.10)$$

Using the values of the best fit for P_0 and T_i , the corresponding theoretical curves of $S(T)$ calculated from the above Eqn. 4.5.10 are shown as solid lines. The universal curve is then obtained by plotting the measured $\chi(T, H_{dc})_{H_{ac}}$ against the $\delta(T)$ determined from the fit parameters and is shown in Fig. 4.24 as the curves for different H_{dc} .

Thus the universal behaviour of ac susceptibility could be demonstrated well in sintered BSCCO as well as melt textured NdBCO samples, which are widely different in their properties. Since the magnitude of bulk critical current density is different by two orders of magnitude, correspondingly the ac susceptibility measurements were chosen to be conducted under different dc field ranges like 0 to 80 Oe for BSCCO with low J_c , and 0 to 10 KOe for melt textured NdBCO with large J_c .

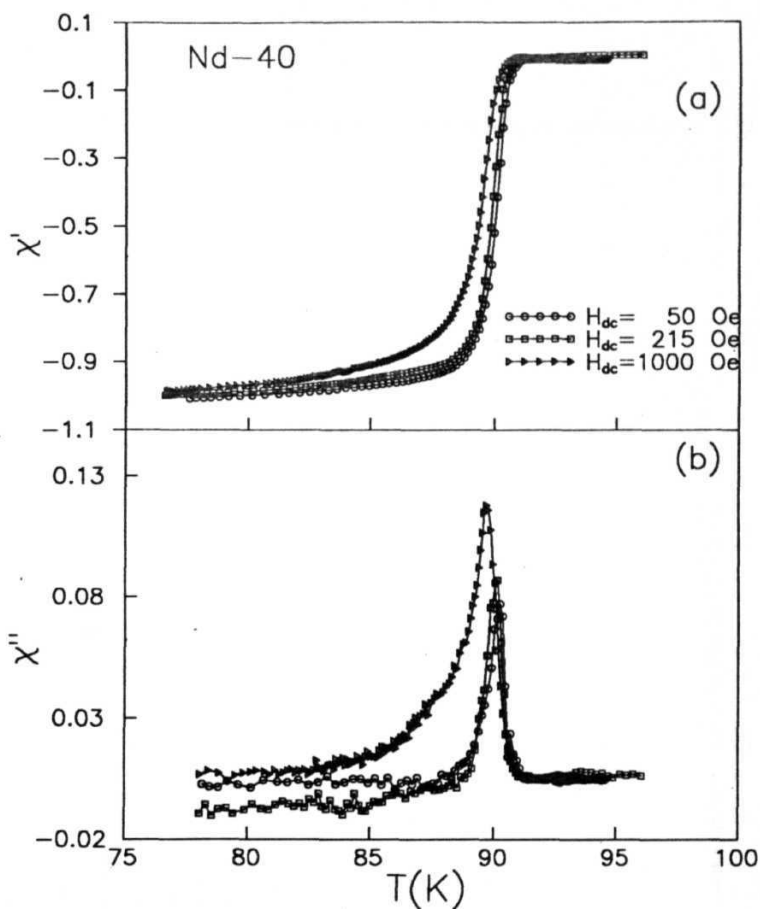


Fig. 4.25 Temperature dependence of measured fundamental susceptibility, (a) χ' and (b) χ'' of the NdBCO slab for different dc fields (H_{dc}), with $H_{ac} = 2$ Oe.

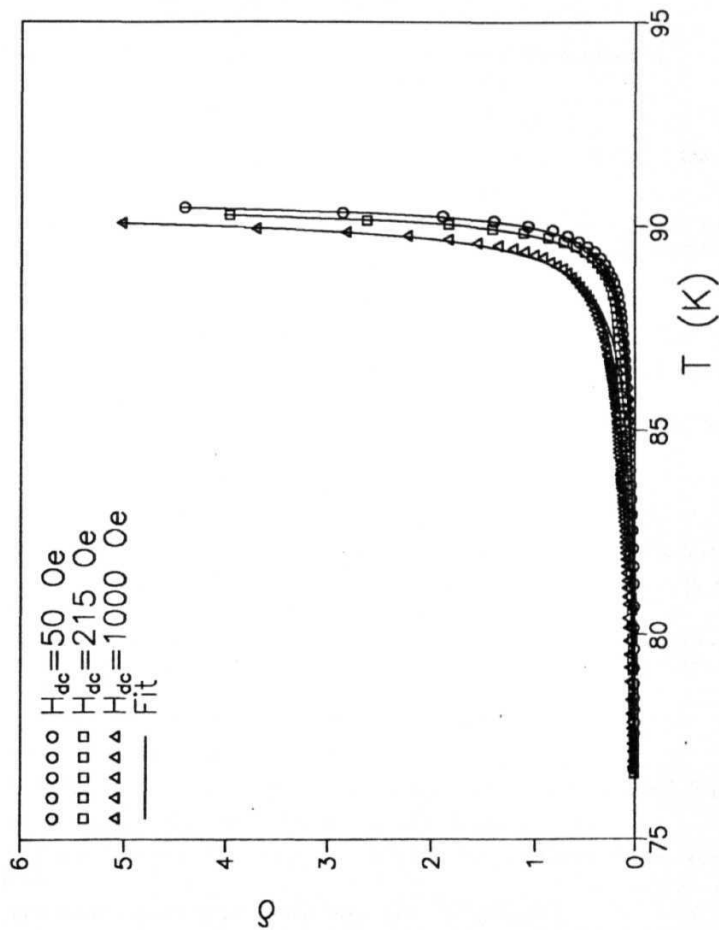


Fig. 4.26 Temperature dependence of $\delta(T, H_{dc})/H_{ac}$ extracted from $\chi(T)$ data, derived using measured susceptibility shown in Fig. 4.25 for various dc fields, is shown as discrete points. Theoretical fits of the δ to Eqn. (4.5.10) are shown as lines.

References

- [1] E. Maxwell and M. Strongin, *Phys. Rev. Lett.*, 10, 212 (1963).
- [2] T. Ishida and H. Mazaki *Phys. Rev. B*, 20, 131 (1979).
- [3] A. F. Khoder, *Phys. Lett.*, **94A**, 378 (1983)
- [4] R. A. Hein, *Phys. Rev. B.*, **33**, 7539 (1986).
- [5] T. Ishida and H. Mazaki, *J. Appl. Phys.*, 52, 6798 (1981).
T. Ishida and H. Mazaki, *Phys. Lett.*, **87A**, 373 (1982).
- [6] Y. Kim, Q. Harry Lam and C. D. Jfferies, *Phys. Rev. B* 43, 11404 (1991).
- [6] M. Nikolo and R. B. Goldfarb, *Phys. Rev. B* **39**, 6615 (1988).
- [7] D. X. Chen, J. Nogues and K. V. Rao, *Cryogenics* 29, 800 (1989).
- [8] D. X. Chen, A. Sanchez, T. Puig, L. M. Martinez, and J. S. Munoz, *Physica C* 168, 652 (1990).
- [9] T. Ishida and R. B. Goldfarb, *Phys. Rev. B* 41, 8939 (1990).
- [10] L. Civale, T. K. Worthington, L. Krusin-Elbaum and F. Holtzberg, in *Magnetic Susceptibility of Superconductors and Other Spin Systems*, edited by R. A. Hein, T.L.Francavilla, and D. H. Liebenberg (Plenum, New York, 1992).
- [11] Y. Kim, Q. Harry Lam and C. D. Jfferies, *Phys. Rev. B* 43, 11404 (1991).
- [12] O. F. Schilling, K. Aihora, A. Soeta, T. Kamo and S. Matsuda, *Phys. Rev. B* 47, 8096 (1993).
- [13] D. Berling, E. V. Antipov, J. J. Capponi, M. F. Gorius, B. Loegel, A. Mehdaoui and J. L. Tholence, *Physica C* **225**, 212 (1994).
- [14] X. C. Jin, Y. Y. Xue, Z. J. Huang, J. Bechtold, P. H. Hor and C. W. Chu, *Phys. Rev. B* **47**, 6082 (1993).
- [15] M. G. Karkut, M. Slaski, L. K. Sagdahl, and K. Fossheim, *Physica C* 215, 19 (1993).
- [16] R. B. Goldfarb, A. F. Clark, A. I. Braginski and A. J. Panson, *Cryogenics* 25 695 (1985).
- [17] D. X. Chen, R. B. Goldfarb, J. Nogues and K. V. Rao, *J. Appl. Phys.* 63 980 (1988).
- [18] D. C Larbarestier, S. E. Babcock, X. Cai, M. Daeumling, D P. Hampshire, T. F. Kelly, L. A. Lavanier, P.J. Lee and J. Seuntjens, *Physica C* 153-155 1580 (1988).
- [19] R. B. Goldfarb, M. Lelental, and C. A. Thomson, in *Magnetic Susceptibility of Superconductors and Other Spin Systems*, edited by R. A. Hein, T.L.Francavilla, and D. H. Liebenberg (Plenum, New York, 1992).
- [20] K. H. Miiller, *Physica C*, **159** 717 (1989).
- [21] J. R. Clem, *Physica C* 153-155, 50 (1988).
- [22] K. H. Muller, B. W. Ricketts, J. C. MacFarlane and R. Driver, *Physica C* **162**, 1177 (1989).
- [23] D. H. Wu and S. Sridhar, *Phys. Rev. Lett.* 65 2074 (1990).
- [24] S. L. Shinde, J. Morrill, D. Goland, D. A. Chance, and T. McGuire, *Phys. Rev. B*, 41, 8838 (1990).
- [25] V. Ambegaokar and A. Baratoff, *Phys. Rev. Lett.* 10, 486 (1963).
- [26] R. Gopalan, T. Roy, T. Rajasekharan, G. Rangarajan and N. Hari Babu, *Physica C* **244**, 106 (1994).

- [27] **M. Couach, A. F. Khoder, F. Monnier, B. Barbara and J. Y. Henry**, *Phys. Rev. B* **38**, 748 (1988).
- [28] **C. P. Bean**, *Phys. Rev. Lett.* **8**, 250 (1962); *Rev. Mod. Phys.* **36**, 31 (1964).
- [29] **F. Sumiyoshi, M. Matsuyama, M. Noda, T. Matsushita, K. Funaki, M. Iwakuma and K. Yamafuji**, *Jpn. J. Appl. Phys.* **25**, L148 (1986).
- [30] **A. M. Campbell**, *J. Phys. C* **4**, 3186 (1971).
- [31] **T. Matsushita, E. S. Otabe and B. Ni**, *Physica C* **182**, 95 (1991).
- [32] **J. R. Clem** in *Magnetic Susceptibility of Superconductors and Other Spin Systems*, edited by **R. A. Hein, T. L. Francavilla, and D. H. Liebenberg** (Plenum, New York, 1992).
- [33] **Y. B. Kim, C. F. Hempstead, and A. R. Strnad**, *Phys. Rev. Lett.* **9**, 306 (1962).
- [34] **Y. B. Kim, C. F. Hempstead and A. R. Strnad**, *Phys. Rev.* **129**, 528 (1963).
- [35] **G. Ravi Kumar and P. Chaddah**, *Phys. Rev. B* **39**, 4704 (1989).
- [36] **D. X. Chen, J. Nogues, and K. V. Rao**, *Cryogenics* **29**, 800 (1989).
- [37] **D. X. Chen, Yu Mei and H. L. Luo**, *Physica C* **167**, 317 (1990).
- [38] **D. X. Chen, A. Sanchez, T. Puig, L. M. Martinez and J. S. Muñoz**, *Physica C* **168**, 652 (1990).
- [39] **S. Ravi and V. Seshu Bai**, *Phys. Rev. B* **49**, 13 082 (1994).
- [40] **S. Ravi and V. Seshu Bai**, *Physica C* **230**, 51 (1994).
- [41] **T. Ishida and R. B. Goldfarb**, *Phys. Rev. B* **41**, 8937 (1990).
- [42] **L. Ji, R. H. Sohn, G. C. Splaingard, C. J. Lobb and M. Tinkham**, *Phys. Rev. B* **40**, 10 936 (1989).
- [43] **Youngtae Kim, Q. Harry Lam, and C. D. Jeffries**, *Phys. Rev. B* **43**, 11 404 (1991).
- [44] **Q. H. Lam, Y. Kim, and C. D. Jeffries**, *Phys. Rev. B* **42**, 4846 (1990).
- [45] **Y. Yamaguchi, D. H. HA, F. Iga, and Y. Nishihara**, *Physica C* **228**, 141 (1994).
- [46] **S. Shatz, A. Shaulov, and Y. Yeshurun**, *Phys. Rev. B* **48**, 13 871 (1993).
- [47] **A. M. Campbell**, *J. Phys. C* **2**, 1492 (1969).
- [48] **A. M. Campbell**, in *Magnetic Susceptibility of Superconductors and Other Spin Systems*, edited by **R. A. Hein, T. L. Francavilla, and D. H. Liebenberg** (Plenum, New York, 1992).
- [49] **John R. Clem and Zhidong Hao**, *Phys. Rev. B* **48**, 13 774 (1993).
- [50] **M. Tinkham**, *Phys. Rev. Lett.* **61**, No. 14, 1658 (1988).

Chapter 5

Magnetic flux profiles

5.1 Introduction

As discussed in Chapter 4, the contributions from the intergranular and intragranular regions of high temperature superconductors (HTSCs) have been studied well by ac magnetic susceptibility measurements [1-12]. The corresponding critical current densities J_{ci} and J_{cg} have been analyzed using critical state models [13-16]. In the intergranular region, the nature and density of weak links associated with the coupling between the grains can be drastically modified by melt texturing the HTSCs as discussed in Chapter 3. However, a clear correlation is yet to be established between the microstructures of HTSCs and their physical properties sensitive to the presence of weak links. In an attempt to contribute in this direction, magnetic flux profiles of $Bi_{1.2}Pb_{0.3}Sr_{1.5}Ca_2Cu_3O_y$ and $NdBa_2Cu_3O_{7-\delta}$ superconductors with widely different and systematically characterized microstructures has been taken up for a detailed study. Campbell [17] suggested a sensitive and versatile method that uses a phase sensitive detector to measure the flux distribution which in turn helps to determine model independent J_c in type - II superconductors. This method can be used to assess the J_c of a material in a dc field regime that is not accessible to transport methods due to the limitations on the maximum current that can be sent through the electrical contacts [18]. Ni *et al.* [19] used this method to measure J_{ci} and J_{cg} for a sintered $YBa_2Cu_3O_{7-\delta}$ superconductor at 77 K while Dang *et al.* [20] have determined J_{cg} and the pinning strength of $Bi_{1.7}Pb_{0.3}Sr_2Ca_2Cu_3O_y$.

Küpfer *et al.* [21] have determined from the flux profiles the **pinning** parameters like J_c , reversible **penetration** depth λ'_c of a pinned flux **lattice**, and the reversible displacement d , which is the distance flux can move before being **unpinned** and comparison has been made between low T_c superconductors and $\text{YBa}_2\text{Cu}_3\text{O}_{7-\delta}$.

In this chapter, the features of flux profiles measured for the sintered and press sintered $\text{Bi}_{1.2}\text{Pb}_{0.3}\text{Sr}_{1.5}\text{Ca}_2\text{Cu}_3\text{O}_y$ (BSCCO) have been studied. Also, sintered, and melt textured $\text{NdBa}_2\text{Cu}_3\text{O}_{7-\delta}$ (NdBCO) superconductor with systematically varying Nd-422 content, have been examined. The theoretical model calculations of the observed magnetic flux profiles have been carried out towards the end of this chapter. An attempt is made to correlate the observed flux profiles to the microstructural features of the sintered and melt textured samples. The J_c values obtained using the flux profiles study on the samples have been compared with those obtained using a SQUID magnetometer. The flux profile technique offers some advantages due to the fact that large samples with well characterized weak links can be studied, and the behaviour of such weak links, for instance, as a function of applied magnetic fields, can be obtained. Such a possibility is demonstrated by the study of domain coupling strength in melt processed NdBCO. Also, since the data obtained using the flux profile technique are on larger samples unlike that obtained using a SQUID magnetometer, the former can be more relevant from a practical view point.

5.2 Experimental

Sample details

One set of samples used in the present study are sintered $\text{Bi}_{1.2}\text{Pb}_{0.3}\text{Sr}_{1.5}\text{Ca}_2\text{Cu}_3\text{O}_y$, and press-sintered $\text{Bi}_{1.2}\text{Pb}_{0.3}\text{Sr}_{1.5}\text{Ca}_2\text{Cu}_3\text{O}_y$. The composition $\text{Bi}_{1.2}\text{Pb}_{0.3}\text{Sr}_{1.5}\text{Ca}_2\text{Cu}_3\text{O}_y$ has been demonstrated to yield single phase Bi-2223 superconductor [22]. They have been prepared from citrate precursors and the exact details of sample preparation, X-ray diffraction (XRD), and the microstructural studies can be found in Refs. 22 and 7. The press-sintered sample was one that had been subjected to a further cold pressing and sintering, after the first sintering step. It has been reported that such a processing route induces texture in the sample and improves density, grain connectivity and J_c [22,23]. The zero resistivity temperatures are 106.4 K and 105.9 K respectively. The XRD results showed texturing along the c-axis of the unit cell in the press sintered BSCCO sample. Scanning electron micrographs (SEM) of the fractured surface showed sintered BSCCO to be highly porous while the porosity had reduced on press sintering. The average size of the grains which is $\sim 5 \mu\text{m}$ in sintered BSCCO was reduced to $\sim 1 \mu\text{m}$ in the press-sintered sample. The porosity was determined to be 50% and 15% for the sintered and press-sintered BSCCO respectively.

The second set of samples studied using the flux profile measurement technique were sintered NdBCO and melt textured NdBCO with systematically varied $\text{Nd}_4\text{Ba}_2\text{Cu}_2\text{O}_{10}$ phase content. Preparation of sintered $\text{NdBa}_2\text{Cu}_3\text{O}_{7-\delta}$ (NdBCO) has been described in Chapter 3. Closely packed grains of size $\sim 15 \mu\text{m}$ can be seen in an optical micrograph of the sample (Fig. 3.5). Porosity was estimated to be $< 5\%$. Transition to zero resistivity occurred at 91 K. The diamagnetic transition was broad (Fig. 4.1(a)) and details were presented in section 4.2.

The melt processing of the NdBCO samples and their microstructural details have been discussed in Chapter 3. As discussed therein, all the samples processed at 1 °C/h cooling rate through the peritectic temperature, are found to consist of domains of size 7-8 mm² without any liquid phase segregation at the boundaries. The domains are observed to contain Nd-123 platelets separated by gaps with fine uniformly distributed Nd₄Ba₂Cu₂O₁₀ (Nd-422) inclusions. For all the samples, zero resistivity temperature was around 92 K with the transition width of less than 1 K. The temperature variation of ac susceptibility shows that the diamagnetic transitions in the samples are very sharp (Fig. 4.4) confirming the suppression of low T_c solid solution phase.

The Nd-40 samples processed at various cooling rates have similar microstructural features. In the faster cooled samples, some of the domain boundaries had unreacted liquid phases.

Magnetic flux profile measurements

The details of the experimental facility used to record the magnetic flux penetration into the superconducting samples, and its calibration so as to obtain the penetration depth from the measured lock-in voltages have been given in Chapter 2. The magnitude of the applied ac field H_{ac} as a function of $p/7$? ($= (1 - \sqrt{\frac{-1}{K} \frac{dS}{dH_{ac}}})$) is known as magnetic "flux profile". The slope of the flux profile i.e, the flux gradient ($d(H_{ac})/d(p/R)/R$) gives the critical current density.

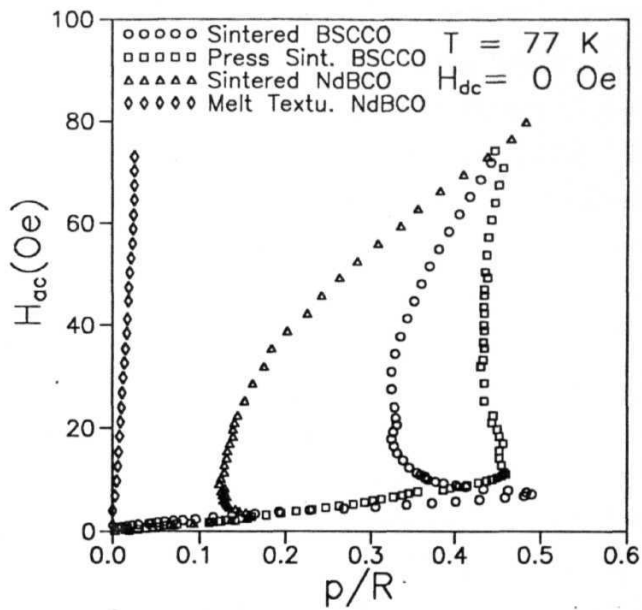


Fig. 5.1 Magnetic flux profiles (H_{ac} versus p/R) for sintered BSCCO, press sintered BSCCO, sintered NdBCO and melt textured NdBCO in the absence of dc field.

5.3 Magnetic flux profiles in poly crystalline superconductors : BSCCO and NdBCO

5.3.1 Profiles with $H_{dc} = 0$

The magnetic flux profiles measured at 77 K in four HTSC samples with no external dc field are shown in Fig. 5.1. They are the sintered BSCCO sample, the press-sintered BSCCO, sintered NdBCO sample and a melt processed NdBCO sample. In the case of sintered BSCCO sample, the normalized penetration depth (p/R) increases nonlinearly with field and shows a peak like structure at 8 Oe, which is the field (H_i^*) at which full penetration of flux takes place into the intergranular region. Non-linearity is an indication of field dependence of J_c . The penetration remains constant between 10 Oe and 30 Oe, the lower critical field of the grains (H_{c1g}). Initially the flux starts penetrating the sample from surface to the center through the intergranular region while the grains remain in Meissner state, since the grain critical current density is much larger than the intergranular current density, However, the shielding currents now flow inside the grains upto a depth of the order of London penetration depth (λ_L). If the penetrated field crosses H_{c1g} , the field starts penetrating into the grains individually in the form of Abrikosov vortices. The two distinct slopes of the flux profile clearly provide evidence for the granular nature of this sample with two distinct J_c s for the intergranular and the intragrain regions. Koblishka *et al.* [24] studied the magnetic flux penetration in granular $YBa_2Cu_3O_{7-\delta}$ samples by using High-Resolution Faraday effect (HRF). They found that the flux penetration occurred in stepwise manner, i.e, flux first penetrated into intergranular region and when the field is above H_{c1g} it entered into individual grains. For a granular sample, the effective permeability (μ_c) is given by $(1 - f_g)\mu_o + f_g\mu_g$, where μ_o and μ_g are intergrain and intragrain permeabilities respectively and f_g is the grain fraction. If the grains are in perfect Meissner state, $\mu_c = (1 - f_g)\mu_o$. At full penetration

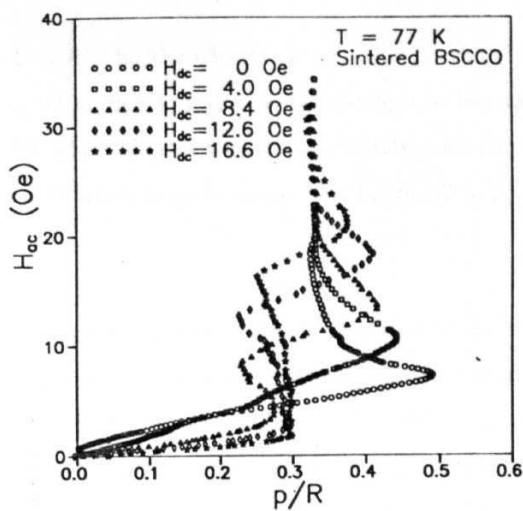


Fig. 5.2 Flux profiles in sintered $\text{Bi}_{1.2}\text{Pb}_{0.3}\text{Sr}_{1.5}\text{Ca}_2\text{Cu}_3\text{O}_y$ at various dc fields, at 77 K.

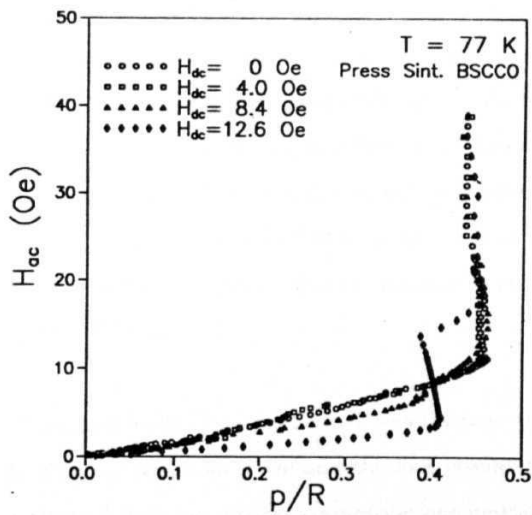


Fig. 5.3 Flux profiles in press sintered $\text{Bi}_{1.2}\text{Pb}_{0.3}\text{Sr}_{1.5}\text{Ca}_2\text{Cu}_3\text{O}_y$ at various dc fields, at 77 K.

(p^*), $d\phi/dH_{ac}$ vs $2\pi\mu_c R^2$. So the effective p^*/R value is related to the grain fraction through $f_g = (1 - p^*/li)^2$. In Fig. 5.1, a vertical asymptotic line appears at $p^*/R = 0.33$ for sintered BSCCO. This indicates a full flux penetration for about $H_{ac} = 8$ Or and f_g is estimated to be 0.45 which is quite comparable to the 50 % porosity observed in the microstructure.

The flux profile in press-sintered sample is nearly linear at low fields, suggesting a weaker field dependence of J_c . The peak like structure is less pronounced and the penetration remains constant up to the maximum field applied (80 Oe), suggesting $H_{c1g} > 80$ Oe. Full penetration for intergranular region occurred at 11 Oe and the vertical asymptotic line appears at $p^*/R = 0.41$, giving a value of 0.35 for f_g . Though the microstructure shows only 15 % porosity (suggesting $f_g = 0.85$) and this discrepancy has its origin in the fact that the increased effective volume of the intergranular region into which flux penetrates has increased as a result of the smaller size ($\sim 1 \mu m$) of the grains on press sintering, compared to sintered sample with grains of $5 \mu m$. The enhancement in the apparent lower critical field H_{c1g} value on press sintering is probably due to the existence of surface barrier to the penetration of magnetic flux. According to Bean-Livingston [25] theory a plane surface of a type - II superconductor will produce a nucleation barrier that will increase the initial flux penetration field to near the thermodynamic critical field H_c , and roughening of the surface will permit flux penetration near the superconducting to mixed-state transition field H_{c1} .

In the case of sintered NdBCO, magnetic flux penetrates to the center of the sample through the intergranular region for 4 Oe and the flux profile is nonlinear. The value of f_g is 0.8, as estimated from the vertical asymptotic line indicating full penetration at $p^*/R = 0.11$. This is consistent with the volume fraction of the grain region, estimated

from the optical **micrographs, which** showed that 85 % of the sample is occupied by the grains of nearly **equal size** ($\sim 15 \mu\text{m}$) **separated by relatively smaller interface regions.**

As can be seen from Fig. 5.1, the extent of flux penetration into a melt processed sample has enormously reduced. The detailed study of flux penetration into various melt grown samples is presented in section 5.4.

5.3.2 Profiles with ($H_{dc} \neq 0$)

Figures 5.2 and 5.3 show the flux profiles recorded in the presence of a constant dc field superimposed on the ac field in sintered and press-sintered BSCCO samples. In the case of sintered sample, flux profile has become linear at low ac fields in the presence of dc fields. Slope of the linear regions gets reduced with increasing dc field. When H_{ac} is comparable to H_{dc} , an oscillatory behavior is seen in the flux profiles. In the case of the press sintered sample also a similar behavior is seen, but the amplitude of oscillation is less. The reason for oscillatory behavior is that due to subtraction of ac from dc, the magnetic field at some local regions inside the sample becomes zero. There the screening would be better than in zero H_{dc} , and hence the current density is effectively higher.

Slope near the origin in the linear regime is related to the critical current density J_{ci} , as given by

$$J_{ci} = \frac{dH_{ac}}{d(p/R)} \frac{1 - f_g}{R} \quad (5.3.1)$$

J_{ci} is calculated at various dc fields and is shown in Fig. 5.4. For sintered BSCCO, J_{ci} falls abruptly with H_{dc} . J_{ci} is enhanced on press sintering but its field dependence is weaker. J_{ci} varies as $J_{ci}(H_{dc}) = K/(H_{dc} + H_o)$ for both the samples with fit parameters $K = 3.58 \times 10^8 \text{ A}^2/\text{m}^3$, $H_o = 450 \text{ A/m}$ for sintered BSCCO and $K = 4.67 \times 10^9 \text{ A}^2/\text{m}^3$,

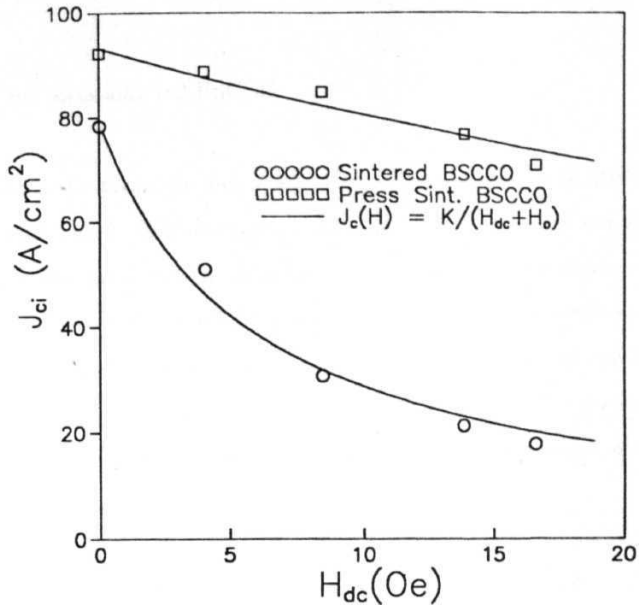


Fig. 5.4 Field variation of inter granular J_{ci} determined from the linear regime of flux profiles for sintered BSCCO and press sintered BSCCO. Solid line is a fit to the equation $J_{ci} = \frac{K}{H_{dc} + H_0}$.

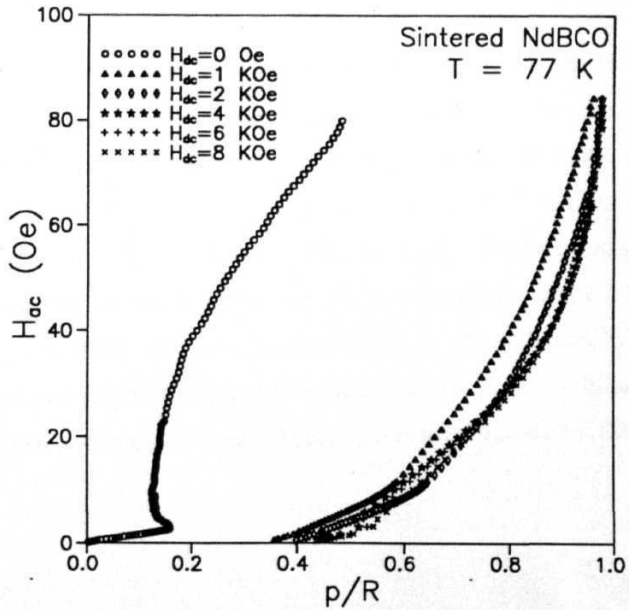


Fig. 5.5 Flux profiles in sintered $NdBa_2Cu_3O_{7-\delta}$ at various dc fields, at 77 K

H_o - 5010 A/m for press sintered BSCCO.

Figure 5.5 shows the magnetic flux penetration into the sintered NdBCO sample in the presence of different dc field strengths. The magnetic flux profile has shifted from the origin in the presence of external dc fields. The normalized penetration (p/R) has reached a value of 1 when $H_{dc} = 1$ KOe indicating that full flux penetration has taken place into the sample including the grains. Reduction in the slope of the flux profiles at still higher fields indicates a strong field dependence of J_{cg} of the grains. This was observed as a shift in the position of the intragranular loss peak (Fig. 4.1b) with an increase in the ac field amplitude.

5.4 Magnetic flux profiles in melt textured NdBCO samples

5.4.1 Slow cooled samples

The magnetic flux profiles measured in melt textured stoichiometric Nd-123 (Nd-0) are shown in Fig. 5.6. Flux penetration (p/R) nearly linear with H_{ac} , unlike in the case of sintered samples where the profile is non-linear with nose-like structure appearing at $H_{ac} \sim H_{pi}$ and an oscillatory behavior is seen when $H_{ac} \sim H_{dc}$. As the external dc field is increased, the extent of ac field penetration (p/R) increases. The normalized penetration (p/R) has reached 0.5 for the maximum applied field of 10 KOe. In the case of Nd-123 samples with Nd-422 inclusions (Fig. 5.7, 5.8, 5.9 and 5.10), the extent of flux penetration is lower than the stoichiometric (Nd-0) sample. The flux that penetrates the superconductor in the form of Abrikosov vortices gets pinned at certain defects (pinning centers) if they are of the order of coherence length ξ . Even though Nd-422 particles cannot contribute directly to flux pinning because their size ($\sim 1 \mu m$) is large when compared to the coherence length (~ 3 nm), the structural defects around a 123/422 interface

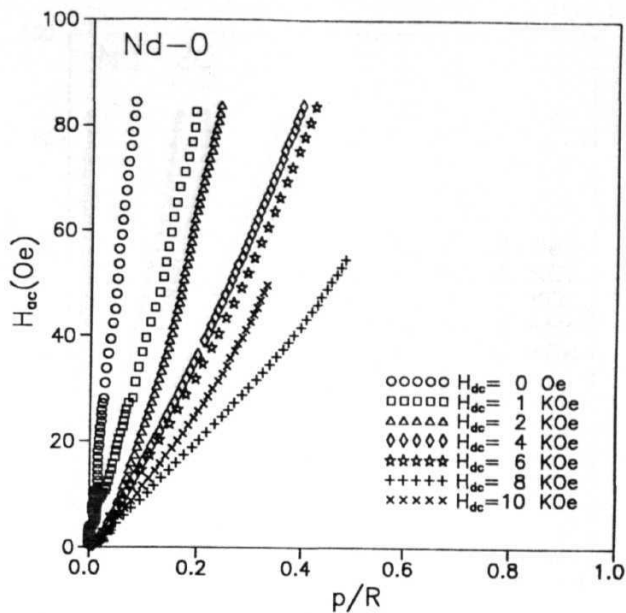


Fig. 5.6 Flux profiles in melt textured Nd-0 superconductor at 77 K.

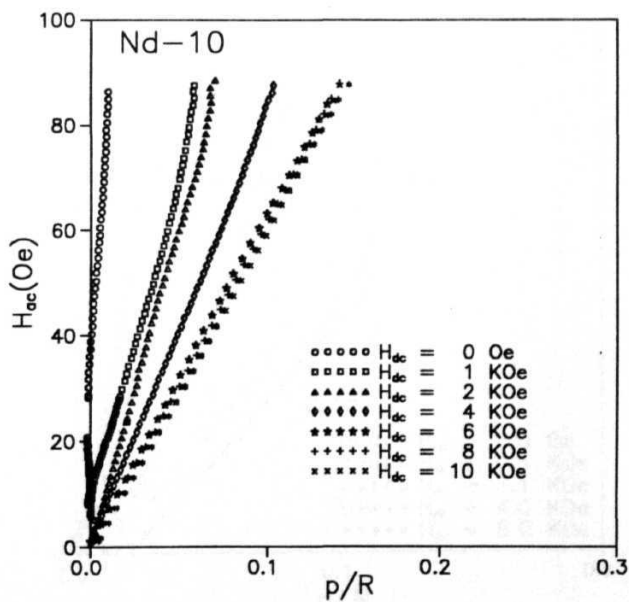


Fig. 5.7 Flux profiles in melt textured Nd-10 superconductor at 77 K.

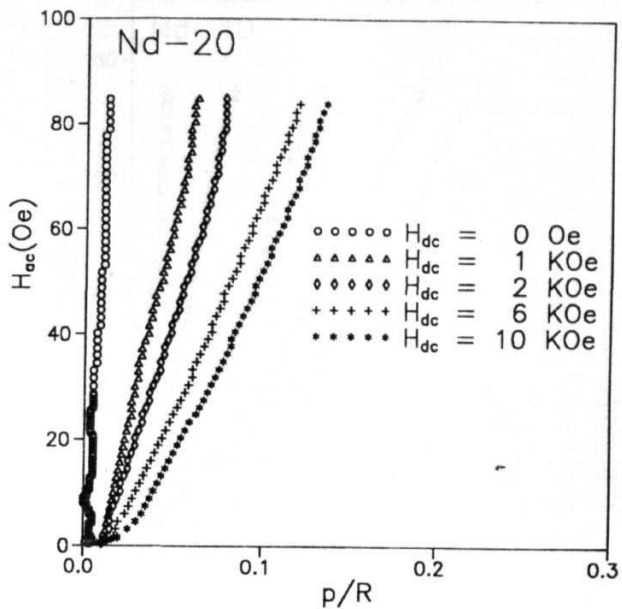


Fig. 5.8 Flux profiles in melt textured Nd-20 superconductor at 77 K.

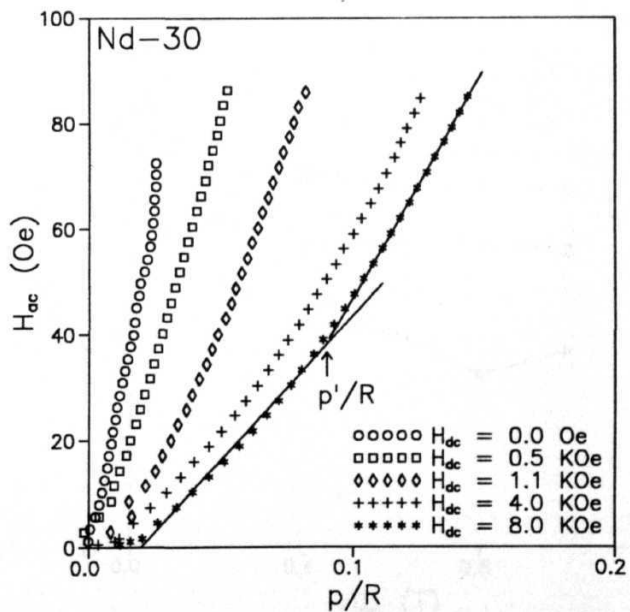


Fig. 5.9 Flux profiles in melt textured Nd-30 superconductor at 77 K.

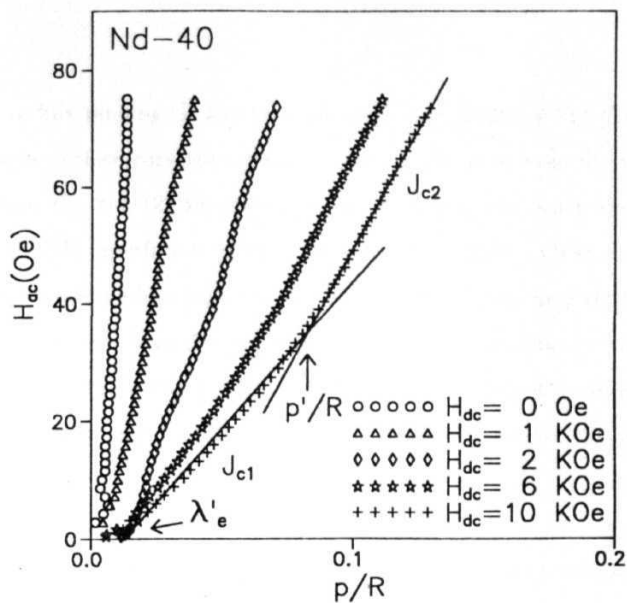


Fig. 5.10 Flux profiles in melt textured Nd-40 superconductor at 77 K.

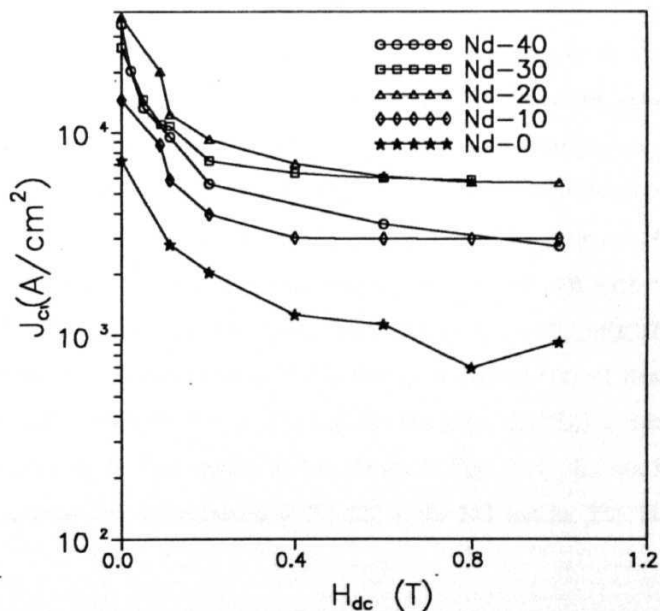


Fig. 5.11 Bulk critical current density J_{c1} , determined from the initial slope of the flux profiles.

would contribute to flux pinning. It has been observed that [27,28] Y-211 (Y_2BaCuO_5) particles with a large surface curvature are associated locally with a density of stacking faults in Y-123, near the 211/123 interfaces. These defects appear when the radius of curvature of the 123/211 interface is below a certain value [27,28]. Calculations made using simple energy considerations suggest that these stacking faults may act as effective pinning centers for magnetic fields directed both parallel and perpendicular to the basal plane [29]. The small extent of flux penetration in Nd-422 added melt textured samples can be attributed to the presence of fine and uniformly distributed Nd-422 particles in the Nd-123 matrix.

The second slope of the flux profile at high dc fields corresponds to a distinctly different critical current density of the platelets. From the microstructural features of a melt processed sample, the first slope can be associated with the flux penetration into the specimen through the gaps, where the current J_{c1} flows across the interplatelet gaps while the second slope corresponds to the flux entry into the platelets. This picture is supported by the high-resolution Farady measurements of Schuster *et al.* [30] on melt processed $\text{YBa}_2\text{Cu}_3\text{O}_y$. They find that the flux penetrates (Fig. 2c and 2d in Ref. 30) the sample preferentially along the cracks to start with and then into the matrix. Although this penetration is not uniform in the microscopic scale, it can be considered to be fairly uniform in the macroscopic scale, since the density of gaps are approximately uniform throughout the specimen giving rise to the observed linearity of p/R with the H_{ac} at lower fields. The bulk critical current density obtained as $J_{c1} = dH_{ac}/d(p/R)/R\phi_m$ low ac field region can be considered to be the transport critical current density, since this slope is associated with the flux gradient across the gaps. $J_{c1}(H_{dc})$ is calculated by measuring the slope of the flux profiles and is shown in Fig. 5.11. J_{c1} can be seen to increase as we increase the concentration of Nd-422 in the 123 matrix. This is similar to

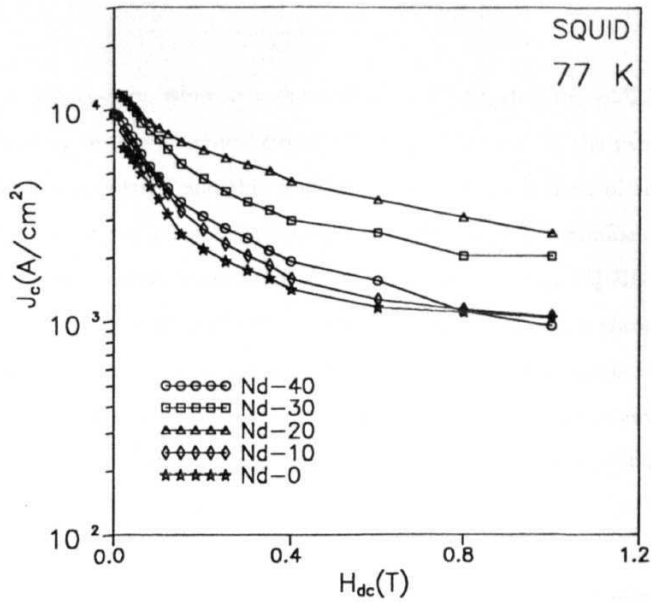


Fig. 5.12 Field variation of J_c determined from SQUID magnetization measurements

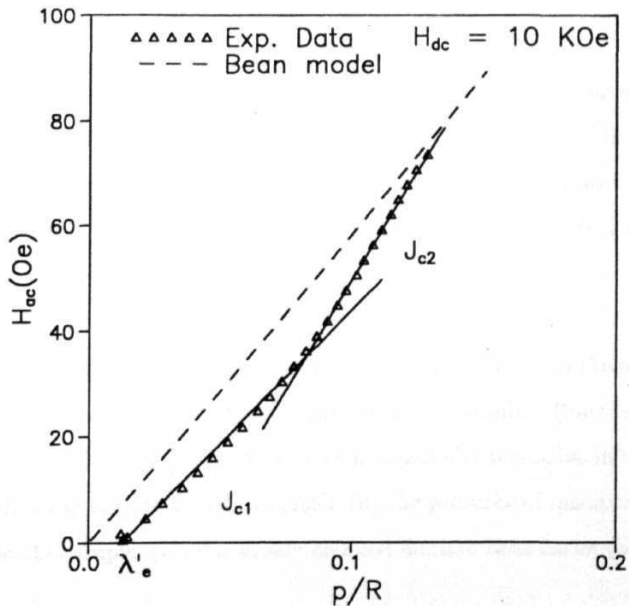


Fig. 5.13 Flux profile in a type-II irreversible superconductor as predicted by Bean's critical state model is shown as dashed line. The discrete points are experimental data exhibit two lines of slope J_{c1} and J_{c2} . The shift from the origin on the p/R axis represents the reversible Penetration depth.

the case of **Y-123** system, where it is demonstrated [31,32] that the addition of Y 211 to the Y-123 matrix improves critical current density. However, in the case of **Nd-40**, J_{c1} is found to have decreased and this could be due to the reduction of **superconducting** path through the dense **nonsuperconducting** Nd-422 particles. Similar variation of J_c with Nd-422 concentration is observed in the results obtained by SQUID magnetometer (see Chapter 6) on smaller specimens (nearly single domain) and is shown in Fig. 5.12. Even though the samples used for the study of flux penetration contained many domain boundaries, the agreement between these two measurement techniques suggests that, the boundaries are strongly coupled and are able to carry a critical current as high as that carried by an individual domain.

The grain (platelet) critical current density, J_{c2} is related to the second slope as $J_{c2} = 2dH_{ac}/d(p/R)/p_w$ where p_w is the platelet width and is tabulated for all the samples at 10 KOe field.

Based on the Bean critical state model, for homogeneously distributed pinning centers, flux profile should be linear, passing through the origin as shown in Fig. 5.13 by a dashed line. It is found that the measured flux profile has not started from the origin. The shift on the p/R axis represents the reversible penetration depth (λ'_c) which is an average of various regions of reversible flux motion.

The possible sources of reversible flux motion are associated with (i) the reversible penetration depth of a pinned vortex lattice λ'_c proposed by Campbell (Since no flux pinning potential well is infinitely sharp, the flux motion is actually reversible in the pinning potential well when the applied ac field is small), (ii) the presence of macrocracks in sample or big voids in the sample, (iii) the weakly coupled domain boundaries (as in the case of

sintered samples) or (iv) the large extent of the low- T_c phase like $Nd_{1-x}Ba_{2-x}Cu_3O_{7-\delta}$, if present.

The last possibility can be ruled out in the samples used for this study, because these showed a sharp diamagnetic transition around 92 K with a transition width < 1 K in the ac susceptibility measurements, representing the suppression of solid solution formation.

The region of reversible fluxoid motion at the domain boundaries in the melt textured sample can have similar characteristics as those of the grain boundaries in the sintered samples if the domain boundaries are isolated under high dc fields. In the presence of high external dc fields, the screening currents locally flow around the grains. In that situation, the ac field freely moves in and out of the sample along the grain boundaries without flux trapping. Due to this reversible fluxoid motion at the grain boundaries, the flux profile shifts from the origin along the p/R axis. The measured reversible penetration depth is $540 \mu\text{m}$. This is much greater than the Campbell's reversible penetration depth of a pinned vortex lattice [33] and is mostly due to the reversible fluxoid motion at normal regions at the grain boundaries. Melt textured samples used in this study contain many domain boundaries. These domain boundaries are clean and are free from liquid phases. Even though they are well connected, some high angle domain boundaries can act as weaklinks as in the case of randomly oriented grains in polycrystalline sample.

Table 1. Microstructural and pinning parameters

	C_w	P_w	$\langle \text{size} \rangle$	r_f	p'/R	λ'_c	λ'_c	J_{c2} (77K)
	μm	μm	μm			μm	μm	A/cm ²
Nd-0	0.70	10	6.0	0.163	0.250	24	20	2.5×10^5
Nd-10	0.43	5.0	4.2	0.131	0.150	16	14	2.0×10^6
Nd-20	0.30	4.0	3.0	0.112	0.100	16	14	3.4×10^6
Nd-30	0.21	2.4	2.5	0.088	0.085	15	12.6	5.7×10^6
Nd-40	0.20	2.3	2.0	0.087	0.080	14	12	5.1×10^6

The reversible penetration depth λ'_c of pinned flux line lattice is given by [33]

$$\lambda'_c = (H_{dc}d_i/\mu_o J_{c1})^{1/2} \quad (5.4.1)$$

where r_f is the interaction distance and is approximately given by $d_i = a_f/\zeta$ in a wide range of magnetic fields. In the above a_f is the fluxoid spacing and ζ is a constant dependent on the kind of pinning center and takes a value of about 4 for a large and strong pinning center [33]. The estimated values of λ'_c , for all the samples closely match the observed shift on the p/R axis. Since the measured reversible penetration depth (λ'_c) is not very much higher than the Campbell's reversible penetration depth (λ'_c), it can be clearly concluded that such a shift is due to the reversible flux motion in the pinning potential well, but not due to the weaklink nature of domain boundaries. Even though there are many domains in these bulk samples, the domain boundaries are still coupled strongly even at the maximum applied field of 10 KOe. If we apply still larger dc fields, we might probably observe more shift than the expected λ'_c due to the isolated domains, where the flux is completely reversible at the domain boundaries. The decoupling nature of melt textured domains has been observed in the samples processed in faster rate of cooling [34] and is described in the next section.

The cross over (p'/R) between the regions of differing slope of the measured flux profile is tabulated in Table I. This is found to be related to the volume fraction of the gaps (f_c) present in the sample as estimated from the microstructures. This supports the view that the flux initially penetrates the sample along the gaps, and then into the grains. Bulk current density of the sample is mainly dependent on the nature and extent of the gaps and is lower than the platelet critical current density J_{c2} . Therefore, if the crack density is minimized in the specimen, the transport critical current density J_{c1} is expected to be as large as the J_{c2} and this would be highly desirable for practical applications. Unlike in the case of Y-123, where the gaps run across the size of the domains, those in Nd-123 are not continuous. The possible reason for this is the higher rate of crystallization of Nd-123 as concluded in Chapter 3. This aspect could be important in realizing large bulk J_{cs} with Nd-123 system.

5.4.2 Fast cooled textured samples

Magnetic flux profiles measured on Nd-40 samples processed at different cooling rates through peritectic temperature T_p are shown in Figs. 5.14, and 5.15 for 10 °C/h and 40 °C/h respectively. The features of the flux profiles are similar to those of the slow cooled (1°C/h) samples (see Fig. 5.10) except for the continuous shift on the p/R axis. Continuous increase in the shift from the origin for different dc fields can arise from the reversible flux motion at the domain boundaries. In the slow cooled samples (1,4 and 10°C/h) the estimated values of λ'_c from Campbell's model, closely compare with the observed shift (λ'_c) representing the reversible fluxoid motion to be associated with the pinning potential well. But in the fast cooled (40°C/h) sample, the observed shift at 10 KOe field is 160 μm and is considerably larger than the estimated reversible penetration depth of a flux line lattice, which is $< 15 \mu\text{m}$. Such a large observed shift could be due

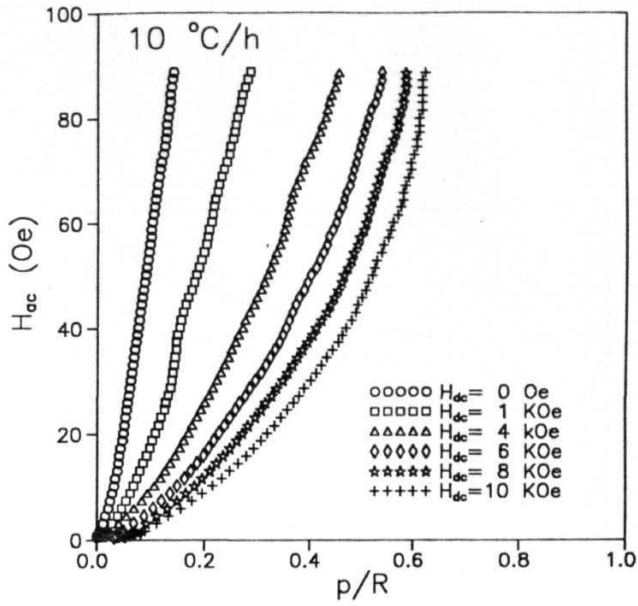


Fig. 5.14 Flux profiles in Nd-40 sample processed at 10 °C/h rate of cooling.

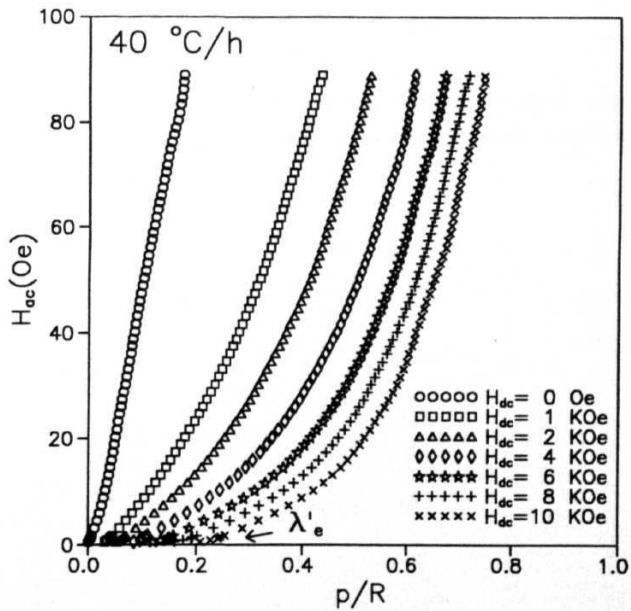


Fig. 5.15 Flux profiles in Nd-40 sample processed at 40 °C/h rate of cooling.

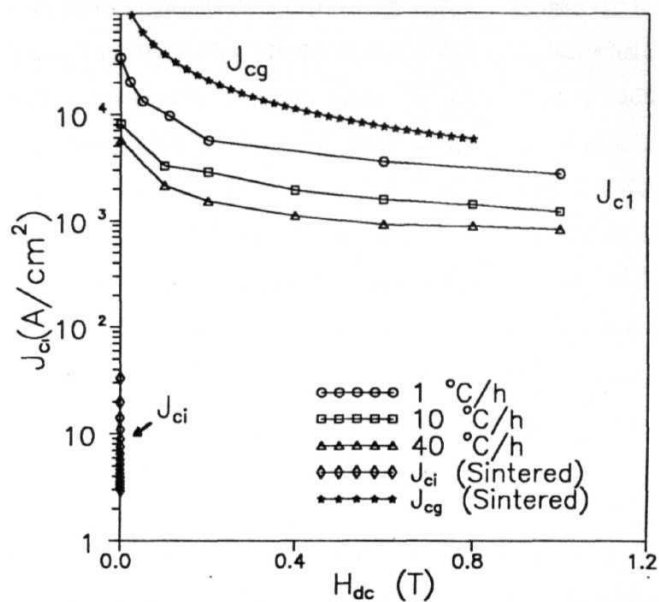


Fig. 5.16 Bulk J_{c1} of melt textured samples, processed at different cooling rates. The intergranular and intragranular critical current densities J_{ci} and J_{cg} of polycrystalline NdBCO sample are also shown for comparison.

to the **decoupling** of the domains which are weakly coupled either due to liquid phase at the domain boundaries or due to high angle domain boundaries. The strong field dependence of reversible penetration depth suggests that the observed shift is associated with the domain boundaries that are decoupled at high dc fields, where the ac fluxoids freely move in and out without getting pinned along the domain boundaries. This is analogous with the reversible flux motion along the grain boundaries in polycrystalline samples reported in literature [19,20] as well as in the sintered NdBCO (Fig.5.5). The measured bulk critical current density of the various fast cooled samples are shown in Fig. 5.16. The bulk critical current density of the fast cooled melt textured sample processed at fast rate (40 °C/h) is $\sim 6000 \text{ A/cm}^2$, which is two orders of magnitude higher than the intergranular critical current density (J_{ci}) in polycrystalline sample. Also the field dependence of J_c is much better (weaker), but it is not as good as that for the samples processed at slow cooling rates.

The bulk critical current density measurements are done on big samples of size 4 mm x 4 mm x 12 mm containing several domains through the measurement of flux profiles. They are expected to be analogous with the transport J_c in the sense that the weak links such as domain boundaries and interplatelet gaps participate. Usual transport J_c measurements cannot be carried out on such big samples, due to the limitation on the magnitude of high currents that can be passed. Measurement of magnetic J_c using commercial SQUID magnetometers also restricts the size of the samples that can be studied. Thus the flux profile measurements is a convenient way of estimating bulk J_c in large sized samples.

5.5 Information on domain coupling strength from flux profiles

When a magnet is placed on a melt textured superconductor, the levitation force acting on the magnet is proportional to the radius of the current loop. Due to the weakly coupled domain boundaries, the shielding current localizes in individual domains and reduces the levitation force drastically. To put the as processed melt textured samples into practical applications, it is necessary to characterize them using nondestructive methods. Many techniques have been proposed in the literature to do the same. Some researchers measured the trapped field distribution on the surface and thereby the critical current density using a Hall probe [35,36]. Some others have measured flux distribution on the sample by high resolution Farady (HRF) effect [37-39]. In the latter method, iron garnet film saturates at high fields and restricts the field range in which characterization is to be conducted. In this section, it is proposed that the ac inductive method is very useful to assess the quality of large sized melt textured samples.

For this purpose, the results of flux profiles on three samples with different microstructural features, namely, the melt grown Nd-123 with 40 mol% $\text{Nd}_4\text{Ba}_2\text{Cu}_2\text{O}_{10}$ (Nd-422) inclusions cooled at a rate of 1 °C/h [Nd-40-1], and at 40 °C/h [Nd-40-40] and the sintered NdBCO sample, have been compared.

Figures 5.10, 5.15 and 5.5 show the flux profiles recorded in Nd-40-1, Nd-40-40 and sintered NdBCO samples respectively. Figure 5.17 shows that, at a large $H_{dc} = 10$ KOe, the flux profiles of all the three samples have shifted along the p/R axis, from the origin, which represents the reversible penetration depth. Figure 5.18 shows the variation of the measured (λ'_c) and calculated (λ'_c) reversible penetration depths with the applied field strength for Nd-40-1 and Nd-40-40. The good agreement between the measured

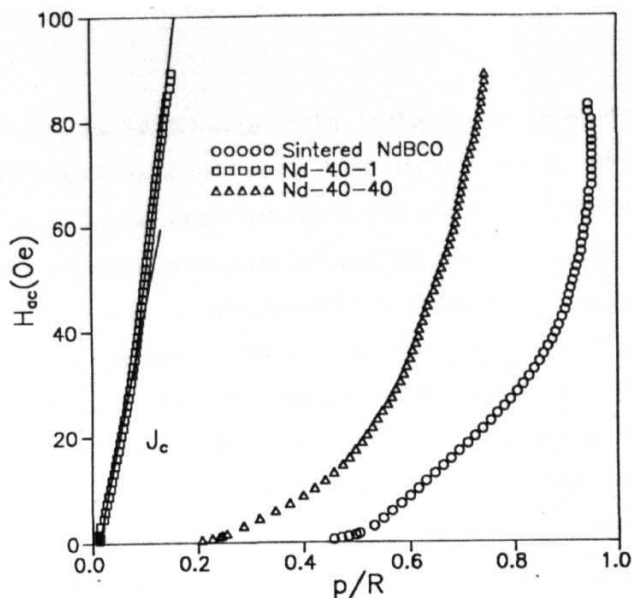


Fig. 5.17 Magnetic flux profiles at 77 K, 10 KOe dc field in sintered NdBCO, melt textured Nd-40 processed at 1 °C/h (Nd-40-1) and melt textured Nd-40 processed at 40 °C/h rate of cooling (Nd-40-40). The large reversible penetration depth (indicated by the shift on p/R axis from the origin) in the sintered and Nd-40-40 samples is due to the reversible fluxoid motion along the weakly coupled grain/domain boundaries.

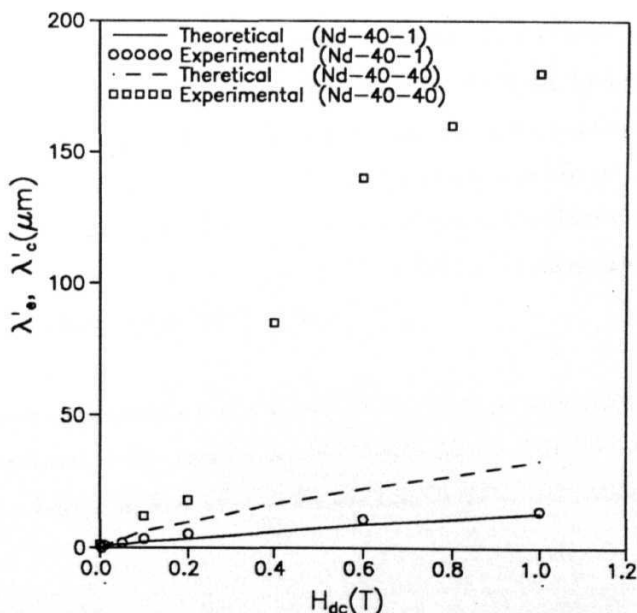


Fig. 5.18 Measured reversible flux penetration depth (λ'_c) versus the external dc field in Nd-40-1 and Nd-40-40 samples. The reversible penetration depths (λ'_c) calculated from the Eqn. (5.4.1) are shown as curves for the above samples.

and the theoretical curve for Nd-40-1 suggests that in this case the reversible penetration depth which is of the order of $\sim 14 \mu\text{m}$ is due to the reversible fluxoid motion of pinned vortex lattice. In the case of the fast cooled melt grown sample [Nd-40-40], the measured reversible penetration depth agrees well with the theoretical one ($\sim 18 \mu\text{m}$) at low external dc fields, but as the dc field strength is increased, it is found to deviated gradually. The measured reversible penetration depth of $\sim 160 \mu\text{m}$ is much more than the theoretical values at high dc fields. This implies that there exist regions of reversible fluxoid motion other than the reversible fluxoid motion of a pinned lattice. Two of the possible origins viz., large sized normal regions such as big voids and large extent of low T_c solid solution regions which turn normal on dc field application can be ruled out from the observed microstructural features and the sharp diamagnetic transition leaving the option of weakly coupled domain boundary regions to be the source. Agreement of theoretical values of λ'_c with the observed λ'_c at low fields and deviation at high dc fields is understandable because the supercurrent flows as a single loop despite the normal regions at domain boundaries due to Josephson coupling at low fields, while at high fields the weak domain boundaries decouple, and the screening currents flow as many small loops in the individual domains. In this situation, the ac fluxoids penetrate the sample along the domain boundaries freely without getting pinned. This phenomena is analogous with the polycrystalline sample, where the boundaries of the grains decouple very easily and destroy the intergranular current density. In the case of sintered NdBCO the reversible penetration depth is $\sim 540 \mu\text{m}$ at 1 KOe field and is $\sim 40\text{-}60\%$ of the sample dimension as is also reported in literature for YBCO [19].

The comparison of the results of flux profiles on the three samples thus reveals that the domain boundaries in the samples processed with slow cooling rate are strongly coupled even at a field of 10 KOe and the domain boundaries in the samples processed

at high rate of cooling are relatively weak and are decoupled at high fields. In the case of polycrystalline samples, the randomly oriented small sized grains are very easily decoupled even at very low applied fields (< 1 KOe). Hence, by measuring the magnetic flux profiles on large sized bulk melt textured samples, they can be assessed for their quality.

5.6 Theoretical model calculations

This section describes the calculation of the flux profiles of an infinitely long cylinder with radius R of type II superconductors exposed to an external field $H = H_{dc} + H_{ac}\cos(\omega t)$ applied along the axis of the cylinder, based on Kim's critical state model. We denote the maximum and minimum values of H by $H_A = H_{dc} + H_{ac}$ and $H_B = H_{dc} - H_{ac}$. In the critical state model, by application of an external field H , a macroscopic current $J(x)$ flows in the sample and the local flux density $B_i(x)$ is written as

$$B_i(x) = \mu_o H + \mu_o \int_x^R J(x') dx', \quad (5.6.1)$$

where $\mu_o = 4\pi \times 10^{-7}$ H/m. Using $B_i(x)$ the average flux density $B(H)$ in the sample can be calculated as

$$B(H) = \frac{2}{R^2} \int_0^R x B_i(x) dx \quad (5.6.2)$$

Thus the penetration depth $p = R \left(1 - \sqrt{1 - \frac{\mu_c d [B(H_A) - B(H_B)]}{2\mu_o d H_{ac}}} \right)$ is calculated for the following three cases. The first case is for a region of the field $0 < H_A < H_p$, where H_p is the full penetration field. The second case is for $H^* < H_A$, where the reverse supercurrent penetrates to the center of the specimen before H is cycled back to zero. The third case is for the intermediate fields, $H_p < H_A < H^*$. When H_{dc} has a nonzero value, each of the above cases is further classified into several different regions, depending on the magnitude of H_B . The detailed calculations for $B(H)$ in all possible cases are given in Ref. 40. By taking the same fit parameters given in section 5.3.2 with $K = 3.58 \times 10^8$

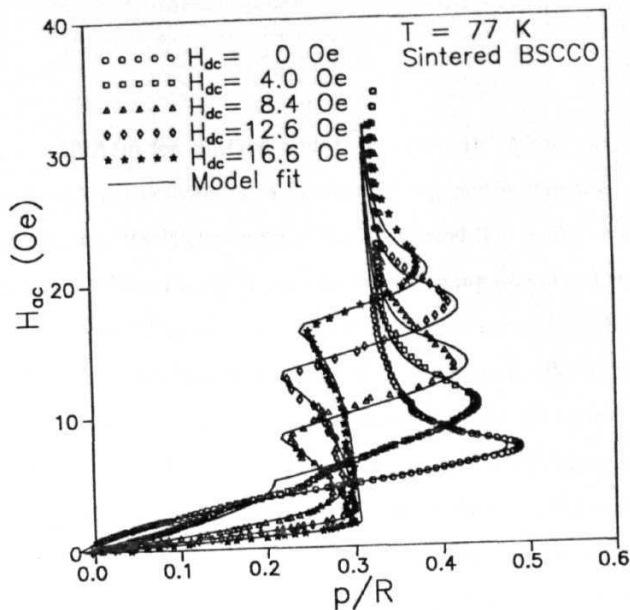


Fig. 5.19 Simulation of measured flux profiles at various dc fields to the Kim's critical state model for sintered $Bi_{1.2}Pb_{0.3}Sr_{1.5}Ca_2Cu_3O_y$.

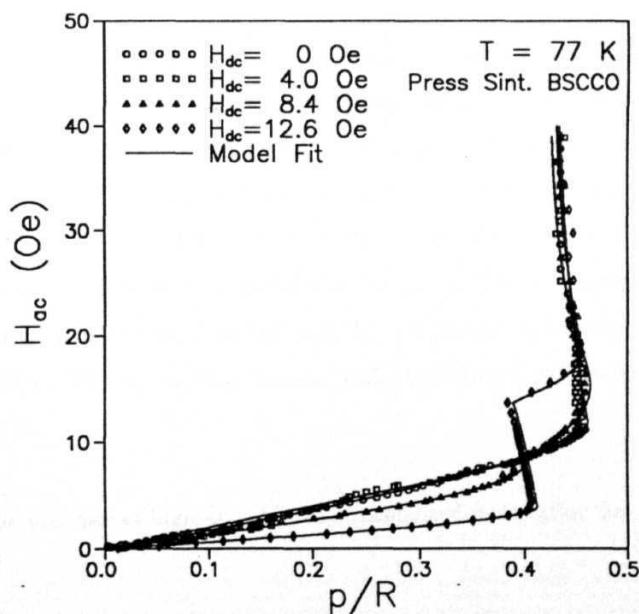


Fig. 5.20 Simulation of measured flux profiles at various dc fields to the Kim's critical state model for press sintered $Bi_{1.2}Pb_{0.3}Sr_{1.5}Ca_2Cu_3O_y$.

Λ^2/m^3 , $H_o = 450 \text{ A/m}$ for sintered and $K = 4.67 \times 10^9 \text{ A}^2/\text{m}^3$, $H_o = 5010 \text{ A/m}$ for press sintered, p/R is calculated as a function of H_{ac} and is shown as solid line in Figs. 5.19 and 5.20 for the BSCCO samples. The calculated flux profiles agree well with the experimental data. From Fig. 5.19 we note the following aspects. The nonlinearity and peak like structure could be well simulated in the absence of H_{dc} . Both of these properties are related to the inhomogeneity in the current path. When the inhomogeneity in the sample increases, the nonlinearity increases, and the over shoot of the peak from the vertical asymptotic line also increases. The stronger the field dependence, the more the non-linearity and over shoot from the full penetration. In the case of press sintered sample, the peak like structure and the non-linearity are less pronounced. So, by press sintering the coupling between grains has been strengthened compared to that in the sintered sample. When H_{dc} is comparable to H_{ac} , an oscillatory behavior is seen in both the samples, but the amplitude of oscillation around the vertical line is less in the press sintered sample.

Since the extent of flux penetration is high in sintered NdBCO and since the flux profile above H_{c1g} is also non-linear, the strong field dependence of intergranular critical current J_{ci} as well as the intragranular critical current density J_{cg} have been taken into account. Solid line in Fig. 5.21 shows the fit to the Kim's critical state model with $K = 3.9 \times 10^7 \text{ A}^2/\text{m}^3$, and $H_o = 118 \text{ A/m}$ for intergranular region. Experimental data is found to agree well with the theoretical calculations. The intergranular critical current density at zero field is calculated from $J_{ci}(0) = K/H_o$ and is found to be 33 A/cm^2 . The calculated $J_{ci}(H)$ from the Kim's model with the above fit parameters is shown as inset in Fig. 5.21.

In the presence of high dc fields, the normalized penetration has reached a value of

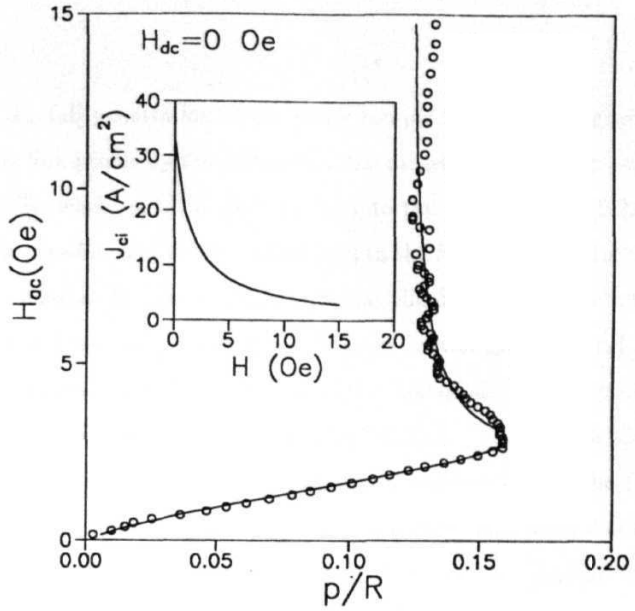


Fig. 5.21 Simulation of the measured flux profile in the absence of dc field for sintered Nd-BCO to the Kim's critical state model. Inset shows the field variation of J_{ci} calculated from the fit parameters of K and H_0 .

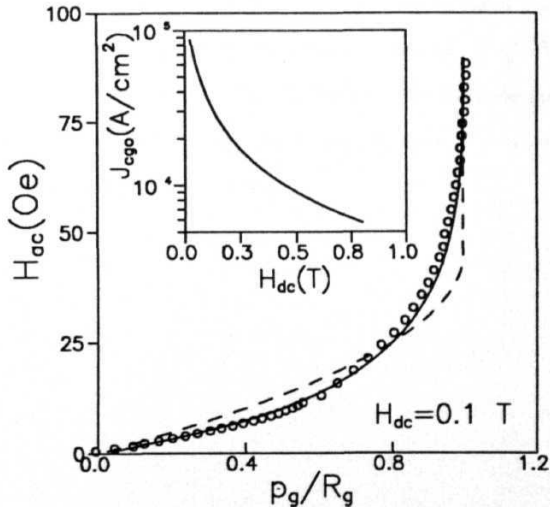


Fig. 5.22 The profile into the grains as extracted from the measured global flux profile. The solid line is a fit to Kim's critical state model after incorporating a Gaussian distribution in J_{cg} . Deviation from the experimental data can be seen when a single valued J_{cg} is considered (dashed line). Inset shows the field variation of J_{cgo} .

I, which represents the full **penetration** of the entire sample including the grains. So, we have extracted the flux profile by the grains from the measured global flux profile by using $\frac{p_g}{R_s} = 1 - \frac{(1-p/R)}{(1-p^*/R)}$, where p_g is the penetration into the grain. Figure 5.22 shows the extracted grain flux profile, and its fit (dashed line) to the Kim's critical **state** model. Grain radius (R_g) is taken as $7.5 \mu\text{m}$. It is thought that the deviation of the measured profile from the fit could be due to a local distribution in the grain critical current density (J_{cg}) due to the presence of $\text{Nd}_{1+x}\text{Ba}_{2-x}\text{Cu}_3\text{O}_{7-\delta}$ precipitates in the grains that were responsible for a broader $\chi'(T)$ transition (Fig. 4.1 (a)). Assuming a Gaussian distribution in the local values of the J_{cg} in the specimen as described by the function $f(J_{cg}) = A \text{Exp}(-\frac{(J_{cg}-J_{cgo})^2}{2\Delta^2})$ (here, A is a normalization constant, J_{cgo} is the mode of the critical current density J_{cg} that represents the average value, and Δ is the half width at half maximum), the calculated effective penetration due to the distribution of J_{cg} using Kim's critical state model is shown as solid line in Fig. 5.22. For $J_{cgo} = 1.85 \times 10^5 \text{ A/cm}^2$ and $\Delta = 1.6 \times 10^5 \text{ A/cm}^2$, agreement with the experimental data can be seen to be very good. The half width of the Gaussian distribution in J_{cg} is quite large and can have its origin in the presence of large extent of low T_c precipitates of solid solutions of the type $\text{Nd}_{1+x}\text{Ba}_{2-x}\text{Cu}_3\text{O}_{7-\delta}$ is evidenced by the broad transition in $\chi'(T)$ and a very broad intragranular peak in $\chi''(T)$. Inset in Fig. 5.22 shows the field dependence of the average intragranular J_{cgo} as calculated from the fit parameters $K = 5.1 \times 10^{13} \text{ A}^2/\text{m}^3$ and $H_o = 27760 \text{ A/m}$ for the intragranular region.

References

- [1] M. Nikolo and R. B. Goldfarb, *Phys. Rev. B* **39**, 6615 (1988).
- [2] I. X. Chen, J. Noguez and K. V. Rao, *Cryogenics* **29**, 800 (1989).
- [3] D. X. Chen, A. Sanchez, T. Puig, L. M. Martinez, and J. S. Muñoz, *Physica C* **168**, 652 (1990).
- [4] T. Ishida and R. B. Goldfarb, *Phys. Rev. B* **41**, 8939 (1990).
- [5] L. Ji, R. H. Sohn, G. C. Splading, C. J. Lobb and M. Tinkham, *Phys. Rev. B* **40**, 10936 (1989).
- [6] Y. Kim, Q. Harry Lam and C. D. Jufferies, *Phys. Rev. B* **43**, 11404 (1991).
- [7] S. Ravi and V. Seshu Bai, *Phys. Rev. B* **49**, 13 082 (1994).
- [8] S. Ravi and V. Seshu Bai *Physica C* **230**, 51 (1994).
- [9] O. F. Schilling, K. Aihara, A. Soeta, T. Kamo and S. Matsuda, *Phys. Rev. B* **47**, 8096 (1993).
- [10] D. Berling, E. V. Antipov, J. J. Capponi, M. F. Gorius, B. Loegel, A. Mehdaoui and J. L. Tholence, *Physica C* **225**, 212 (1994).
- [11] X. C. Jin, Y. Y. Xue, Z. J. Huang, J. Bechtold, P. H. Hor and C W. Chu, *Phys. Rev. B* **47**, 6082 (1993).
- [12] M. G. Karkut, M. Slaski, L. K. Sagdahl, and K. Fossheim, *Physica C* **215**, 19 (1993).
- [13] C. P. Bean, *Phys. Rev. Lett.* **8**, 250 (1962); *Rev. Mod. Phys.* **36**, 31 (1964).
- [14] Y. B. Kim, C. F. Hempstead and A. R. Strnad, *Phys. Rev. Lett.* **9**, 306 (1962).
- [15] Y. B. Kim, C. F. Hempstead and A. R. Strnad, *Phys. Rev.* **129**, 528; (1963).
- [16] G. Ravi Kumar and P. Chaddah, *Phys. Rev. B* **39**, 4704 (1989).
- [17] A. M. Campbell, *J. Phys. C* **2**, 1492 (1969).
- [18] A. M. Campbell and F. J. Blunt, *Physica C* **172**, 253 (1990).
- [19] B. Ni, T. Munakata, T. Matsushita, M. Iwakuma, K. Funki, M. Takeo and K. Yamafuji, *Jpn. J. Appl. Phys.* **27**, 1658 (1988).
- [20] A. Dang, P. Godelaine and Ph. Vanderbernden, R. Cloots and M. Ausloos, *J. Appl. Phys.* **77**, 3560 (1995).
- [21] H. Kupfer, A. A. Zhukov, R. Kresse, R. Meier-Hirmer, W. Jahn, T. Wolf, T. Matsushita, K. Kimura and K. Salama, *Phys. Rev. B* **52**, 7689 (1995).
- [22] V. Seshu Bai, S. Ravi, T. Rajasekharan and R. Gopalan, *J. Appl. Phys.* **70**, 4378 (1991).
- [23] T. Asano, Y. Tanaka, M. Fukutomi, K. Jikihara, J. Machida and H. Maeda, *Jpn. J. Appl. Phys.* **27**, 1652 (1988).
- [24] M. R. Koblishka, Th. Schuster and H. Kronmüller, *Physica C* **219**, 205 (1994).
- [25] C. P. Bean and J. D. Livingston, *Phys. Rev. Lett.* **12**, 14 (1964).
- [26] T. B. Lindemer, E. D. Specht, P. M. Martin and M. L. Flitcroft, *Physica C* **255**, 65 (1995).
- [27] M. Mironova, D. F. Lee, and K. Salama, *Physica C* **211**, 188 (1993).
- [28] R. Gopalan, T. Roy, T. Rajasekharan, G. Rangarajan and N. Hari Babu, *Physica C* **244**, 106 (1994).
- [29] Z. L. Wang, A. Goyal, and D. M. Kroeger, *Phys. Rev. B*, **47**, 5373 (1993).

- [30] Th. Schuster, M. R. Koblishka, H. Kuhn, M. Glücker, B. Ludescher, and H. Kronmüller, J. Appl. Phys. 74, 3307 (1993).
- [31] M. **Murakami**, S. Gotoh, N. **Koshishuka**, S. Tanaka, T. Matsushita, S. Kambr, and K. **Kitazawa**, **Cryogenics**, 30, 390 (1990).
M. Murakami, S. Gotoh, H. **Fujimoto**, K. Yamaguchi, N. Koshizuka and S. Tanaka **Supercond. Sci. Technol.** 4 S43 (1991).
- [32] D. F. Lee, V. **Selvamanickam** and K. Salama, Physica C 202, 83 (1992).
D. Shi, S. Sengupta, L. S. Lou, C. Varanasi and P. J. McGinn, Physica C 213, 179-184 (1993).
- [33] A. M. Campbell, J. Phys. C 4, 3186 (1971).
- [34] N. Hari Babu, T. Rajasekharan and V. Seshu Bai (Submitted)
- [35] I. Chen, J. Liu, R. Weinstein and K. Lau, J. Appl. Phys. 72, 1013 (1992).
Y. H. Zhang, A. Parikh and K. Salama, IEEE Trans. Appl. Supercond., 7, 1787 (1997).
- [36] H. **Fujimoto**, T. Higuchi, K. Kawano and T. Ban, IEEE Trans. Appl. Supercond., **7**, 1124 (1997).
- [37] Th. Schuster, M. R. Koblishka, H. Kuhn, M. Gliicker, B. Ludescher, and H. Kronmuller, J. Appl. Phys. 74, 3307 (1993).
M. R. Koblishka, Th. Schuster and H. Kronmuller, Physica C 219, 205 (1994).
- [38] S. Gotoh and N. **Koshizuka**, Physica C 176, 300 (1991).
- [39] M. V. **Indenbom**, N. N. Kolesnikov, M. P. **Kulakov**, I. G. Naumenko, I. Nikitenko, A. A. Polyanskii, N. F. Vershinin and V. K. **Vlasko-Vlasov**, Physica C 166 486 (1990).
- [40] K. **Yamamoto**, H. Mazaki and H. Yasuoka, Phys. Rev. B 47, 915 (1993).

Chapter 6

dc magnetization measurements

6.1 Introduction

As has been discussed in Chapter 3, when **Nd-123** is processed in the ambient atmosphere a low T_c solid solution with the formula $\text{Nd}_{1+x}\text{Ba}_{2-x}\text{Cu}_3\text{O}_{7-\delta}$ is formed by the replacement of Ba atoms by Nd atoms [1]. Yoo *et al.* [2] melt processed $\text{NdBa}_2\text{Cu}_3\text{O}_{7-\delta}$ (Nd-123) in reduced oxygen partial pressures to suppress the solid solution phase. The J_c of Nd-123 bulk material processed under low oxygen partial pressure has been found to be even higher than that of the MPMG-processed Y-123 in the high field region [2,3]. An anomalous peak in J_c occurs at high fields. The origin of the peak effect has been discussed in many reports [4-8]. It has been proposed that existence of peak effect is due to the low T_c solid solution phase turning normal on applying fields (2-3 T). Addition of Nd-422 inclusions is a means of drastically modifying the microstructure of melt processed Nd-123. In Y-123 such additions lower the 123 platelet widths and the width of the gaps between the platelets and refine the Y-211 particle size [9-11]. In Nd-123 flux pinning mechanism originating from the defects at the 123/422 interface, possibly introduced by refining the Nd-422 size, in addition to the already existing pinning from low T_c solid solution phases. By the experience on Y-123 system, one can expect pinning from the 123/422 interface defects to reinforce the low field J_c which is not very high in melt processed stoichiometric Nd-123. It is also of interest to know the optimum Nd-422 content for a maximum in J_c .

In this chapter, correlation of the enhancement of J_c estimated from magnetization data with the interface area is described. An anticlockwise tilt in the magnetic hysteresis loops is analysed by considering the paramagnetic moment of Nd^{3+} ions, in addition to the critical state model proposed for type-II irreversible superconductor, is also described.

6.2 Experimental

Microstructural features of the melt textured samples (Nd-0, Nd-10, Nd-20, Nd-30 and Nd-40) have been described in detail in chapter 3. Microstructural features such as width of the platelets (P_w), gaps between the platelets (C_w), particle size of the Nd-422 inclusions etc. were quantitatively estimated using standard metallographic methods, and the quoted values were the average over several measurements.

The dc magnetization measurements were performed using a SQUID magnetometer (Quantum Design) up to a magnetic field of 5.5 T. For each measurement, a scan length of 3 cm was employed in order to minimize the inhomogeneity of the magnetic field.

6.3 Results on melt processed NdBCO samples

Before discussing the results of the magnetization measurements, microstructural features are briefly outlined here. All the samples exhibit 6-8 mm^2 sized domains with very clean domain boundaries. There is no liquid phase residual from the peritectic reaction at the domain boundaries. Nd-422 phase particles are found to be uniformly distributed in the Nd-123 matrix. The particle size of Nd-422 inclusions becomes smaller as the Nd-422 content is increased. An important change in the Nd-422 morphology is that more number of particles per unit area become spherical as we go from Nd-0 to Nd-40. There

are 00% – 70% spherical Nd-422 particles with an average diameter of 2 μm or less in the Nd-30 and Nd-40 samples, whereas only 20% - 30% particles are spherical in Nd-0, Nd-10 and Nd-20 samples. Number of fine Nd-422 particles per unit volume is increased as the concentration of Nd-422 particles is increased. Various **microstructural** parameters are quantitatively estimated from several micrographs, averaged, and the values are tabulated in Table 6.1 for different samples.

Though the samples gave a sharp transition in the resistivity versus temperature plots, there could still be a minor amount of low T_c phase, which forms locally. The presence of low T_c phases and weakly coupled domain boundaries in the samples can be investigated by measuring the ac susceptibility [12,13]. Temperature variation of low field ac susceptibility is shown in Fig. 4.4 for various samples. All the samples showed sharp transitions at around 92 K and sharp peaks in χ' and χ'' respectively. If there were some weakly coupled domain boundaries, we would have observed two peaks in the ac loss corresponding to the weakly coupled interdomain and intradomain regions. The observed sharp transition in χ' , and sharp peak in χ'' show the suppression of weak links to large extent and there are no low T_c phases.

Figure 6.1 shows the temperature variation of dc magnetization measured in zero-field-cooled (ZFC) and field-cooled (FC) states in field of 10 mT. When the sample is zero field cooled, it showed sharp diamagnetic transition at 92 K, as in the case of $\chi'(T)$. When the sample is field cooled, the applied external field is trapped, which implies existence of very strong pinning.

Magnetization hysteresis loops measured at 5 K, 35 K and 77 K are shown in Figs.

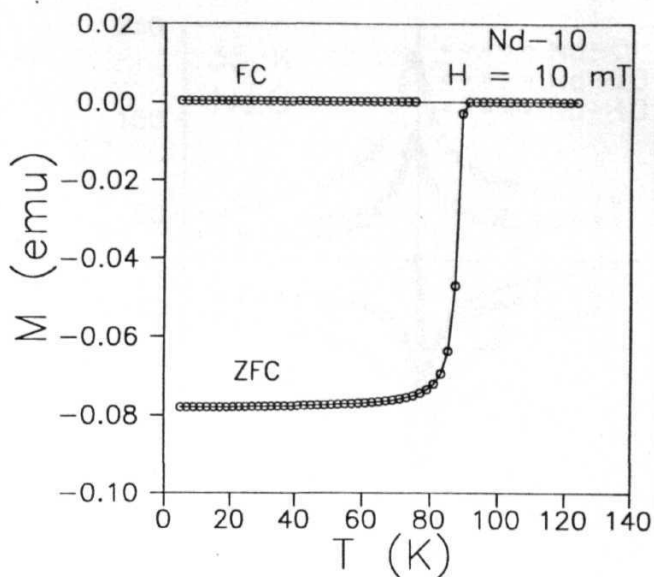


Fig. 6.1 Temperature variation of zero field-cooled (ZFC) and field-cooled (FC) magnetization for Nd-10 sample.

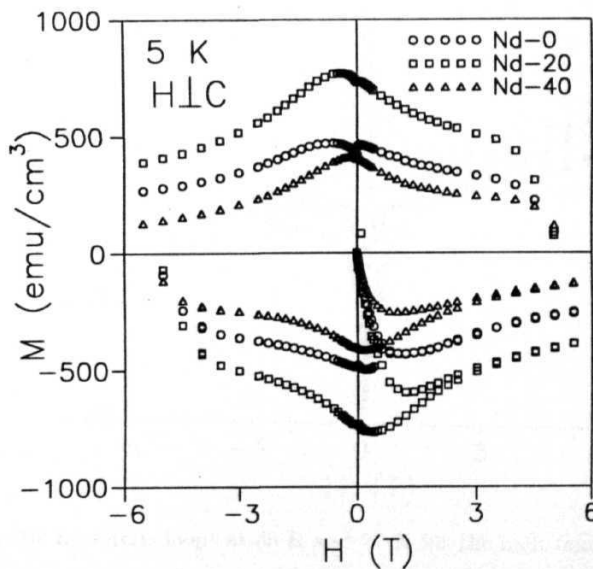


Fig. 6.2(a) Magnetic hysteresis loops at 5 K for the melt textured NdBCO samples.

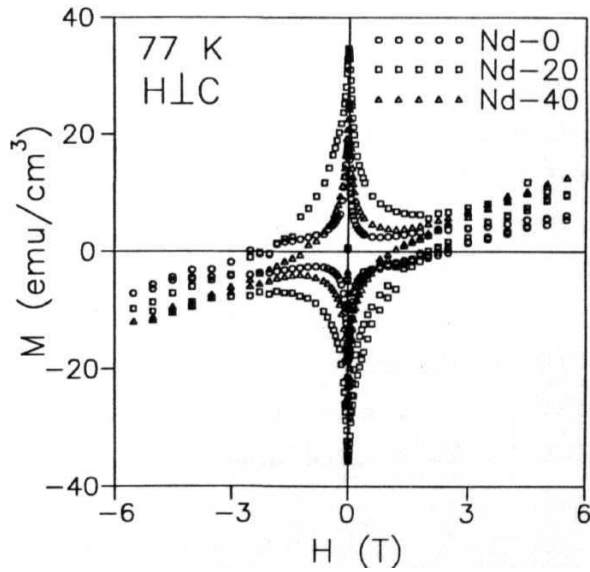
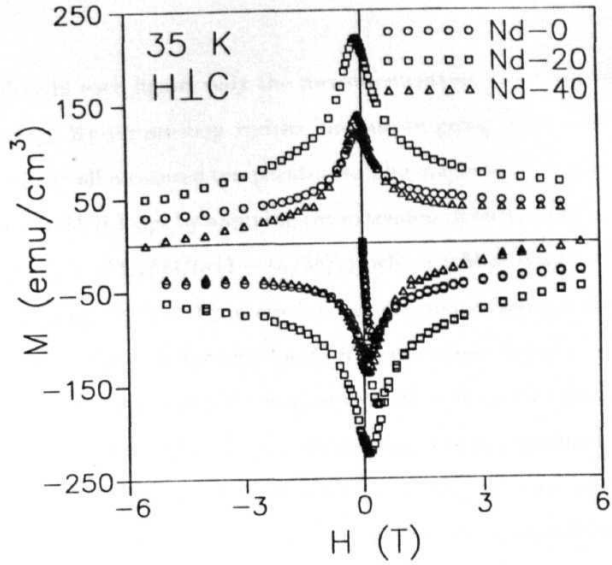


Fig. 6.2(b)&(c) Magnetic hysteresis loops at 35 K and 77 K for the melt textured NdBCO samples.

6.2 for various samples. In each figure, only the measurements on Nd 0, Nd 20 and Nd 40 are shown for clarity. **Hysteresis** loop widths increase in going from Nd-0 to Nd 30 and **decreases** for Nd-40 at all measured temperatures. The magnetic J_c values are determined in A/cm² from the M-H loops by applying the extended Hean's critical state model [14] from the equation $J_c = (20\Delta M)/(a\{1 - (a/36)\})$, where ΔM is magnetic hysteresis measured in emu/cm³, a and b (a < b) in cm are sample dimensions perpendicular to the applied magnetic field. Figure 6.3 shows the $J_c(H)$ determined from the width of the hysteresis loops for various samples at 5 K, 35 K and 77 K. It is found that J_c improves with increase in the mol % of Nd-422 in the **Nd-123** matrix. The maximum in J_c is found in the Nd-20 and Nd-30 samples at all measured temperatures. For the sample with 40 mol% Nd-422 content, the J_c is decreased due to a decrease in the superconducting path.

It is known that in the case of melt processed Y-123 samples, smaller spherical **Y-211** inclusions favor the formation of secondary defects in the 123 matrix at the **123/211** interface [15-20]. Such defects which compare in size with the coherence length, are believed to contribute to an enhancement in J_c . In the present samples all the microstructural parameters, particularly the Nd-422 size, saturates beyond 30 mol %. Further increase in Nd-422 content can therefore, be expected only to reduce the superconducting path and to reduce J_c .

The effect of Nd-422 inclusions on the microstructural parameters and J_c of the melt textured Nd-123 is found to be similar to that observed in the Y-123 system. The optimum Y-211 content for J_c in the latter case has been demonstrated to be around 28 mol % of Y-211 [21].

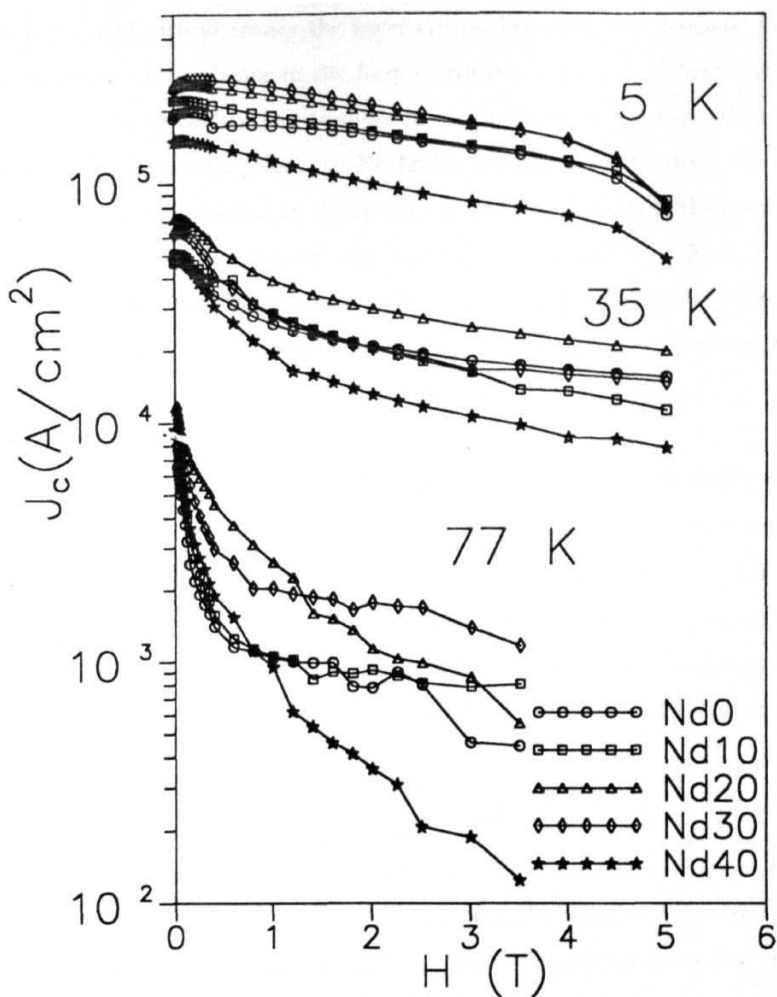


Fig. 6.3 Field variation of critical current density of the melt textured NdBCO samples at various temperatures.

When the applied field crosses the lower critical field, H_{c1} , the **magnetic flux penetrates** into the superconductor in the form of Abrikosov **vortices**. These vortices **get pinned** at the pinning centers (due to dislocations, stacking faults, oxygen deficiency or defects associated with extra phases like Nd-422) whose sizes are of the order of coherence length ξ . If the force (F) acting on the vortex per unit volume exceeds the pinning force per unit volume F_p , the vortices will continue their motion until $F = F_p$ at all points. The variation of the field in the interior of the sample is directly linked to the current that the sample can sustain without vortex motion, $F_p = J_c B$. If the pinning force per unit volume is more in the sample, one can have high J_c in the sample.

Even though large pinning centers (about 2 orders of magnitude larger than the coherence length $\xi_{ab} \sim 2$ nm), such as 211 (422) particles, may indeed contribute to pin vortices in the 211/123 interfaces, the effectiveness of the **flux** pinning per unit volume of precipitates is not as high as that of small pinning centers. Therefore, controlling the size, distribution and the concentration of 211 (422) inclusions is very important from the point of view of improving the superconducting properties of 123/422 interface. In single core vortex pinning [22],

$$J_c = \frac{\pi \xi H_c^2 N_p d^2}{4 \mu_o \phi_o^{1/2} H^{1/2}} = \beta H^{-1/2} \quad (6.3.1)$$

where N_p is the number of 422 inclusions per unit volume and d is their mean diameter. Thus, J_c is proportional to $N_p d^2$, which corresponds to the quantity V/d , with $V \sim N_p d^3$ being the volume fraction of the Nd- 422 precipitates. The quantity V/d i.e., the ratio of the volume percentage of Nd-422 phase particles to their mean diameter, is a measure of the interface area between Nd-422 particles and the Nd-123 superconducting matrix. V/d is obtained from the SEM pictures of melt textured NdBCO samples. In order to verify the occurrence of interfacial pinning mechanism in the samples, the experimental $J_c(H)$ curves have been fitted using Eqn. 6.3.1 and a very good fit has been obtained

at 77 K and at low applied fields, which gets deviated at high fields since the additional pinning from the solid solution phase becomes operative at these high (2-3 T) fields. The experimental points for the Nd-30 sample and the fit are shown in Fig. 6.4, the latter by a solid line. At lower temperatures, 5 K and 35 K, solid lines in the figure representing the curves calculated using the equation $J_c = \beta H^{-\alpha}$ with $\alpha = 1/2$, deviate from the experimental data. However, the experimental data at those temperatures can be fitted (broken lines in Fig. 6.4) with $\alpha = 0.46$ and 0.2 at 35 K and 5 K respectively.

The value of β is evaluated from the fit for the samples containing various percentage of 422, at 77 K. If the hypothesis of interfacial pinning is correct the parameter β in Eqn. 6.3.1 should display a linear dependence on V/d . Figure 6.5 shows that β depends linearly on V/d , at 77 K. Therefore, we can conclude that in the low-field region, the interfacial pinning by Nd-422 particles is the dominant pinning mechanism. In Fig. 6.5, the data point corresponding to Nd-123 with 40 mol % Nd-422 ($V/d \sim 3080$) is found to deviate substantially from linearity. The microstructure of the sample shows that volume percentage of the Nd-422 is more than that of the Nd-123 phase, causing the reduction in superconducting path.

At 77 K, the value of the power in Eqn. 6.3.1 is $1/2$ in the low field region, i.e., at $H < 2$ T approximately, while with increasing field at $H > 2$ T a plateau in which J_c is almost field independent occurs. In the Nd-30 sample above 2 T peak effect is observed, instead of plateau. The plateau zone becomes more evident as the temperature decreases. At lower temperatures $J_c(H)$ curves are found to deviate from $H^{-1/2}$, due to new pinning centers. These new active pinning centers (twins, oxygen defects, or dislocations) help to pin the vortex more strongly and the role of 422/123 interfacial pinning fades away among the contributions from the rest of the pinning centers. The change observed in

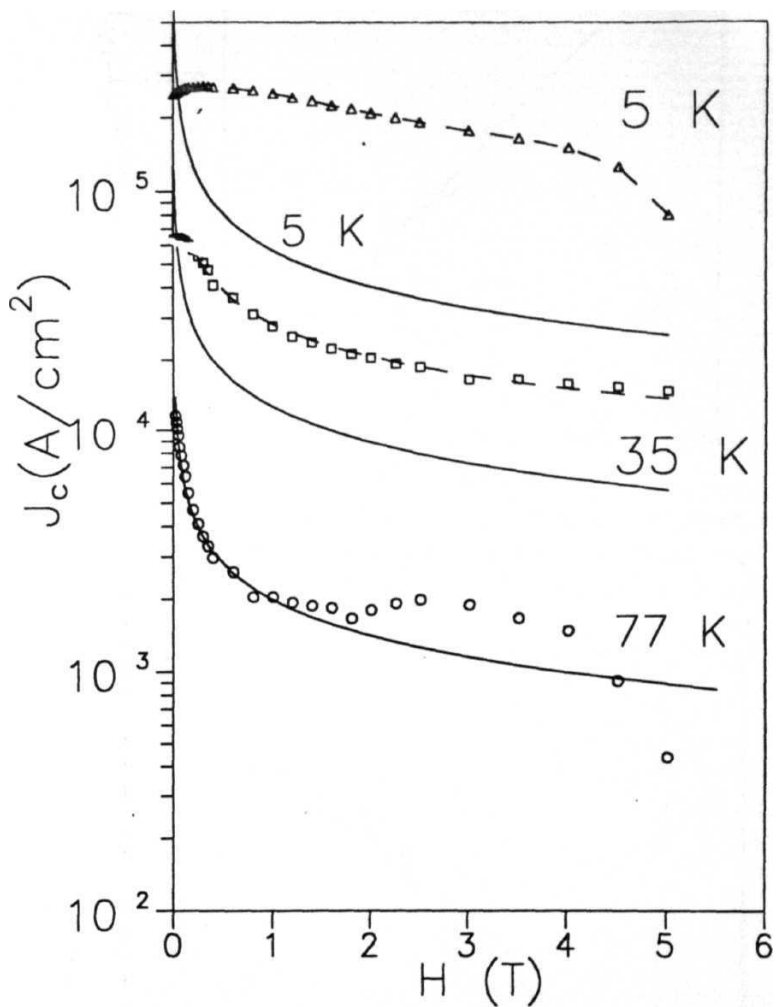


Fig. 6.4 Field variation of the critical current density for Nd-30 sample. The solid lines correspond to the fit of the experimental data with $\alpha = 1/2$ in Eqn. (6.3.1). Dashed lines correspond to the fit with $\alpha = 0.46$ and $\alpha = 0.2$ at 35 K and 5 K, respectively.

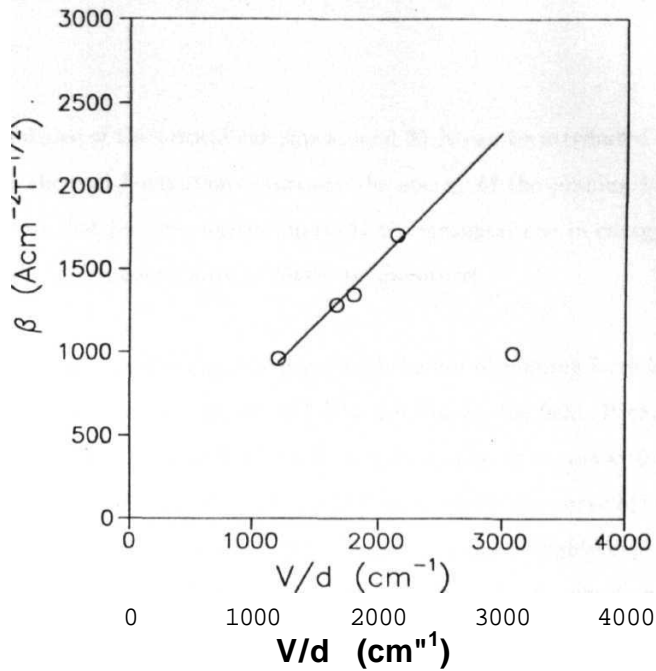


Fig. 6.5 The dependence of the parameter (β defined in Eqn. (6.3.1) on the 123/422 interfacial area (V/d) of the melt textured NdBCO samples. The linear relationship with V/d is consistent with the picture of normal core pinning at 123/422 interface represented by the above equation.

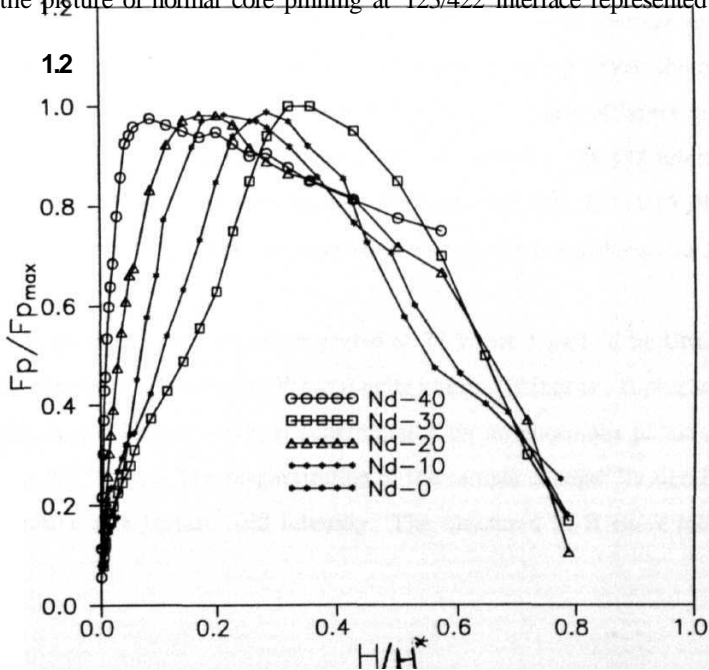


Fig. 6.6 Normalized pinning force versus the reduced field (H/H^*) for the melt textured NdBCO samples at 77 K.

the thermal dependence of the critical currents around 35 K can be attributed to depinning in which the thermal fluctuations overcome the energy of the pinning barriers of some pinning centers that become inactive and only the strongest one in energy, i.e., the 422/123 interfacial pinning contributes at higher temperatures.

For small size normal core pinning, the expected behavior of pinning force is proportional to $h(l - h)^2$ [23], where $h = H/H^*$ and H^* is the irreversible field. It can be seen from the Fig. 6.6 that for Nd-123 with 30 mol% sample, maximum occurs at 0.36 and it matches with the predicted (0.33) value of the inflection point for the curve $h(l - h)^2$. In the Fig. 6.6, it can be seen that the occurrence of peak positions is highly dependent on the value of the irreversible field. Hence, H^* should be measured precisely. Even though the error in measuring H^* is high in the present study, the maximum pinning force (Table 6.1) for Nd-30 sample indicates the effectiveness of the pinning centers in comparison with the other Nd-422 added samples. Microstructural studies show that the Nd-30 contains uniformly distributed Nd-422 insulating phase inclusions with average size of 1.5 μm . Out of the total Nd-422 particles, 60% particles are spherical. Even though these Nd-422 particles cannot contribute directly to flux pinning because of larger size when compared to coherence length ξ , the structural defects around a 123/422 interface can contribute to flux pinning as discussed earlier. It is observed that Y-211 (Y_2BaCuO_5) phase with a large surface curvature are associated with numerous dislocations [11,15].

The magnetization hysteresis loops measured at 77 K are found to be tilted in the anticlockwise direction for all samples. What is quite unusual is that the superconducting contribution by magnetization curve, is superimposed on an enormous paramagnetism arising from the Nd $3+$ ions. The magnetization of the sample changes its sign from the negative to positive at a certain field intensity. The measured M-H curve look like a

superposition of a superconducting **loop** and a paramagnetic magnetization **curve**, the **Meissner** diamagnetism being added on the **paramagnetism**. The tilt in the anticlockwise direction is **more** for the Nd-40 samples as compared to Nd-0. In order **to account** the paramagnetic moment of **Nd³⁺** ions, the M-H loop has been analysed by considering

$$M(H) = M_s(H) + M_p(H), \quad (6.3.2)$$

where M_s is the superconducting diamagnetic signal, and M_p is the paramagnetic contribution from **Nd³⁺** and is given by $M_p = NgJ\mu_B B_J(x)$ with $x = gJ\mu_B H/k_B T$ where N is the total number of atoms per unit volume, μ_B is Bohr magneton, k_B is the Boltzman constant, g is the Lande's g factor, and J is the angular momentum quantum number, and $B_J(x)$ is Brillouin function defined by

$$B_J(x) = \frac{2J+1}{2J} \text{Coth}\left(\frac{(2J+1)}{2J}x\right) - \frac{1}{2J} \text{Coth}\left(\frac{x}{2J}\right)$$

$M_s(H)$ is analyzed using critical state models. In the literature different functional dependences of J_c on H were proposed by observing the experimental data [25,26]. In the Bean's critical state model $J_c(H)$ is assumed as constant and in the Kim's critical state model, $J_c(H) = \frac{K}{H+a}$ where K and H_o are constants. Since all the measured loops have the reduction in loop width with increasing magnetic field, i.e, J_c is field dependent, we have used Kim's critical state model. Chen and Goldfarb [27] have given expressions for $M-H$ curves of **type-II** superconductors based on Kim's model. K and H_o are related to H_p and p by $H_p = H_o[-1 + (1 + p^2)^{1/2}]$ and $p = (2Ka)^{1/2}/H_p$ where a is the smaller dimension of the sample perpendicular to field direction and H_p is the full penetration field i.e, the field required to penetrate the sample upto the centre and it is temperature dependent. The parameters H_p and p are taken as free parameters in fitting the experimental data to the critical state models.

The solid line in Fig. 6.7 shows the **calculated** M-II curve for $H_p = 0.106$ T and p as 1.08 and it is found to agree well with the experimental data measured at 77 K. If there were no paramagnetic contribution, the expected M-II curve would have been as shown by the dashed line. The data points in Fig. 6.8 show the experimental loop at 5 K, the solid and dashed lines are fits to Eqn. 6.3.2 with and without the M_p term respectively. Both curves show good fit because the strong diamagnetic signal at low temperatures dominates the field induced paramagnetic contribution. At high temperatures, one has to consider the paramagnetic moment to understand the magnetic behaviour of the sample.

Table 6.1. Microstructural and pinning parameters of various melt textured samples.

	C_w	P_w	d	V/d	β	$F_{p,max}$
	μm	μm	μm	cm^{-1}	$Acm^{-2}T^{-1/2}$	TA/cm^2
Nd-0	0.70	10	6.0	1208	960	0.18
Nd-10	0.43	5.0	4.2	1667	1282	0.23
Nd-20	0.30	4.0	3.0	1802	1346	0.30
Nd-30	0.21	2.4	2.5	2151	1706	0.40
Nd-40	0.20	2.3	2.0	3085	991	0.09

The peak effect is observed only in a sample with an excess of 30 mol % Nd-422 in Nd-123 and is shown in Fig. 6.9. In the Sm-123 system the peak effect is observed in 10 mol % added sample, and it disappears with increase in Sm-211 concentrations [24]. Transmission electron microscopy studies on Sm-10 sample reveal that it contains oxygen ordered **ortho-II** structures distributed in nanometer scale, which is a low T_c phase and aids pinning of flux at high fields. There is no such ortho -II structure observed in Sm-20

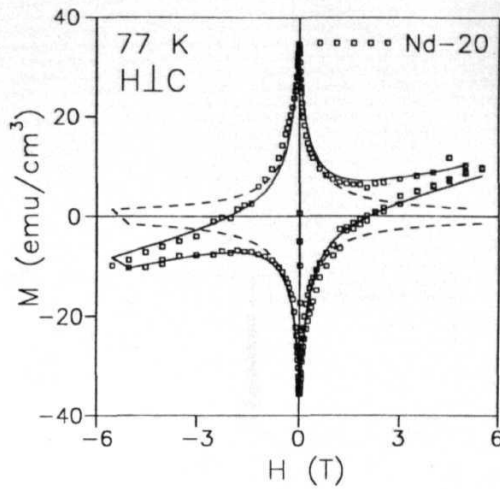


Fig. 6.7 M-H loop at 77 K for Nd-123 with 20 mol% Nd-422 sample. Dashed line is a M-H loop predicted for a type-II irreversible superconductor without any paramagnetic contribution. Solid line shows a good fit to Eqn. (6.3.2) suggesting that the paramagnetic contribution from Nd^{3+} ions is significant.

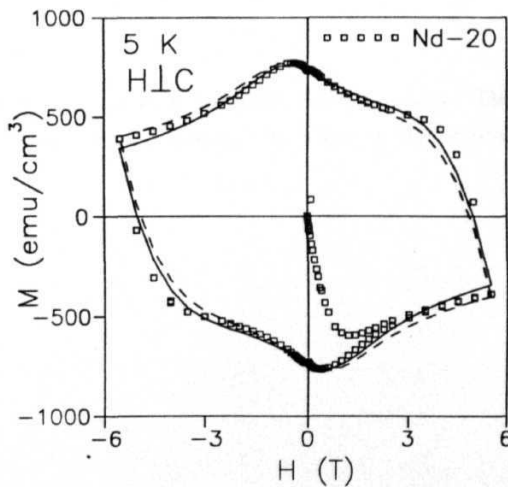


Fig. 6.8 M-H loop at 5 K for Nd-123 with 20 mol% Nd-422 sample. Solid line is a fit to Eqn. (6.3.2). Dashed line is a M-H loop predicted for a type-II irreversible superconductor without any paramagnetic contribution. Both are shown to be fitting well, suggesting that the strong Meissner diamagnetic signal dominates the field induced paramagnetic moment at lower temperatures.

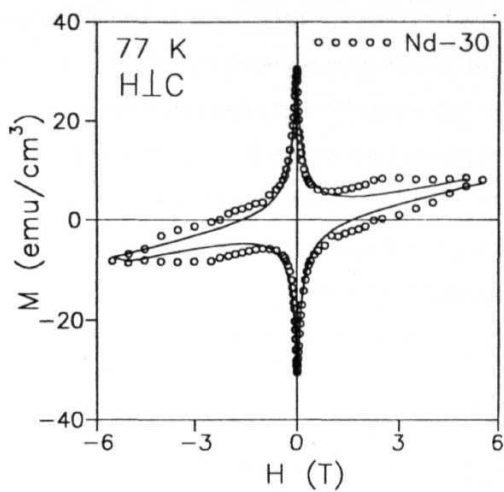


Fig. 6.9 M-H loop at 77 K for Nd-123 with 30 mol% Nd-422 sample. The deviation seen from a fit (solid line) to the Kim's critical state model is due to the presence of peak effect in this sample.

sample. Nakamura *et al* [8] demonstrated that existence of the peak effect in NdBCO system is not an intrinsic property, but it is considered to be controlled by the oxygen heat treatment. They found that samples heat treated in oxygen atmosphere at 340 °C for 200 h showed no peak effect, whereas samples heat treated at 500 °C for 100 h followed by 340 °C for 200 h showed peak effect, due to occurrence of spinodal decomposition at 500 °C. The heat treatment followed in the Nd-123 system has been given in section 3.4.2. Absence of peak effect in most of the samples is probably due to heat treating the samples in oxygen atmosphere at 500 °C for lesser time. However, the addition of Nd-422 inclusions enhanced the J_c at low fields at 77 K due to increase in the Nd-123/Nd-422 interfacial area. The solid line in Fig. 6.9 shows the fit to Kim's critical state model with additional paramagnetic contribution. The fit deviates from the experimental data in the region of the minor peak because, in Kim's model, the functional dependence of $J_c(H)$ is assumed to be as $K/(H+H_o)$, which shows a continuous fall in J_c with the applied field.

6.4 Results on **IG** processed **NdBCO** sample

In this section we discuss the results of magnetization measurements on IG processed sample. Magnetization hysteresis loops measured at 5 K, 35 K and 77 K are shown in Figs. 6.10(a), (b) and (c) respectively. The measured M-H loops could be simulated well using the Eqn. 6.3.2, suggesting that the paramagnetic contribution from Nd^{3+} ions is significant. The magnetic J_c values are estimated in A/cm^2 from the M-H loops by applying extended Bean critical state model [14]. The J_c values are derived from the following equation $J_c = (20\Delta M)/[a\{1 - (a/36)\}]$ where ΔM is magnetic hysteresis measured in emu/cm^3 , a and b ($a < 6$) in cm are sample dimensions perpendicular to the applied magnetic field. Figure 6.11 shows the $J_c(H)$ determined from the width of the hysteresis loops at 5, 35 and 77 K. The J_c values are slightly lower than the

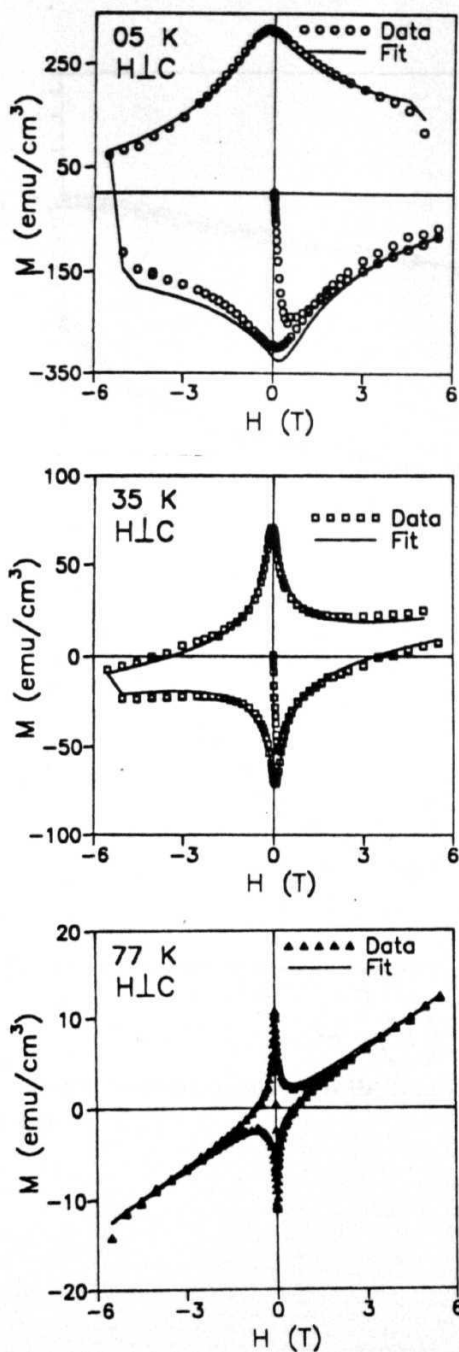


Fig.6.10 Magnetic hysteresis loops measured at (a) 5 K, (b) 35 K, and (c) 77 K for the G sample. Solid line shows a good fit to Eqn. (6.3.2) suggesting that the paramagnetic contribution from Nd^{3+} ions is significant.

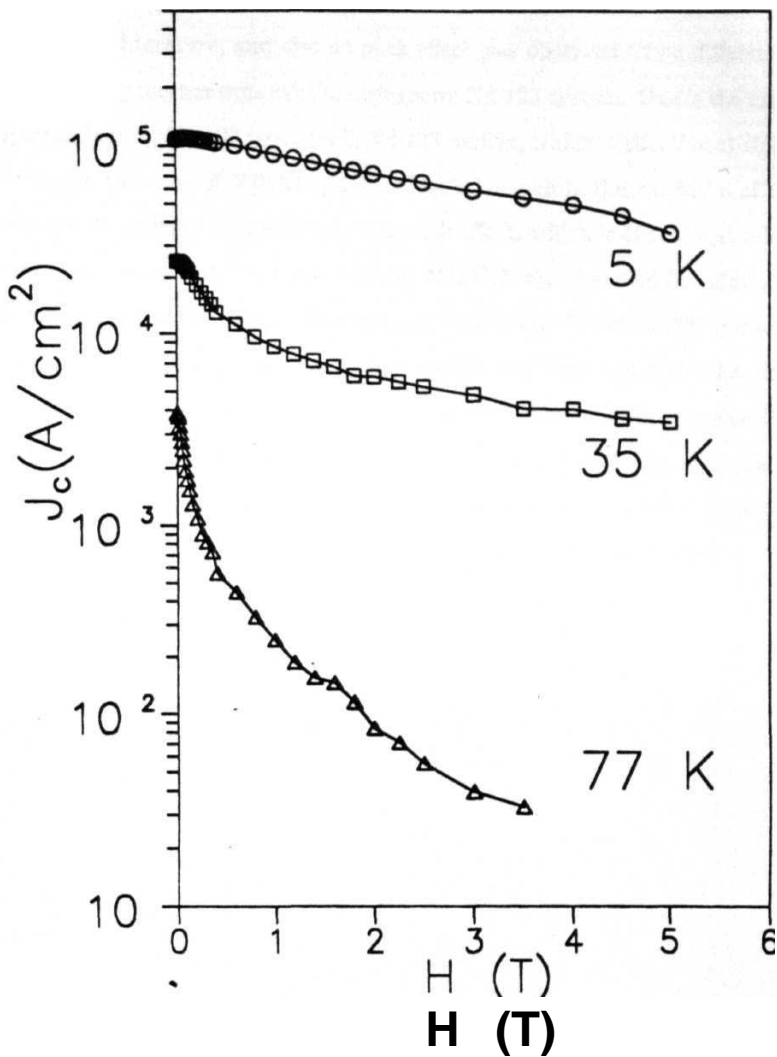


Fig. 6.11 Field variation of J_c for the IG processed NdBOO at different temperatures. Solid lines are guide to the eye.

reported values in literature, and also no peak effect was observed. Two different types of dominant pinning mechanisms exist in melt grown Nd-123 system. One is the existence of nonsuperconducting Nd-422 particles in Nd-123 matrix, which is effective at relatively low **fields** like in the case of YBCO system. The other one is the existence of low T_c Nd substituted Ba-regions, responsible for the peak effect, which is effective at relatively high fields. Improvement of J_c at low fields in NdBCO was observed by adding 10-20 mol% Nd-422 phase [28,29]. Beyond 20 mol%, J_c drastically decreases [28] and also the peak effect disappears due to lack of Nd-123 matrix, in which solid solution pinning [3-6] or spinodal decomposition occurs [8,24]. In the IG processed sample, due to high concentration of Nd-422 particles (~ 36 mol %) in Nd-123 matrix, the J_c is low. The concentration of Nd-422 phase in the IG sample can be lowered by infiltrating the liquid into a low dense Nd-422 preform and thereby $J_c(H)$ can be improved further.

References

- [1] S. I. Yoo, R. W. McCallum, *Physica C* **210**, 147 (1993).
- [2] S. I. Yoo, N. Sakai, H. Takauchi and M. Murakami, *Appl. Phys. Lett.* **65**, 633 (1994).
- [3] M. Murakami, S. I. Yoo, T. Higuchi, N. Sakai, J. Weltz, N. Koshizuka, and S. Tanaka, *Jpn. J. Appl. Phys.* **33**, L715 (1994).
- [4] T. Egi, J. G. Wen, K. Kuroda, H. Unoki and N. Koshizuka, *Appl. Phys. Lett.* **67**, 2406 (1995).
- [5] T. Egi, J. G. Wen, K. Kuroda, H. Mori, H. Unoki, N. Koshizuka, *Physica C* **270**, 223 (1996).
- [6] T. Higuchi, S. I. Yoo, K. Sawada, N. Sakai and M. Murakami, *Physica C*, **263**, 396 (1996).
- [7] M. Nakamura, T. Hirayama, Y. Yamada, Y. Ikuhara and Y. Shiohara *Jpn. J. Appl. Phys.*, Part 1, **35**, 3882 (1996).
- [8] M. Nakamura, Y. Yamada T. Hirayama, Y. Ikuhara, Y. Shiohara, S. Tanaka, *Physica C*, **259**, 295 (1996).
- [9] P. McGinn, W. Chen, N. Zhu, M. Lanagan, and U. Balachandran, *Appl. Phys. Lett.*, **57**, 1455 (1990).
- [10] P. Diko, W. Gawalek, T. Habisreuther, T. Klupsch, and P. Gornert, *Phys. Rev. B* **52**, 13658 (1995).
- [11] R. Gopalan, T. Roy, T. Rajasekharan, G. Rangarajan and N. Hari Babu, *Physica C* **244**, 106 (1994).
- [12] S. Gotoh, M. Murakami, H. Fujimoto, N. Koshizuka and S. Tanaka, *Physica C* **166**, 215 (1990).
- [13] H. T. Ren, J. A. Xia and K. N. R. Taylor, *Physica C* **218**, 87 (1993).
- [14] C P. Bean, *Phys. Rev. Lett.* **8**, 250 (1962); *Rev. Mod. Phys.* **36**, 31 (1964).
- [15] M. Mironova, D. F. Lee and K. Salama, *Physica C* **211**, 188 (1993).
- [16] Z. L. Wang, A. Goyal, and D. M. Kroeger, *Phys. Rev. B*, **47**, 5373 (1993).
- [17] K. Yamaguchi, M. Murakami, H. Fujimoto, S. Gotoh, N. Koshizuka and S. Tanaka; *Jpn. J. Appl. Phys.* **29**, L1428 (1990).
- [18] K. Yamaguchi, M. Murakami, H. Fujimoto, S. Gotoh, T. Oyama, Y. Shiohara, N. Koshizuka and S. Tanaka; *J. Mater. Res.* **6**, 1404 (1991).
- [19] L. J. Swartzendruber, A. Ritburd, D. L. Kaiser, F. W. Gayle and L.H. Benett, *Phys. Rev. Lett.* **64**, 483, (1990).
- [20] U. Welp, W.K. Kwok, G.W. Crabtree, K.G. Wandervoort and J.Z. Liu, *Appl. Phys. Lett.* **57**, 84 (1990).
- [21] D. F. Lee, V. Selvamanickam and K. Salama, *Physica C* **202**, 83 (1992).
- [22] H. Fujimoto, T. Taguchi, M. Murakami, N. Nakamura and N. Koshizuka, *Cryogenics*, **32**, 954 (1992); K. Salama and D. F. Lee, *Supercond. Sci. Technol.* **7**, 177 (1994).
- [23] D. Dew-Hughes : *Phil. Mag.* **30**, 293 (1974).
- [24] N. V. N. Viswanath *et al*, *Appl. Phys. Lett.*, 1997 (In press).
- [25] Y. B. Kim, C. F. Hempstead and A. R. Strnad, *Phys. Rev. Lett.* **9**, 306 (1962).
- [26] G. Ravi Kumar and P. Chaddah, *Phys. Rev. B* **39**, 4704 (1989).
- [27] D. X. Chen and R. B. Goldfarb, *J. Appl. Phys.* **66**, 2489 (1989).
- [28] M. Murakami, *Supercond. Sci. Tech.*, **9** [12] 1015 (1996).
- [29] S. I. Yoo, N. Sakai, H. Kojo, S. Takebayashi, N. Hayashi, M. Takahashi, K. Sawada, T. Higuchi and M. Muarakami, *IEEE Trans. Appl. Supercond.* **7** 1781 (1997).

Chapter 7

Conclusions

This chapter summarises the important conclusions drawn from the work described in this thesis.

Optimised temperature - time schedules have been evolved to melt process $\text{NdBa}_2\text{Cu}_3\text{O}_{7-\delta}$ (Nd-123) high temperature superconductor. The processing was done in high pure Argon unlike in the work reported in the literature where oxygen-rich atmospheres were used [1]. The T_c obtained was ~ 93 K indicating the suppression of the solid solution phase. It is also found, in agreement with the literature [2,3], that Nd-123 has to be annealed at lower temperatures (250 °C-300 °C) in oxygen to facilitate the tetragonal to orthorhombic transformation, in comparison with Y-123 (400 °C-500 °C).

Nd-123 was melt processed with systematically varying amounts of insulating Nd-422 phase. The microstructural and the magnetic properties of the resulting composites were studied. The microstructural parameters were quantitatively estimated using standard metallographic procedures [4]. The infiltration and growth process which permits shape-forming with only a minimum of internal defects has been extended to the Nd-123 system. Magnetic properties were investigated by studying the flux profiles in the materials as a function of increasing magnetic fields using an ac inductive method, and also using a SQUID magnetometer. The former technique was sought to be established as a

viable means of studying the magnetic properties of high temperature superconductors by a study of sintered and press-sintered BSCCO , sintered and melt textured NdBCO . ac susceptibility measurements were also done to study the properties of the melt processed materials.

The results of detailed microstructural investigations on melt processed Nd-123 with varying Nd-422 content, and as a function of varying cooling rates through T_p , are as follows :

In the case of Nd-123 melt processed with varying Nd-422 content, various microstructural parameters such as the average width of the Nd-123 platelets, that of the gaps between the platelets, the size of Nd-422 inclusions residual in the melt processed material and also the size of the micro pores in the material after melt processing varies with Nd-422 concentration in a similar fashion as do the Nd-422 particle size in the melt at the pro-peritectic stage at high temperatures. The variation of the gap width is proportional to the platelet width as has been observed in the YBaCuO system [5] as well as in the GdBaCuO system [6]. It has been established in the literature by a study of the microstructure of Y-123 as a function of various cooling rates through T_p that the inter-platelet gaps form during the solidification stage rather than after solidification due to various kinds of stresses [7,8]. The interplatelet gaps were observed to bend continuously when the cooling rates through T_p exceeded 15°C/h [7]. Further evidence was provided in the case of solidification from a highly undercooled $211 + \text{liquid}$ mixture in which case spherulitic growth of 123 platelets with gaps between the platelets was demonstrated, and 211 particles were found to be partially converted by the liquid in the gaps [7]. The formation of gaps during the growth stage, and not subsequent to solidification, suggests separate nucleation of the platelets. In the present work, further evidence for the separate

nucleation of platelets has been given in Fig. 3.10(d), where different platelets are shown to protrude by different extent into a neighbouring domain. It has been shown in the present work that the variations of platelet width and the inter-platelet gap width with the concentration of Nd-422 varies in the same way as do the size of the Nd-422 particles in the liquid at the melting stage (Fig. 3.17). The Nd-422 particles are highly acicular at the melting stage in the case of Nd-123 with 0 and 10 mol % Nd-422 because only very few such particles are available in the liquid, and the particles grow depending on their natural habit. However, in the samples with higher Nd-422 content, the extra Nd-422 serve as nuclei for the Nd-422 formed during the melting of Nd-123, and the resulting Nd-422 particles in the liquid are small and spherical due to the competitive growth of a large number of particles in the liquid. The similarity in the variations of platelet and gap widths with Nd-422 size variation in the melt indicates a connection between the platelet nucleation and the Nd-422 concentration in the liquid, with their width being correlated to the 422-size in the liquid.

There are, however, several differences between the microstructural evolution in the melt processed Nd-123 in comparison with that in Y-123 or Gd-123. All the differences arise from the faster rate of crystallization of Nd-123 [9] in comparison with Y-123 and Gd-123. The pseudo-binary phase diagram of Y-123 shows a continuous (without a change of slope) liquidus at T_p [10] whereas the liquidus in the case of Nd-Ba-Cu-O system shows a change of slope [11]. The absence of a change in the slope of the liquidus at T_p in the case of the YBCO system is due to the lack of solubility of the Y-ions in the liquid [12]. The increased solubility of the Nd-ions in the liquid leads to the faster crystallization rate for Nd-123. The textured growth of RE-123 platelets has been attributed to their competitive growth by Schmitz *et al.* [13], though they have not suggested any mechanism as to how they nucleate. It has been proposed that, during

the cooling stage, when the solidification front traverses the sample volume slower than the platelet growth rate, plane-front solidification of parallel platelets takes place. In the case of Y-123 system, at 15 °C/h cooling rate, the solidification front moves too fast for the undisturbed growth of the parallel platelets [7]. However in the Nd-123 system, the faster crystallization rate of the phase enables the solidification front to be undisturbed even at cooling rates of 40 °C/h through T_p .

The liquid phase left back in the interplatelet gaps has been demonstrated to be from the solidification stage [14]. The gaps may have their origin in the poor solubility of the RE-ions in the liquid which limits the crystallization of 123 to a very small range (measured in microns) around the dissolving 211 particles in the peritectic reaction [15]. It is known that the reaction zone surrounding dissolving Y-211 particles is only a few microns in width [16]. The gaps would result when the platelets thicken to such an extent that there are no more primary phase particles left in the region between the platelets for the peritectic reaction to continue. Transport of Y-ions from relatively farther points to complete the reaction would not be possible. The gap widths can be expected to be correlated with the 211 size and spacing at the melting stage if 211 size and distribution plays a role in deciding the platelet width. The width of gaps in the stoichiometric Nd-123 has been found to be $\sim 0.7 \mu\text{m}$ whereas that in Y-123 system has been reported to be $\sim 3 \mu\text{m}$ [5]. This also would explain the fact that the gaps are observed to be completely closed at many points in the melt processed Nd-123 microstructure (Figs. 3.10 and 3.12), whereas they have been found to extend from one end of the domain to the other in the Y-123 system [5]. Because of the larger solubility of Nd ions in the liquid, Nd-ions may be expected to diffuse larger distances in order to react with the residual liquid in the gaps so as to form more 123 and to reduce the observed gap widths in the Nd-123 system.

The size of the residual 211 in the RE-123 matrix is controlled by the growth of 211 particles in the liquid above T_p through Ostwald ripening [17] and by the consumption of those particles below T_p through the peritectic reaction. It has been reported that the Gd-211 in melt processed Gd-123 matrix decreases in size with slower cooling through T_p [6]. However, in the case of the Nd-123 system, the particle size was observed to increase. This again, can be attributed to the better solubility of Nd-422 in the liquid above T_p where the smaller grains dissolve to promote the growth of the larger ones. The longer residence time a few degrees above T_p during the slow cooling stage causes much more grain growth in the case of the Nd-123 samples cooled at 1 °C/h than in the faster cooled samples.

The magnetic J_c determined from dc magnetization measurements in the Nd-123 superconductor is found to increase with the Nd-422 content upto 30 mol % just as in the Y-123 system. The J_c in samples peak at 20-30 mol % Nd-422. The variation of J_c with Nd-422 content has been correlated to accurately estimated microstructural parameters such as volume fraction of Nd-422, and the interfacial area between the Nd-422 particles and Nd-123 matrix. It is found to vary linearly with the Nd-123/Nd-422 interfacial area. However, in the Nd-40 sample, even though the interfacial area is more, the J_c has been decreased due to a reduction in the superconducting path. A mild peak effect is observed in the sample with 30 mol% Nd-422. There is no peak effect in the other Nd-123 samples. The absence of the peak effect in most of the samples can be attributed to the lack of spinodal decomposition, while oxygenating the samples. The present samples were annealed in the oxygen atmosphere at higher temperature (at 500 °C) for lesser time (~ 12 h), and at 250 °C to 350 °C for a longer time. But later it was found by Nakamura *et al* [18] that the peak effect is controlled by the oxygenation schedule. They found that the samples annealed at 500 °C for 100 h and followed by 350 °C at 250

h showed enormous **peak effect** due to **spinodal decomposition**. Annealing the **NdBCO** system at **high** temperatures for lesser time **might** have caused the **absence** of **peak effect**.

The observed anticlockwise tilt in the M-H loop of a melt textured Nd-123 superconductor could be described well by **Kim's** critical state model combined with a contribution from the **paramagnetism** of Nd^{3+} ions represented by the Brillouin function.

This thesis also discusses the processing of $NdBa_2Cu_3O_{7-\delta}$ superconductor by an Infiltration and Growth (IG) process that involves the **infiltration** of liquid phases into a shaped preform followed by slow cooling through the peritectic formation temperature of Nd-123. The IG process eliminates shrinkage, large hollows within the interior of the samples and it can enable the fabrication of **3-dimensional** complex-shaped objects with good dimensional tolerance and high critical current density for applications. The IG processed samples also contain domains consisting of parallel platelets of Nd-123, separated by gaps. The estimated Nd-422 content in the IG sample is nearly similar to the conventional melt processed sample with 40 **mol** % of Nd-422. A major advantage of the IG process is that it minimizes the possibility of Nd-422 coarsening in the liquid. The result is a very uniform distribution of nearly spherical Nd-422 inclusions with 80% of the particles having a diameter less than 1 μm , in the highly textured Nd-123 matrix. The J_c of IG sample is of the order of 10^5 A/cm² at 5 K and 0.4×10^4 A/cm² at 77 K, which are slightly lower than the values reported in the samples prepared by the other melt processing techniques. The possible reason for the lower J_c is higher concentration of Nd-422 in Nd-123 matrix and the absence of the spinodal decomposition due to short hold at 500 °C during oxygenation. Efforts aimed at lowering the Nd-422 content in samples prepared by the IG process are in progress.

Temperature variation of ac susceptibility on melt grown samples shows a sharp single diamagnetic transition around 92 K with a transition width of 2 K. $\chi''(T)$ shows a sharp single peak. The sharpness of the transition suggests suppression of the solid solution phase of the type $\text{Nd}_{1+x}\text{Ba}_{2-x}\text{Cu}_3\text{O}_{7-\delta}$. The single diamagnetic transition and single ac loss peak are indicative of suppression of weaklinks in the melt textured samples, which is in contrast with the polycrystalline samples where a two step behavior is observed. The observed weak field dependence of the ac loss peak position is suggestive of a large pinning force. The J_c estimated from $\chi''(T)$ measurements is found to increase with Nd-422 content upto Nd-30 and then to decrease for the Nd-40 sample. This trend is the same as that observed in the J_c s obtained from the SQUID data. The observed second minor ac loss peak beside the major $\chi''(T)$ peak in bulk multidomain Nd-40 sample has been attributed to the anisotropy in pinning in the ab (basal) plane and along the c-axis, but not due to weak links.

In the melt textured samples, with decreasing ac magnetic field, the peak value of the imaginary $\chi''(T)$, decreased in addition to a shift of its position to higher temperatures. The former behavior is against the prediction of the critical state models in which the flux pinning is assumed to be completely irreversible. The reduction in the ac loss has been explained by considering the reversible fluxoid motion of a pinned vortex lattice as proposed by Campbell. For the appearance of reversible fluxoid motion the size of the superconducting specimen in which current flows uniformly should be less than the sample size. Existence of platelets of size (2-3 μm) separated by $\sim 0.2 \mu\text{m}$ gaps in the melt grown sample is proposed to result in the reversible fluxoid motion thereby causing reduced ac loss as the transition temperature is approached.

The universal behaviour of the field and temperature dependences of $\chi(H_{dc}, H_{ac})T$

and $\lambda(T, H_{dc})H_a$ respectively, has **been demonstrated** in the 110 K phase of Bi Sr-Ca Cu-O system and **melt textured** NdBCO system in terms of a single parameter (δ), in the regime where the flux profile is linear in the sample. It implies that, all the ac susceptibility measurements with varying temperature, ac field and dc field can be reduced to a universal curve, which describes the susceptibility as a function of the single parameter δ . Analysis of the ac susceptibility data shows that the field dependence of J_c is better described for the sintered BSCCO sample by the power law model upto 80 Oe and for the melt textured NdBCO sample by the Kim's critical state model for the fields upto **10 KOe**.

A facility for the measurements of magnetic flux profiles in HTSCs was set up during the course of the work. The methodology of measurement had been proposed by Campbell [19]. An appropriate expression for estimating the ac penetration depth has been derived (Chapter 2) to account for the changes in the present configuration relative to that of Campbell [19]. In the present case the resultant voltage from the secondaries is nullified in the absence of a sample rather than with the sample in the Meissner state as was done by Campbell [19].

The magnetic flux profiles (H_{ac} versus p/R) in sintered BSCCO and NdBCO samples exhibit non-linear curves at very low fields followed by a peak like structure at the full penetration field H^* into the intergrain region. At $H_{ac} > H^*$ the penetration remains a constant upto $H = H_{c1g}$, the lower critical field of the grains. For $H_{ac} > H_{c1g}$ the flux profile into the grains is obtained. The H^* and J_{ci} are found to be enhanced for the BSCCO sample on press sintering. This has correlation to the reduction in porosity and the resultant strengthening of the coupling between the grains. The observed enhancement in the apparent lower critical field H_{c1g} on press sintering has also been reported from M-H loop studies and was attributed to the existence of a surface barrier to the

penetration of magnetic flux [20].

In the case of the sintered BSCCO sample, the flux profile becomes linear at low fields in the presence of a dc field. Slope of this flux profile is reduced by increasing the dc field. $J_{ci}(H_{dc})$ has been determined by measuring the slope of the flux profile in the linear regime for the BSCCO samples. It is found to vary as $K/(H_{dc} + H_o)$. Using the fit parameters K and H_o , all the features of the experimentally observed flux profiles could be simulated very well using Kim's critical state model. When H_{ac} is comparable to H_{dc} , an oscillatory behavior is seen in the flux profiles ; this has been traced to a strong magnetic field dependence of J_c .

The sintered NdBCO sample is found to show a complete penetration of the flux into the intergrain region at $H_{ac} = 4$ Oe with $H_{dc} = 0$ Oe and even into the grains at $H_{ac} \sim 50$ Oe with $H_{dc} = 1$ KOe. The grain fraction f_g calculated from the flux profile is consistent with the estimated grain fraction from optical micrographs. The intergranular profile is simulated using Kim's model and the grain flux profile is derived from the global profile recorded at high fields. The grain profile could be simulated well only when a wide distribution in grain critical current density J_{cg} was assumed. The distribution in J_{cg} can arise due to the low T_c solid solution phase of the type $Nd_{1+x}Ba_{2-x}Cu_3O_{7-\delta}$; the effect of this can also be seen in the temperature variation of ac susceptibility.

The flux penetration into the melt processed samples is much slower compared to that into the sintered samples due to stronger flux pinning and coupling between the domains in the former. The extent of penetration among the melt textured samples is smaller in the Nd-422 added samples when compared to stoichiometric Nd-123 sample. The flux

profiles are linear, indicating that J_c is nearly independent of the field at the fields considered. At high fields ($H_{dc} = 4-8$ KOe) the flux profiles exhibit two different slopes. From microstructural considerations, the slope change may correspond to the inter-platelet gap region allowing the full penetration of the flux into that region ; thereafter the flux begins to enter platelets themselves. It is known from high resolution Faraday measurements on melt textured YBCO, the magnetic flux penetrates preferentially along the gaps and then into the matrix at the field range of 2-4 KOe at 5 K [21].

The bulk critical current density J_{c1} , is lower than the platelet critical current density J_{c2} , by an order of magnitude, which suggests that if the gaps are minimized in the melt textured samples, the bulk critical current density of the melt textured samples can be improved to a value as high as that of the platelet critical current density. In the NdBCO system the platelet gaps are small compared to those in other REBCO systems, due to former's high rate of crystallization. The volume fraction of the empty space corresponding to the gaps in various melt textured samples could be correlated well to the position of the slope change on the p/R axis of the flux profiles. This supports the view that the flux initially penetrates the sample along the gaps, and then into the grains.

Variation and the magnitude of the measured bulk critical current densities on large sized multidomain melt textured samples obtained using the flux profile technique are quite similar to those obtained on smaller sized nearly single domain samples using a SQUID magnetometer. By measuring the reversible penetration depth in multidomain samples processed at two cooling rates through T_p , namely, the slow cooled sample (1 °C/h) with clean domain boundaries and the other fast cooled (40 °C/h) sample with some amount of liquid phase at the domain boundaries, it is shown that flux profile measurements can give information on domain coupling strength in melt textured samples.

The domain boundaries in samples processed with slow rate of cooling ($1\text{ }^{\circ}\text{C/h}$) through peritectic temperatures are strongly coupled upto an applied field of 10 KOe. Decoupling nature of domain boundaries are observed in the melt textured samples processed at faster rates of cooling. The flux profile technique can thus be used to measure bulk J_c and for characterization of large sized melt grown samples.

References

- [1] S. I. Yoo, N. Sakai, H. Takaichi and M. Murakami, Appl. Phys. Lett. **65**, 633 (1994).
M. Murakami, S. I. Yoo, T. Higuchi, N. Sakai, J. Weltz, N. Koshizuka, and S. Tanaka, Jpn. J. Appl. Phys. 33, L715 (1994).
- [2] W. Bieger, P. Schatzle, G. Krabbes, L. Zelenina, U. Weisner, G. Stover, P. Verges and J. Klosowski, Proc. Europ. Conf. Appl. Supercond. EUCAS '95, p 147 (1995).
- [3] N. Chikimoto, S. Ozawa, S. I. Yoo, N. Hayashi, and M. Murakami, Physica C **278** 187 (1997).
- [4] "The basis of quantitative metallography" ed. F. B. Pickering, Institute of Metallurgical Technicians, Monograph No.1.
- [5] R. Gopalan, T. Roy, T. Rajasekharan, G. Rangarajan and N. Hari Babu, Physica C **244**, 106 (1994).
- [6] E. Sudhakar Reddy and T. Rajasekharan, Supercond. Sci. and Tech., 1997 (In press).
- [7] E. Sudhakar Reddy and T. Rajasekharan, Phys. Rev. B, 1997 (In press).
- [8] E. Sudhakar Reddy and T. Rajasekharan, Physica C, **259** 56 (1997).
- [9] K. Salama, A. S. Parikh, L. Woolf, Appl. Phys. Lett. **68**, 1993 (1996).
- [10] S. Jin, T. H. Tiefel, R. C. Sherwood, R. B. van Dover, M. E. Davis, G. W. Kammlott, and R. A. Fastnacht, Phys. Rev. B 37, 7850 (1988).
- [11] M. Nakamura, M. Kambara, T. Umeda, Y. Shohara, Physica C **266**, 178 (1996).
- [12] C. Krauns, M. Sumida, M. Tagami, Y. Yamada and Y. Shiohara, Z. Phys. B **96**, 207 (1994).
- [13] G. Schmitz, J. Laakmann, C. Wolters, S. Rex, W. Gawalek, T. Habisreuther, G. Bruchlos and P. Gornert, J. Mater. Res. 8, 2774 (1993).
- [14] K.B. Alexander, A. Goyal, D. M. Kroeger, V. Selvamanikam, and K. Salama, Phys. Rev. B. **45**, 5622 (1992).
- [15] T. Izumi, Y. Nakamura, and Y. Shiohara, J. Mater. Res., 7, 1621 (1992).
- [16] M. A. Rodriguez, B. J. Chen and R.L. Snyder, Physica C **195**, 185 (1992).
- [17] Ostwald, Z. Phys. Chem., 34, 495 (1990).
- [18] M. Nakamura, Y. Yamada T. Hirayama, Y. Ikuhara, Y. Shiohara, S. Tanaka, Physica C, **259** 295 (1996).
- [19] A. M. Campbell, J. Phys. C 2, 1492 (1969).
- [20] N. Harish Kumar and V. Seshu Bai, Phys. Rev. B 53, 15281 (1996).
- [21] Th. Schuster, M. R. Koblishka, H. Kuhn, M. Glücker, B. Ludescher, and H. Kronmuller, J. Appl. Phys. 74, 3307 (1993).

List of publications

Journals

1. "Magnetic flux profiles in **BSCCO** and **NdBCO** superconductors and a simulation to critical state models."
N. Hari Babu, T. Rajasekharan and V. Seshu Bai.
Phys. Rev. B **56**, (1997).
2. "Universal Behaviour of AC Susceptibility in the 110 K Phase of Bi-Sr-Ca-Cu-0 System"
N. Hari Babu, T. Rajasekharan, S. Ravi and V. Seshu Bai.
Phys. Rev. B **52**, 13 605, (1995).
3. "Microstructural and magnetisation study in melt-grown Y-Ba-Cu-0 samples".
R. Gopalan, T. Roy, T. Rajasekharan, G. Rangarajan and N. Hari Babu.
Physica C **244**, 106, (1995).
4. "**NdBa₂Cu₃O₇** superconductors with fine spherical Nd-422 inclusions through an infiltration and growth process."
N. Hari Babu, T. Rajasekharan, Latika Menon and S. K. Malik
J. Americ. Ceramic Society (Accepted).
5. "Melt texturing of **NdBa₂Cu₃O_{7-δ}** superconductor in short time"
N. Hari Babu, T. Rajasekharan and V. Seshu Bai
Submitted
6. "Influence of Nd-422 on flux penetration in melt textured **NdBa₂Cu₃O₇** superconductor."
N. Hari Babu, T. Rajasekharan and V. Seshu Bai.
Submitted
7. "Use of ac inductive method to test domain coupling strength in melt textured samples under external dc fields".
N. Hari Babu, T. Rajasekharan and V. Seshu Bai.
Submitted
8. "Ac inductive method : a tool for characterization of bulk melt textured superconductors".
N. Hari Babu, T. Rajasekharan and V. Seshu Bai
Submitted
9. "Low field ac magnetic response of melt textured **NdBa₂Cu₃O_{7-δ}**- **Nd₄Ba₂Cu₂O₁₀** superconductors"

N. Hari Halm, T. Rajasekharan and V. Seshu Bai
Submitted

10. "Effect of a systematic variation of $\text{Nd}_4\text{Ba}_2\text{Cu}_2\text{O}_{10}$ content on the microstructure of melt processed $\text{NdBa}_2\text{Cu}_3\text{O}_{7-\delta}$ superconductor"¹¹
N. Hari Babu and T. Rajasekharan.
Submitted
11. "Effect of a systematic variation of $\text{Nd}_4\text{Ba}_2\text{Cu}_2\text{O}_{10}$ content on the magnetic properties of $\text{NdBa}_2\text{Cu}_3\text{O}_{7-\delta}$ - $\text{Nd}_4\text{Ba}_2\text{Cu}_2\text{O}_{10}$ composites."
N. Hari Babu, T. Rajasekharan, L. Menon, S. Srinivas and S. K. Malik
Submitted
12. "Effect of cooling rate on microstructural and magnetic properties of melt textured NdBCO superconductor"
N. Hari Babu, T. Rajasekharan and V. Seshu Bai.
Submitted
13. "Universal behavior of ac susceptibility in melt textured NdBCO superconductor"
N. Hari Babu, T. Rajasekharan and V. Seshu Bai
Submitted

(b) Conference proceedings / Abstracts

International :

1. "Influence of Nd422 inclusions and fast cooling on flux penetration in melt textured Nd123"
N. Hari Babu, T. Rajasekharan and V. Seshu Bai
Presented at the International Workshop on the Processing and Applications of Superconducting (RE)BCO Large Grain Materials, 7-9 July, 1997, Cambridge, UK.
2. "High rate melt processing of $\text{NdBa}_2\text{Cu}_3\text{O}_7$ superconductors".
N. Hari Babu and T. Rajasekharan.
Presented at International workshop on HTS - 10 Years After Discovery, Jaipur, India. December 16-21, 1996
3. "Near net-shaped processing for high J_c in $\text{REBa}_2\text{Cu}_3\text{O}_7$ superconductors".
T. Rajasekharan, E. Sudhakar Reddy, N.V.N. Viswanath, and N. Hari Babu
Proceedings of International symposium on ASMCCD, TIFR, Mumbai, India. September 17-20, 1996.

National

1. " ac reversible fluxoid motion in high J_c bulk melt textured NdB(X) superconductors"
N. Hari babu, T. Rajasekharan, and V. Seshu Bai
Proceedings of the DAE Solid State Physics Symposium, **40C**, ... (1997).
2. "Melt processing of $\text{NdBa}_2\text{Cu}_3\text{O}_7/\text{Nd}_4\text{Ba}_2\text{Cu}_2\text{O}_{10}$ composites in reduced Oxygen partial pressures"
N. Hari Babu and T. Rajasekharan
Symposium on Current Topics in Physics of Materials, Hyderabad, India
3. "Magnetic flux profiles in the 110 K phase of the Bi-Sr-Ca-Cu-0 system"
N. Hari Babu, T. Rajasekharan and V. Seshu Bai
Proceeding of the DAE Solid State Physics Symposium, **39C**, 301, (1996).
4. "Critical state model analysis of intergrain and intragrain AC M - H loops in sintered $\text{Bi}_{1.2}\text{Pb}_{0.3}\text{Sr}_{1.5}\text{Ca}_2\text{Cu}_3\text{O}_y$ "
N. Harish Kumar, N. Hari Babu, T. Rajasekharan, and V. Seshu Bai
Proceeding of the DAE Solid State Physics Symposium, 38C, 342, (1995).
5. "Flux profiles in sintered GdBCO and Melt Grown YBCO HTSCs".
P. Bhanusri, N. Hari Babu, T. Rajasekharan and V. Seshu Bai
Proceedings of the DAE Solid State Physics Symposium, 38C, 341, (1995).
6. "Application of critical state models to the AC susceptibility in the presence of dc field".
N. Hari Babu, T. Rajasekharan, S. Ravi and V. Seshu Bai
Proceedings of the DAE Solid State Physics Symposium, **37C**, 373 (1994).
7. "Universal behavior of ac suceptibility in the 110 K phase of Bi-Sr-Ca-Cu-0 system"
N. Hari babu, T. Rajasekharan, S. Ravi and V. Seshu Bai
Proceedings of the DAE Solid State Physics Symposium, **37C**, 374 (1994).